Reconstruction hyperspectrale haute résolution par inversion de mesures spectroscopiques à integrale de champ. Application au spectromètreinfrarouge MIRI-MRS du télescope spatial James webb

Ralph Abi Rizk

Thèse de doctorat

NNT: 2021UPASG087

université PARIS-SACLAY

Reconstruction hyperspectrale haute résolution par inversion de mesures spectroscopiques à integrale de champ. Application au spectromètre infrarouge MIRI-MRS du télescope spatial James Webb.

High-resolution hyperspectral reconstruction by inversion of integral field spectroscopy measurements. Application to the MIRI-MRS infrared spectrometer of the James Webb Space Telescope

Thèse de doctorat de l'Université Paris-Saclay

École doctorale n° 580, : Sciences et technologies de l'information et de la communication (STIC)
Spécialité de doctorat: Traitement du signal et des images
Unité de recherche: Université Paris-Saclay, CNRS, CentraleSupélec, Laboratoire des signaux et systèmes, 91190, Gif-sur-Yvette, France.
Référent: Faculté des sciences d'Orsay

Thèse présentée et soutenue à Paris-Saclay, le 8/11/2021,par

Ralph ABI RIZK

Composition du jury:

Barbara Nicolas Directrice de Recherche, CNRS, Créatis, Lyon	Présidente
Hervé Carfantan Professeur, Université Paul Sabatier	Rapporteur & Examinateur
Said Moussaoui Professeur, Ecole Centrale de Nantes	Rapporteur & Examinateur
Émilie Chouzenoux Chargée de Recherche, Inria	Examinatrice

Direction de la thèse:

François Orieux Maître de Conférence, Université Paris-Saclay	Directeur de thèse
Alain Abergel Professeur, Université Paris-Saclay	Co-directeur de thèse

Thesis conducted at

Laboratoire des Signaux et Systèmes (L2S)
Université Paris-Saclay, CNRS, CentraleSupélec

3 rue Joliot-Curie, 91190, Gif-Sur-Yvette, France

Institut d'Astrophysique Spatiale (IAS),
Université Paris-Saclay, CNRS

91405 Orsay, France

co-funded by

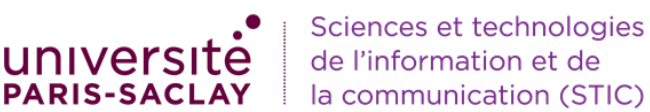

Résumé

L'imagerie hyperspectrale produit des images tridimensionnelles (2D+λ) avec deux dimensions spatiales et une dimension spectrale. Cependant, une observation directe des images hyperspectrales n'est pas possible. Au lieu de cela, des instruments hyperspectraux, qui s'appuient principalement sur des spectromètres dispersifs, sont conçus pour projeter l'image 2D+λ sur des detecteurs 2D (ou 1D), résultant en un ensemble de mesures spectroscopiques 2D (ou 1D). Plusieurs techniques d'acquisition d'images hyperspectrales sont adoptées. Parmi ces techniques, le spectromètre à champs integrale (Integral Field Spectrometer: IFS) observe le champs de vue de l'image 2D+λ selon plusieurs slits en parallèle, et la lumière de chaque slit est dispersée et projetée sur des détecteurs 2D.

L'objet de cette thèse est la reconstruction de l'image hyperspectral à haute résolution spatiale et spectrale, par inversion de mesures spectroscopiques 2D observées par l'instrument IFS "Meduim Resolution Spectrometer: MRS" de l'instrument "Mid-Infrared" embarqué à bord du téléscope spatial "James Webb". Le problème de reconstruction est un problème "mal-posé" car les mesures souffrent de plusieurs dégradations: (1) une dégradation spatiale introduite par la réponse de l'optique qui dépend de la longueur d'onde, (2) une dégradation spectrale introduite par la réponse de l'instrument de dispersion également dépendant de la longueur d'onde, (3) l'instrument hyperspectral considère plusieurs observations avec différents champs de vues, (4) un échantillonnage spatial et spectral avec un pas d'échantillonnage hétérogène, (5) un sous-échantillonnage spatial.

Pour traiter ces mesures, notre approche repose sur les problèmes inverses suivant deux étapes. Tout d'abord, nous concevons un modèle direct qui décrit le comportement de l'instrument IFS et qui établit une relation entre les mesures et l'image 2D+λ inconnue. Ensuite, ce modèle est utilisé pour la reconstruction en s'appuyant sur l'approche des moindres carrés régularisées avec une régularisation spatiale et spectrale convexe pour la préservation des contours. Nous utilisons les approches semi quadratiques rapides pour résoudre le problème de reconstruction. L'algorithme de reconstruction proposé inclut une fusion des mesures issues de différentes observations spatio-spectrales avec différents flous et pas d'échantillonnages, une SR à partir des différents pointages de l'instrument pour compenser l'information spatiale perdue au niveau du détecteur, et une déconvolution pour minimiser le flou.

Nous testons et validons l'algorithme de reconstruction proposé sur plusieurs images d'entrée synthétiques ayant des différentes distributions spatiales et spectrales.

Pour justifier le choix de la régularisation adoptée, nous comparons l'algorithme proposé avec l'algorithme SR représentatif de l'état de l'art qui s'appelle le "Shift-and-Add", utilisé pour traiter les mesures du MRS. Cette technique combine toutes les mesures issues de différentes observations et différents pointages de l'instrument afin d'améliorer la résolution spatiale de l'image 2D+λ reconstruite. Cependant, le "Shift-and-Add" ne prends pas en compte le flou spatial et spectral. Par conséquent, l'algorithme est souvent suivi d'une étape de déconvolution qui prends en compte le flou spatial. Nous choisissons la régularisation total variation (TV) qui s'applique séparément à chaque image monochromatique sans tenir compte de la corrélation entre les bandes spectrales. Finalement, nous comparons l'algorithme que nous avons mis au point avec l'approche des moindres carrées avec une régularisation quadratique l_2.

On constate à partir des images reconstruites avec les différents algorithmes, que l'algorithme "Shift-and-Add" suivi d'une régularisation spatiale TV ne parvient pas à reconstruire les détails à petite échelle, et la régularisation quadratique introduit des rebonds et empêche la préservation des contours. En revanche, la reconstruction grâce à l'algorithme que nous proposons montre une déconvolution nette et une amélioration significative de la résolution spatiale et spectrale des images 3D reconstruites par rapport aux algorithmes de l'état de l'art, notamment sur les bords.

Malgré l'amélioration de la résolution des images reconstruites, l'algorithme proposé présente des limitations. Tout d'abord, le nombre d'inconnues que l'on cherche à estimer est significativement grand, ce qui va augmenter le temps de calcul. De plus, les mesures produites par le MRS ont souvent une information spectrale complexe comme un continuum et une succession de raies spectrales ce qui nous force à déterminer plusieurs hyperparametres spectraux augmentant la complexité de l'algorithme.

Pour surmonter cela, nous proposons un autre algorithme de reconstruction en supposant que l'image 2D+λ observée se trouve dans un sous-espace de faible dimension et peut être modélisée comme une combinaison linéaire de composantes spectrales, supposées connues, pondérées par des coefficients de mélange inconnus. Le problème de reconstruction se réduit à l'estimation des cartes d'abondances en passant par un nouveau model direct qui inclut les composantes spectrales connues. Pour résoudre le problème de reconstruction, nous nous appuyons sur l'algorithme Majorize-Minimize Memory Gradient (3MG).

Nous testons l'algorithme proposé sur des simulations astrophysiques représentant la région de photodissociation de la "barre d'Orion" ayant une information spectrale complexe (succession des raies). On montre encore une fois que l'algorithme proposé fournit la meilleure reconstruction spatiale en termes de résolution et d'erreur comparé aux algorithmes de l'état de l'art. En plus, l'information spectrale est bien préservée car la résolution spectrale de l'image reconstruite est imposée par les composantes spectrales connues.

En résumé, l'ensemble de nos travaux au cours de cette thèse nous a permis en premier lieu de concevoir deux différent modèles directs pour l'instrument MRS

à partir de deux modèles différents pour l'image d'entrée (modèle voxel et modèle de mélange linéaire avec des composantes spectrales connues) qui produisent des mesures projetées sur des detecteurs 2D en tenant compte les limitations spatio-spectrales. Pour résoudre ce problème mal posé, nous avons proposé un algorithme de "super-résolution" multi-images, basé sur l'approche des moindres carrés régularisés, avec une régularisation convexe préservant les bords qui permet des améliorations spatiales via des observations multi-images et une déconvolution. L'algorithme proposé est résolu via l'optimisation du gradient majorize-minimize memory (3MG) et testé sur des images synthétiques 3D, mesurant dans la gamme infrarouge, donc adapté au prochain instrument infrarouge à bord du James WebbSpace Telescope (JWST).

Acknowledgments

There are many people whom I would like to thank for their contributions, both directly and indirectly, to this thesis.

I would first like to express the most profound appreciation to my supervisors M. François Orieux and M. Alain Abergel, for their guidance, support, and trust throughout this project, from inception to completion. Their valuable feedback, expertise, and enthusiasm for research made my Ph.D. study a rich experience in different aspects.

I want to express my deep gratitude to the reviewers, M. Hervé Carfantan and M. Said Moussaoui, for their time in reading my manuscript and for all the comments and suggestions. I also thank the examiners Mme. Barbara Nicolas and Mme. Emilie Chouzenoux for evaluating my work and providing me with constructive critics.

I want to thank the cnes and the Doctoral school STIC for funding my thesis for three years.

To my dear colleagues, Mickaël (our biker), Daouda (keep practicing my "indoor" tennis partner), Nico (you + me = the losers of the GPI :p), Marine (who will piss you off now?), Pierre (I will miss your weird stories), Edwardo (one day we will master "le subjonctif") and Stephano (I mean...), I want to thank you for all your encouragements and all the coffee (and tea) breaks we had (which was more of a therapy session for frustrated Ph.D students :')). In addition, I would like to thank Nicolas Gac, Charles Soussen, Patrice Brault, and all the GPI team for all the nourishing conversations we had.

To Charly, Gabriel, Dan, Maria, and Guillaume, thank you all for your unwavering support and for dragging me out of my apartment to take breaks and have fun when I've been stressed out. For a foreigner arriving in France without knowing anyone, I feel fortunate to have you in my life.

Finally, I would like to express my deepest gratitude to my wonderful parents and siblings for being a constant source of persistence, inspiration, and motivation despite the distance that separates us. Words are not enough to thank you.

Contents

List of Figures

List of Tables

List of Algorithms

Acronyms

3MG: Majorize Minimize Memory Gradient.

CG: Conjugate Gradient.

FOV: Field Of View.

GR: Geman and Reynold.

GY: Geman and Yang.

HQ: Half-Quadratic.

HR: High Resolution.

HS: HyperSpectral.

HSI: HyperSpectral Imaging.

ICA: Independent Components Analysis.

IFS: Integral Field Spectrometer.

IFU: Integral Field Unit.

JWST: James Webb Space Telescope.

LR: Low Resolution.

MIRI: Mid InfraRed Instrument.

MM: Majorize-Minimize.

MRS: Mid-Resolution Spectrometer.

MS: MultiSpectral.

NMF: Non-negative Matrix Factorization.

OPD: Optical Path Difference.

PAN: PANchromatic.

PCA: Principal Component Analysis.

PSF: Point Spread Function.

PSNR: Peak Signal to Noise Ratio.

S&A: Shift and Add.

SAM: Spectral Angular Mapper.

SNR: Signal to Noise Ratio.

SR: Super-Resolution.

SSIM: Structural Similarity Index.

STScI: Space Telescope Science Institute.

TV: Total Variation.

Notations

$\boldsymbol{A}$: symmetric positive definite matrix

$\boldsymbol{a}$: mixing coefficients

α: step-size

$\boldsymbol{b}$: auxiliary variables

$\boldsymbol{\alpha}$: multi-dimensional step-size

$\boldsymbol{s}$: spectral components

$\boldsymbol{D}$: multi-dimensional subspace

$\boldsymbol{d}$: descent direction

$\hat{\boldsymbol{a}}$: reconstructed mixing coefficients

$\hat{\boldsymbol{x}}$: reconstructed input image

$\boldsymbol{H}$: Observation matrix or forward model

λ: wavelength in μm

$\mathcal{J}^*$: augmented objective function

$\mathcal{J}$: objective function

$\mathcal{R}$: regularization term

μ: regularization parameter

ϕ: differentiable potential function

$\boldsymbol{x}$: unknown 3D input image of size $I \times J \times L$

$\boldsymbol{y}$: measurements of size $I' \times L'$

c: spectral channel

M: number of spectral components

p: spatial shift index

Q: quadratic surrogate function

R: spectral resolution

T_i, T_j: spatial sampling step of the input image

T_l: spectral sampling step of the input image

$T_{i'}$: spatial sampling step of the measurements

$T_{l'}$: spectral sampling step of the measurements

w_c: channel windows

Chapter 1

Introduction

Contents

1.1 General context

With the expansion of the universe, the visible light emitted by celestial objects is shifted to the infrared range through cosmological redshifting. Moreover, the infrared spectral range contains numerous spectral features emitted by interstellar dust and gas. Therefore, the infrared spectral range is increasingly observed by astrophysicists to address key questions such as the evolution of galaxies over time, the formation of stars and planets, the chemical complexity of the interstellar medium, etc. More and more complex instruments are put on board observatories operated in space to avoid atmospheric infrared absorption. The goal is to provide spatial and spectral information on the observed objects, and ideally, their hyperspectral (HS) images.

In the remote sensing community, HS images are defined as 3-dimensional spatio-spectral (2D+λ) images spanning two spatial dimensions (i, j) and a series of narrow spectral bands l forming the third dimension. Unfortunately, the direct observation of HS images is not straightforward because 3D detectors actually do not exist. Instead, hyperspectral instruments, primarily relying on dispersive spectrometers, are designed to project the HS input image onto 2D (sometimes 1D) detectors, resulting in a set of 2D (or 1D) measurements with high spectral resolution. Hence,

a processing step of these measurements is mandatory to reconstruct the HS input images.

In most cases, the processing of high spectral measurements is challenging because of the spatial and spectral degradations during the acquisition process. For instance, the optical components of the measuring instrument are limited by the diffraction [Goodman 1996] and introduce wavelength-dependent spatial blurring to the 2D+λ input images. Moreover, the wavelength dispersion system (*i.e.* prism, diffraction grating, etc.) is not perfect and introduces spectral blurring, which is also wavelength-dependent [Pérez 2004]. Finally, the pixel size of the HS input images is often smaller than the pixel size of the HS detectors, resulting in severe limitations of the spatial resolution of the image, as in classic Super-Resolution problems [Sung Cheol Park 2003].

In this thesis, we propose original reconstruction algorithms based on inverse problem approaches [Idier 2001b] to estimate 2D+λ astronomical sky images from a set of measurements with a high spectral resolution, degraded by an HS instrument and projected onto 2D detectors. The reconstruction algorithms mainly include (1) a data fusion step that combines all 2D measurements to provide a 2D+λ image, (2) a deconvolution step that minimizes the blurring and improves the contrast and sharpness of the reconstructed images [Idier 2001b], and (3) a multi-frame Super-Resolution (SR) step [Sung Cheol Park 2003] to compensate for the spatial information lost during the HS detector sampling. This work is part of long-term collaborations between the "Laboratoire des Signaux et Systèmes" (L2S) and the "Institut d'Astrophysique Spatiale" (IAS). These collaborations mainly concern the processing of degraded measurements provided by various measuring instruments from different space missions [Rodet 2009, Hadj-Youcef 2020, Orieux 2011, Orieux 2013]. In this thesis, we are particularly interested in the James Webb Space Telescope (JWST)[1] space mission.

The JWST, expected to be launched in October 2021, is the next space observatory of the National Aeronautics and Space Administration (NASA), in collaboration with the European Space Agency (ESA) and the Canadian Space Agency (CSA). It will be the largest and most complex telescope ever sent to space with a primary mirror of 6.5 meters in diameter (which is $\sim$ 10 times larger than for the previous infrared space observatories, ISO and Spitzer). The JWST incorporates several instruments that provide a unique and unprecedented combination of imagers and spectrometers, measuring a broad spectral window from the visible to the infrared range. Among these instruments, we particularly mention the Mid-InfraRed Instrument (MIRI). It contains an imager [Bouchet 2015], and an integral field spectrometer (IFS) [Vives 2008a], called Medium Resolution Spectroscopy (MRS) [Wells 2015], both observing the same infrared range (between 4.9 and 28.3 μm) but with very different spectral resolutions and spatial fields of view. The imager provides good spatial information in terms of detector sampling and observed field of view (74×113 arcseconds^2), but the spectral resolution is limited ($\lambda/\Delta\lambda \approx 5$)

[1] https://www.jwst.nasa.gov/

because of the wavelength integration over broad spectral filters. On the other hand, the MRS observes a relatively small field of view (up to 6.9×7.9 arcseconds^2) and provides measurements with insufficient spatial sampling but with high spectral resolution ($\lambda/\Delta\lambda \approx 1500 - 3500$). The 2D+$\lambda$ image reconstruction of the multi-spectral measurements provided by the broad-band imager, such as the imager of JWST/MIRI has been treated in a previous work [Hadj-Youcef 2020]. In this thesis, we are interested in the processing of 2D measurements provided by integral field spectrometer (IFS) instruments, such as the MRS of JWST/MIRI, in order to reconstruct a 2D+λ image with a high spatial and spectral resolutions.

1.2 Contributions

The reconstruction of a 2D+λ input image $\boldsymbol{x}$ from degraded 2D spectral measurements $\boldsymbol{y}$ with an inverse problem approach is treated following two main stages. In the first stage, we develop an explicit forward model for the IFS instrument that establishes a relationship between $\boldsymbol{y}$ and the unknown $\boldsymbol{x}$. This model identifies the response of each component of the acquisition instrument and allows the extraction of an observation matrix $\boldsymbol{H}$ and its transpose $\boldsymbol{H}^t$, used in the inverse problem algorithm. The forward model is general but primarily adapted for the MRS of JWST/MIRI. It involves relatively complex components and takes into account several effects, such as wavelength-dependent spatial and spectral blurring, different observations with varying spatial and spectral field of views (FOV) coming from different sources (spectral instruments, Integral Field Units, pointing of the instrument), and finally projections onto different 2D detectors with heterogeneous spatial and spectral sampling steps.

In the second stage, we propose a reconstruction algorithm that uses the developed forward model and the measurements $\boldsymbol{y}$ to estimate the unknown values of $\boldsymbol{x}$. The reconstruction problem, however, is ill-posed because of the ill-conditioning of $\boldsymbol{H}$. The proposed reconstruction is therefore based on the regularized least square approaches. It consists of minimizing a cost function composed of (1) a data fidelity term that relies on the description of the forward model and (2) a spatial and spectral regularization to ensure the stability of the solution. We particularly propose a convex spatial and spectral regularization for edge-preserving and solve the problem using a fast semi-quadratic algorithm based on Geman and Reynolds formulation [Geman 1992] to estimate the solution.

In further work, we consider a new linear model for the 2D+λ input image $\boldsymbol{x}$ while preserving its spatial and spectral distributions. More particularly, we assume that $\boldsymbol{x}$ lives in a low dimensional subspace, and is represented by a small number of spectral components $\mathbf{s}$, assumed known, weighted by unknown mixing coefficients $\boldsymbol{a}$. Based on this input model, known as the Linear Mixing Model (LMM), we formulate a new forward model that includes the known spectral components and relates the measurements $\boldsymbol{y}$ to the unknown mixing coefficients $\boldsymbol{a}$. The reconstruction algorithm uses the new forward model to estimate the unknown mixing coefficients

$\boldsymbol{a}$ from the measurements $\boldsymbol{y}$. The new reconstruction algorithm requires only a convex spatial edge-preserving regularization since the spectral resolution of the reconstructed HS image is imposed by the known spectral components $\mathbf{s}$. We finally solve the problem using a high efficient optimization algorithm, which is the iterative Majorize-Minimize Memory gradient (3MG) algorithm [Chouzenoux 2011].

To validate the proposed reconstruction algorithms for both input models, we simulate high spectral measurements, using both forward models respectively, from several synthetic hyperspectral inputs with different spatial and spectral distributions. The overall proposed algorithms for both the spatio-spectral and the linear mixing object models show good performances and a significant increase of the spatial and spectral resolution of the reconstructed 2D+λ image compared to other reconstruction algorithms, particularly the classic l_2 regularization [Tikhonov 1995] and the shift-and-add algorithm [Hook 2000, Farsiu 2003] for multi-frame SR reconstructions.

1.3 Outline of this thesis

The following chapters are organized as follows. Chapter 2 presents an overview of the inverse problem framework as an ill-posed problem and discusses several methods and algorithms to solve the inverse problem and reconstruct 2D+λ HS images. Chapter 3 describes the characteristics of the Integral Field Spectrometer (IFS) instruments, in particular, the MRS of JWST/MIRI. Chapters 4 and 5 deal with the reconstruction of a discrete 2D+λ input image from spatially and spectrally degraded 2D spectral measurements using a spatio-spectral model and a linear mixing model for the input, respectively. Finally, we provide a general conclusion and perspectives in Chapter 6.

1.4 Publications

- R. Abi-rizk, F. Orieux and A. Abergel, "Reconstruction hyperspectrale à haute résolution à partir de mesures de spectrometrie", 27eme Colloque GRETSI Traitement du Signal et des Images, GRETSI 2019
- R. Abi-rizk, F. Orieux and A. Abergel, "Non-Stationary Hyperspectral Forward Model and High-Resolution," 2020 IEEE International Conference on Image Processing (ICIP), 2020.
- R. Abi-rizk, F. Orieux and A. Abergel,"Super-Resolution Hyperspectral Reconstruction with Majorization-Minimization Algorithm and Low-Rank Approximation," 2021 (submitted).

Chapter 2

Inverse Problems

Contents

In this thesis, we are interested in the inverse problem approach, mainly used to reconstruct 2D+λ images from degraded measurements provided by astronomical instruments. In the first section of this chapter, we provide a general paradigm of the inverse problem approaches and address the related limitations, techniques, and algorithms. The second section presents several works and methods to reconstruct 2D+λ images with a high spatial and spectral resolution, particularly the Hyperspectral (HS) images, using the inverse problem approaches.

2.1 Inverse problem framework

The inverse problem is the process of estimating and reconstructing an unknown input object $\boldsymbol{x} \in \mathbb{R}^N$ from an output measurement $\boldsymbol{y} \in \mathbb{R}^M$ provided by an observation system (*i.e.* telescope, camera, microscope, etc). $\boldsymbol{x}$ and $\boldsymbol{y}$ are not necessarily

limited to one dimension but can represent a two-dimensional image or a Hyperspectral image, denoted as vectors in this section. We denote $\boldsymbol{H} \in \mathbb{R}^{M \times N}$ a linear operator describing the response of the observation system and providing a relationship between the input $\boldsymbol{x}$ and the output $\boldsymbol{y}$, shown in Fig. 2.1 and described as

$$\boldsymbol{y} = \boldsymbol{H}\boldsymbol{x} + \boldsymbol{\epsilon} \tag{2.1}$$

where $\boldsymbol{\epsilon} \in \mathbb{R}^{M}$ denotes a vector of errors. The model in Eq. (2.1) is called a forward problem that describes the formation of the measurements. Generally, the observation matrix $\boldsymbol{H}$ can be identified and modeled. Hence, the inverse problem relies on estimating $\boldsymbol{x}$ from the known $\boldsymbol{H}$ and measurements $\boldsymbol{y}$ [Demoment 1989]. However, in some other cases, $\boldsymbol{H}$ is unknown or partially known and requires a full or a partial estimation along with $\boldsymbol{x}$. In these cases, the inverse problem is approached in a blind [Almeida 2010] or semi-blind [Yu-Li You 1999] fashion.

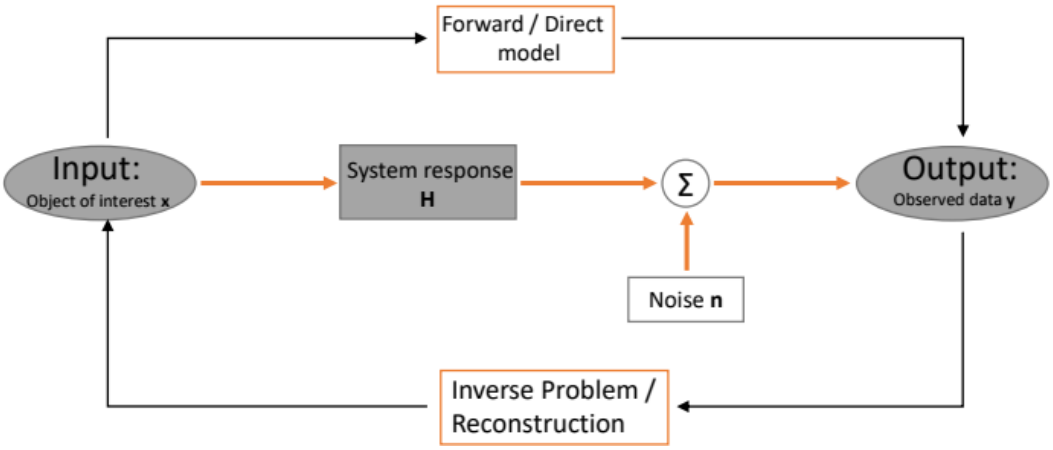

Figure 2.1: A scheme of the inverse problem process.

2.1.1 Ill posed problem

Solving an inverse problem is challenging because it is generally "ill-posed". Hadamard [Hadamard 1902] imposed several mathematical properties that should be respected to consider the inverse problem "well-posed". These properties are (1) the existence of the solution, (2) the uniqueness of the solution, and (3) the stability of the solution (the solution continuously depends on the measurements). If one or more of these properties are violated, the reconstruction problem is considered "ill-posed". For instance, if the observation matrix $\boldsymbol{H}$ is square ($M = N$) and invertible ($\mathrm{Ker}\boldsymbol{H} = \{0\}$), a straightforward solution to the inverse problem might be considered as [Demoment 1989, Idier 2001b]

$$\hat{\boldsymbol{x}} = \boldsymbol{H}^{-1}\boldsymbol{y} \tag{2.2}$$

where $\hat{\boldsymbol{x}}$ denotes the estimated input (the solution of the inverse problem). In other cases, Eq. (2.2) is inapplicable. Moreover, since the measurements $\boldsymbol{y}$ are subject to errors introduced by the additional term $\boldsymbol{\epsilon}$, the solution of Eq. (2.2) is not expected to be accurate. For these reasons, it is crucial to develop new alternative to the direct inversion that can solve the inverse problems. These theories include, for instance, the "generalized inversion" and the regularization [Idier 2001b].

A natural approach is the least square approach consisting of minimizing the square of the distance between the observation vector $\boldsymbol{y}$ and the model output $\boldsymbol{Hx}$ yielding to

$$\hat{\boldsymbol{x}}_s \quad \text{minimize} \quad \|\boldsymbol{y} - \boldsymbol{Hx}\|_2^2 \tag{2.3}$$

where $\hat{\boldsymbol{x}}_s$ is the solution of the following linear system

$$\boldsymbol{H}^t\boldsymbol{Hx} = \boldsymbol{H}^t\boldsymbol{y}. \tag{2.4}$$

In the discrete case, the linear operator generally lives in a finite-dimensional space. Therefore, at least one minimizer $\hat{\boldsymbol{x}}_s$ exists and depends continuously on the measurements (this condition is necessary but not sufficient) [Idier 2001b]. However, the problem might remain ill-posed in the sense of Hadamard because the uniqueness of the solution is not necessarily guaranteed (*i.e.* the problem is under-determined). In that case, the "generalized inversion" might be considered by selecting the minimizer $\hat{\boldsymbol{x}} \in \hat{\boldsymbol{x}}_s$ with the minimal norm. The "generalized inversion" problem remains in most cases ill-posed because the matrix $\boldsymbol{H}^t\boldsymbol{H}$ is ill-conditioned. In fact, $\boldsymbol{H}^t\boldsymbol{H}$ might contain eigenvalues close to zero. Consequently, small perturbations in the measurements $\boldsymbol{y}$ can result in high perturbations in $\hat{\boldsymbol{x}}$ [Idier 2001b] as illustrated in Fig 2.2(c).

2.1.2 Regularized least square approaches

The regularization theory was established in general to correct the ill-conditioning of the matrix $\boldsymbol{H}^t\boldsymbol{H}$ in Eq. (2.4) by enforcing one or multiple regularization terms to estimate a stable solution $\hat{\boldsymbol{x}}$ close to $\boldsymbol{x}$. We first define an objective (or cost) function that denotes $\mathcal{J}$ as [Idier 2001b, Tikhonov 1995]

$$\mathcal{J}(\boldsymbol{x}) = \|\boldsymbol{y} - \boldsymbol{Hx}\|_2^2 + \mu\mathcal{R}(\boldsymbol{x}). \tag{2.5}$$

The objective function $\mathcal{J}$ is composed of two terms. The first one is the data fidelity term that measures the square of the distance between $\boldsymbol{y}$ and $\boldsymbol{Hx}$, and the second one is the added regularization term R, which enforces a *priori* knowledge of the solution. The parameter μ is a regularization parameter that is set to find the best compromise between the data fidelity term and the regularization term. This parameter is highly sensitive to the modeling errors and noise in $\boldsymbol{\epsilon}$. The choice of the regularization term $R(\boldsymbol{x})$ strongly depends on the nature of the object. For instance, a regularization term that enforces smoothness is considered if the distribution of the input object is expected to be smooth or uniform, and a regularization term

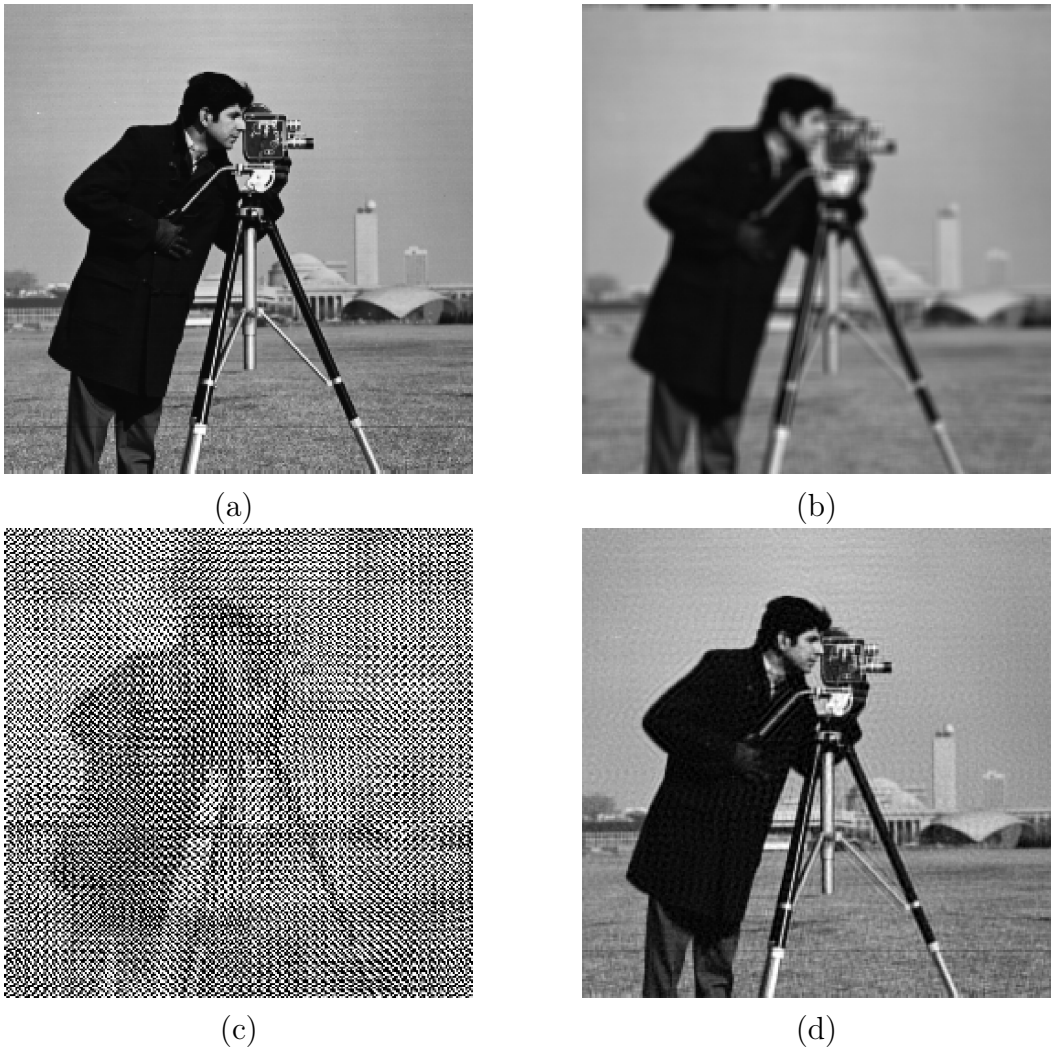

Figure 2.2: Ill conditioned inverse filter. (a): original 2D image of *cameraman* from the Matlab Image processing Toolbox. (b): output image degraded by a 2D square convolution kernel, and corrupted with an additive white Gaussian noise, (c): solution with an inverse filter, (d): regularized least square solution, with an l_2 regularization

that preserves sharp edges is considered if the object contains high discontinuities we want to preserve. Next, we present the regularized least square approaches with several regularization terms used to estimate $\boldsymbol{x}$.

2.1.2.1 Tikhonov regularization

The first proposed choice of $\mathcal{R}(\boldsymbol{x})$ is the Tikhonov regularization (l_2 norm) [Tikhonov 1995]. The associated objective function writes

$$\mathcal{J}_{l_2}(\boldsymbol{x}) = \|\boldsymbol{y} - \boldsymbol{H}\boldsymbol{x}\|_2^2 + \mu\|\boldsymbol{V}\boldsymbol{x}\|^2. \tag{2.6}$$

with $\boldsymbol{V}$ a linear operator. $\mathcal{J}_{l_2}$ is quadratic since the data fidelity term and the regularization term are both quadratics (*see Fig.* 2.3(a)). Moreover, $\mathcal{J}_{l_2}$ is strictly convex with a unique global minimum if $Ker\boldsymbol{H} \bigcap Ker\boldsymbol{V} = \{0\}$. Therefore, the unique solution $\hat{\boldsymbol{x}}$ of the inverse problem is obtained as the minimizer of the objective function $\mathcal{J}_{l_2}$ with

$$\hat{\boldsymbol{x}} = \underset{\boldsymbol{x}}{\operatorname{argmin}} \{\mathcal{J}(\boldsymbol{x}) = (\boldsymbol{H}^t\boldsymbol{H} + \mu\boldsymbol{V}^t\boldsymbol{V})^{-1}\boldsymbol{H}^t\boldsymbol{y}\}. \tag{2.7}$$

Eq. (2.7) yields to an explicit closed-form expression of the minimizer $\hat{\boldsymbol{x}}$. In most applications, $\boldsymbol{V}$ is a difference operator, hence, the l_2 regularization enforces smoothness to the solution by penalizing the difference between the elements of $\boldsymbol{x}$ (*i.e.* pixels in the case of a 2D image). However, it introduces artifacts to the solution, particularly around the high gradient values that will limit the ability to restore the sharp edges (*i.e.* contours of images), as shown in (Fig. 2.2(d)). Therefore, non-quadratic regularization terms, such as the total variation (TV) [Rudin 1992] and the half-quadratic regularization [Idier 2001a, Charbonnier 1997], might be considered to preserve the high gradient values of the estimated solution.

2.1.2.2 Total variation

The total variation (TV) [Rudin 1992], based on the l_1-norm, is a regularization approach that preserves the high gradient values of the input. The solution is estimated by minimizing the following objective function, denoted $\mathcal{J}_{l_1}$

$$\hat{\boldsymbol{x}} = \underset{\boldsymbol{x}}{\operatorname{argmin}} \{\mathcal{J}_{l_1}(\boldsymbol{x}) = \|\boldsymbol{y} - \boldsymbol{H}\boldsymbol{x}\|_2^2 + \mu|\nabla\boldsymbol{x}|_1\} \tag{2.8}$$

where $\nabla\boldsymbol{x}$ computes the first gradient of $\boldsymbol{x}$. Unlike the quadratic objective function in Eq. (2.7), $|\nabla\boldsymbol{x}|_1$ is not differentiable at zero, and the closed-form expression of the minimizer $\hat{\boldsymbol{x}}$ is not explicit and cannot be directly calculated. Therefore, iterative algorithms are used to estimate the solution. Such algorithms include the splitting Bregman proposed in [Goldstein 2009] and the first-order primal-dual proposed in [Chambolle 2011]. Moreover, the TV method introduces a cartoon-like effects.

2.1.2.3 Half quadratic regularization

Another family of regularization, known as the half-quadratic (HQ) [Idier 2001a], is used to promote high gradient values to the solution. Unlike the previous regularization, HQ promotes smoothness to the continuous regions of the solution while

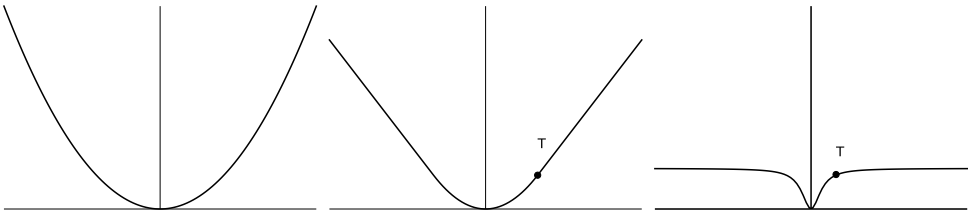

Figure 2.3: Different potential functions: (a) quadratic potential functionn (b) convex l_2l_1 huber potential function, (c) non convex l_2l_0 Geman and McClure function. The parameter T in (b) and (c) refers to the threshold. Below this threshold, the functions have a quadratic behaviour, and above it is linear or constant.

preventing excessive penalization of the high gradient values. We first introduce a general form of the regularization term as

$$\mathcal{R}(\boldsymbol{x}) = \sum_{w=1}^{W} \phi(\boldsymbol{v}_w \boldsymbol{x}) \tag{2.9}$$

with $\phi : \mathbb{R} \to \mathbb{R}$ is a differentiable potential function. For instance, when $\phi(\delta) = \|\delta\|^2$, $R(\boldsymbol{x}) = \|\boldsymbol{V}\boldsymbol{x}\|^2$, hence the quadratic regularization. We are particularly interested in the convex potential functions $\phi(\delta)$ used for edge-preserving. The convex potential functions are (l_2l_1-norm) takes a quadratic behaviour below a fixed threshold T and a linear behaviour above it to preserve the edges (Fig. 2.3(b)). Among these l_2l_1 potential functions [Charbonnier 1997] we mention:

- The Huber potential function

$$\phi(\delta, T) = \begin{cases} \delta^2, & \text{if } |\delta| \leq T \\ 2T|\delta| - T^2 & \text{otherwise.} \end{cases} \tag{2.10}$$

- The Hyperbolic potential functions

$$\phi(\delta, T) = \sqrt{1 + \frac{\delta^2}{T^2}} - 1. \tag{2.11}$$

On the other hand, the non-convex potential functions (l_2l_0-norm) takes a quadratic behaviour below a fixed threshold T and a constant behaviour above it (Fig. 2.3(c)). Typical example of l_2l_0 potentials is the Geman-McClure with

$$\phi(\delta, T) = \frac{\delta^2}{2T^2 + \delta^2}. \tag{2.12}$$

The regularized least square approaches with an edge-preserving regularization relies on the optimization of a non-quadratic objective function, $\mathcal{J}_{l_2l_1}$, that writes

$$\hat{\boldsymbol{x}} = \underset{\boldsymbol{x}}{\operatorname{argmin}}\, \mathcal{J}_{l_2l_1}(\boldsymbol{x}) = \|\boldsymbol{y} - \boldsymbol{H}\boldsymbol{x}\|_2^2 + \mu \sum_{w=1}^{W} \phi(\boldsymbol{v}_w^t \boldsymbol{x}). \tag{2.13}$$

where $\boldsymbol{v}_w$ computes the first order difference between the elements of $\boldsymbol{x}$ and ϕ is a convex potential function (*i.e.* Huber). Unfortunately, an explicit form of the minimizer $\hat{\boldsymbol{x}}$ of $\mathcal{J}_{l_2l_1}$ is not available and cannot be directly calculated. The optimization of a non-quadratic function with a convex regularization for edge-preserving in Eq. (2.13) can be structured into a simpler problem by considering a half-quadratic form. This new form consists of introducing to the convex potential function a set of auxiliary variables $\boldsymbol{b} = (b_w)_{w\in\mathcal{W}}$ [Idier 2001a]. ϕ can therefore be expressed as a function of a quadratic surrogate function Q and a dual auxiliary function $\psi(b)$, related to ϕ (with respect to the auxiliary variable b) that writes

$$\phi(b) = \inf_{b\in\{0,b_\infty\}} \left\{Q(\delta, b) + \psi(b)\right\}, \quad \forall\delta \in \mathbb{R} \tag{2.14}$$

To address the half-quadratic reconstruction, we define a new augmented objective function $\mathcal{J}^*_{l_2l_1}$ as

$$\mathcal{J}^*_{l_2l_1}(\boldsymbol{x}, \boldsymbol{b}) = \|\boldsymbol{y} - \boldsymbol{H}\boldsymbol{x}\|^2 + \mu \sum_{w=1}^{W} \Big(Q(\boldsymbol{v}_w^t\boldsymbol{x}, b_w) + \psi(b_w)\Big). \tag{2.15}$$

The augmented objective function $\mathcal{J}^*_{l_2l_1}$ includes a least-square term measuring the fidelity to the data, a quadratic surrogate function Q expressing the difference between the elements $(\boldsymbol{v}_w^t\boldsymbol{x})_{w\in\mathcal{W}}$ (*i.e.* pixels of an image) and depends on $(b_w)_{w\in\mathcal{W}}$ and an auxiliary function ψ that depends solely on $(b_w)_{w\in\mathcal{W}}$. Moreover, the augmented auxiliary variables $(b_w)_{w\in\mathcal{W}}$ are proportional to $(\boldsymbol{v}_w^t\boldsymbol{x})_{w\in\mathcal{W}}$. The higher the gradient, the higher the auxiliary variables.

From Eq.(2.14) and Eq.(2.15), the augmented objective function $\mathcal{J}^*_{l_2l_1}(\boldsymbol{x}, \boldsymbol{b})$ shares the same minimizer as $\mathcal{J}_{l_2l_1}(\boldsymbol{x})$ with

$$\min_{b} \mathcal{J}^*_{l_2l_1}(\boldsymbol{x}, \boldsymbol{b}) = \mathcal{J}_{l_2l_1}(\boldsymbol{x}). \tag{2.16}$$

Two different formulations of the half-quadratic regularization have been proposed to solve Eq.(2.15). Geman and Reynolds (GR) [Geman 1992] were the first to propose a multiplicative form of the quadratic surrogate function Q, whereas Geman and Yang (GY) [Geman 1995] proposed an additive form of this function a few years later. Both formulations provide iterative optimization algorithms that benefit from a global convergence. The augmented objective function with GR and GY formulations respectively writes

$$\mathcal{J}^*_{GR}(\boldsymbol{x}, \boldsymbol{b}) = \|\boldsymbol{y} - \boldsymbol{H}\boldsymbol{x}\|^2 + \mu \sum_{w=1}^{W} b_w(\boldsymbol{v}_w^t\boldsymbol{x})^2 + \psi(b_w), \tag{2.17}$$

$$\mathcal{J}^*_{GY}(\boldsymbol{x}, \boldsymbol{b}) = \|\boldsymbol{y} - \boldsymbol{H}\boldsymbol{x}\|^2 + \mu \sum_{w=1}^{W} (\boldsymbol{v}_w^t\boldsymbol{x} - b_w)^2 + \psi(b_w). \tag{2.18}$$

Eq.(2.17) and Eq.(2.18) are solved by iteratively alternating two minimization problems until convergence [Idier 2001a, Charbonnier 1997]

$$\hat{\boldsymbol{x}}^{(k)} = \arg\min_{\boldsymbol{x}} \mathcal{J}^{*}_{l_2 l_1}\left(\boldsymbol{x}, \boldsymbol{b}^{(k-1)}\right) \tag{2.19}$$

$$\hat{\boldsymbol{b}}^{(k)} = \arg\min_{\boldsymbol{b}} \mathcal{J}^{*}_{l_2 l_1}\left(\boldsymbol{x}^{(k)}, \boldsymbol{b}\right) \tag{2.20}$$

Eq. (2.19) corresponds to the minimization for each iteration (k) of $\mathcal{J}^{*}_{GR}$ and $\mathcal{J}^{*}_{GY}$ with respect to (w.r.t) $\boldsymbol{x}$ for a fixed $\boldsymbol{b}$ with [Idier 2001a]

$$\hat{\boldsymbol{x}}_{GR} = \arg\min_{\boldsymbol{x}} \left\{ \|\boldsymbol{y} - \boldsymbol{H}\boldsymbol{x}\|^2 + \frac{\mu}{2} \boldsymbol{x}^t \boldsymbol{V}^t \boldsymbol{B} \boldsymbol{V} \boldsymbol{x} \right\}, \tag{2.21}$$

$$\hat{\boldsymbol{x}}_{GY} = \arg\min_{\boldsymbol{x}} \left\{ \|\boldsymbol{y} - \boldsymbol{H}\boldsymbol{x}\|^2 + \frac{\mu}{2} \|\boldsymbol{V}\boldsymbol{x} - \boldsymbol{b}\|^2 \right\}, \tag{2.22}$$

where $\boldsymbol{B} = \text{Diag}(\boldsymbol{b})$ and $\boldsymbol{V} = [\boldsymbol{v}_1 \dots \boldsymbol{v}_W]$. Hence $\hat{\boldsymbol{x}}_{GR}$ and $\hat{\boldsymbol{x}}_{GY}$ are deduced by solving the following linear systems respectively

$$\boldsymbol{A}_{GR}(\boldsymbol{x}) = (\boldsymbol{H}^t \boldsymbol{y}), \tag{2.23}$$

$$\boldsymbol{A}_{GY}(\boldsymbol{x}) = (\boldsymbol{H}^t \boldsymbol{y} + \mu \boldsymbol{V}^t \boldsymbol{b}), \tag{2.24}$$

where the Normal matrices $\boldsymbol{A}_{GR} = (\boldsymbol{H}^t\boldsymbol{H} + \mu \boldsymbol{V}^t \boldsymbol{B} \boldsymbol{V})$ and $\boldsymbol{A}_{GY} = (\boldsymbol{H}^t\boldsymbol{H} + \mu \boldsymbol{V}^t \boldsymbol{V})$ are symmetric positive definite, hence, can be inverted if the conditions $\left(Ker\{\boldsymbol{H}^t\boldsymbol{H}\} \bigcap Ker\{\boldsymbol{V}^t\boldsymbol{B}\boldsymbol{V}\}\right) = \{0\}$ and $\left(Ker\{\boldsymbol{H}^t\boldsymbol{H}\} \bigcap Ker\{\boldsymbol{V}^t\boldsymbol{V}\}\right) = \{0\}$ are respected for GR and GY formulations, respectively. Eq. (2.23) and (2.24) yields to a closed-form expression of the minimizer $\hat{\boldsymbol{x}}_{GR}$ and $\hat{\boldsymbol{x}}_{GY}$ respectively. However, computing the inverse of the normal matrices for each iteration (k) is untractable, particularly for large-size problems since the sizes of these matrices are related to the number of unknowns [Allain 2006].

In some cases, a numerical analysis might be considered to compute the exact solution of the Normal equation in Eq. (2.23) and (2.24), depending on the structural properties of the observation matrix $\boldsymbol{H}$. For instance, when $\boldsymbol{H}$ has a Toeplitz or a Toeplitz-block-Toeplitz structure (*i.e.* $\boldsymbol{H}$ is a convolution matrix), it can be, under circular approximation assumption, diagonalized in the Fourier domain at a low cost [Hunt 1971, Allain 2006]. In that case, computing the inverse of the Normal matrix $\boldsymbol{A}_{GY}$ can be efficiently done. Unfortunately, this is not the case for $\boldsymbol{A}_{GR}$ since it depends on the auxiliary variables $\boldsymbol{b}$. Moreover, in more realistic problems, $\boldsymbol{H}$ does not always benefit from such simple structures. Therefore, it is natural to propose alternative methods that approach the resolution of the linear system but at a much lower cost, such as iterative optimization algorithms [Shewchuk 1994, Nocedal 2006], presented in the following section.

On the other hand, sovling Eq. (2.20) corresponds to the minimization of $\mathcal{J}^{*}_{HQ}$

w.r.t $\boldsymbol{b}$ for a fixed $\boldsymbol{x}$ yielding to

$$\hat{\boldsymbol{b}}_{GR} = \arg\min_{b_w} \left\{ \frac{\mu}{2} \sum_{w \in \mathcal{W}} b_w (\boldsymbol{v}_w^t \boldsymbol{x})^2 + \psi(b_w) \right\}. \tag{2.25}$$

$$\hat{\boldsymbol{b}}_{GY} = \arg\min_{b_w} \left\{ \frac{\mu}{2} \sum_{w \in \mathcal{W}} (\boldsymbol{v}_w^t \boldsymbol{x} - b_w)^2 + \psi(b_w) \right\}. \tag{2.26}$$

The minimization problem in Eq. (2.25) and (2.26) for the GR and GY formulations, respectively, can be achieved in parallel for each $b_w \in \boldsymbol{b}$. Moreover, b_w are expressed explicitly and does not require a known form of the function ψ since the infimum in Eq. (2.14) is uniquely reached when

$$b_{GR} = \frac{\phi'(\boldsymbol{v}_w^t \boldsymbol{x})}{2\boldsymbol{v}_w^t \boldsymbol{x}} \tag{2.27}$$

$$b_{GY} = \boldsymbol{v}_w^t \boldsymbol{x} - \phi'(\boldsymbol{v}_w^t \boldsymbol{x}) \tag{2.28}$$

with ϕ' is the first order derivative of the convex ($l_2 l_1$) potential function (*i.e.* Huber).

2.1.3 Gradient-based iterative optimization algorithms

As detailed in the previous sections, the inverse problem can be solved by minimizing a regularized objective function $\mathcal{J}(\boldsymbol{x})$ that writes

$$\mathcal{J}(\boldsymbol{x}) = \|\boldsymbol{y} - \boldsymbol{H}\boldsymbol{x}\|_2^2 + \mu \sum_{w=1}^{W} \phi(\boldsymbol{v}_w \boldsymbol{x}) \tag{2.29}$$

We consider the problem where $\phi : \mathbb{R} \to \mathbb{R}$ is a differentiable and strictly convex potential function. Thus, if $\left(Ker\{\boldsymbol{H}^t\boldsymbol{H}\} \bigcap Ker\{\boldsymbol{V}^t\boldsymbol{V}\} \right) = \{0\}$, the objective function $\mathcal{J}$ is also convex and the optimizer $\hat{\boldsymbol{x}}$ of the problem is global and unique [Idier 2001b]. Minimizing Eq. (2.29) depends heavily on the structure of $\mathcal{J}$. For instance, when the regularization is quadratic, minimizing Eq. (2.29) with respect to $\boldsymbol{x}$ yields to unique closed-form expression of $\hat{\boldsymbol{x}}$. However, solving the problem is untractable, mainly when the unknown $\boldsymbol{x}$ is high-dimensional. When a non-quadratic regularization is considered, no analytic form expression of $\hat{\boldsymbol{x}}$ is available. In both cases, alternative methods such as iterative algorithms are approached to solve the problem. We are mainly interested in the family of iterative algorithms that use the gradient of $\mathcal{J}$, such as the gradient descent algorithms [Shewchuk 1994, Nocedal 2006]. These algorithms do not compute exact solution $\hat{\boldsymbol{x}}$ but rather approach sufficiently a local minimum that corresponds to a global minimum when the function is convex.

Starting from an initial value $\boldsymbol{x}^{(0)}$, the gradient descent algorithms generates a sequence of iterates $\boldsymbol{x}^{(k)}$ with $k = \{0 \dots K\}$ converging towards the solution $\hat{\boldsymbol{x}}$ with

$$\boldsymbol{x}^{(k+1)} = \boldsymbol{x}^{(k)} + \alpha^{(k)} \boldsymbol{d}^{(k)}. \tag{2.30}$$

$\boldsymbol{d}^{(k)}$ is the descent direction that ensures the monotonic decrease of the objective function

$$\mathcal{J}(\boldsymbol{x}^{(k+1)}) < \mathcal{J}(\boldsymbol{x}^{(k)}) \tag{2.31}$$

and $\alpha^{(k)}$ is the stepsize that describes how much the function decreases at each iteration. The convergence of the iterative descent algorithms is ensured when the objective function monotonically decreases between iterations and when the step size value is well chosen. For a minimum value of α, the optimization algorithm converges very slowly and might not reach convergence points if the number of iterations chosen is not high enough. On the other hand, a large step size value accelerates the algorithm but might lead to divergence. Finding the correct step size value that ensures the convergence of the algorithm is called line search and can be obtained by minimizing the following scalar function $j(\alpha)$ [Nocedal 2006]

$$j(\alpha) = \mathcal{J}\Big(\boldsymbol{x}^{(k)} + \alpha^{(k)}\boldsymbol{d}^{(k)}\Big). \tag{2.32}$$

Unfortunately, when $\mathcal{J}$ is a non-quadratic objective function, it is usually not easy to define nor to implement a converging line search [Labat 2008, Chouzenoux 2011]. On the other hand, when the objective function is quadratic, it precludes an optimal closed-form step-size.

We are particularly interested here in the iterative descent algorithms that minimize a regularized non-quadratic objective function with a convex regularization for edge-preserving. In section 2.1.2.3, we saw that no analytical form exists to solve the problem. Therefore, the Half Quadratic (HQ) algorithms with GR [Geman 1992] or GY [Geman 1995] formulations, used in section 2.1.2.3 were considered to provide a simpler solution than a direct minimization of Eq. (2.29). HQ approaches consisted on minimizing an augmented function $\mathcal{J}^*(\boldsymbol{x}, \boldsymbol{b})$ that depends on auxiliary variables $\boldsymbol{b}$. Thus, instead of using the line search strategy, the minimization of the problem w.r.t $\boldsymbol{x}$ is quadratic and can be computed using the iterative optimization algorithms with a pre-defined step size. The quadratic optimization problem amounts to solve a large system of linear equations with [Shewchuk 1994]

$$\boldsymbol{A}\boldsymbol{x} = \boldsymbol{\nu} \tag{2.33}$$

with $\boldsymbol{\nu}$ is a known vector, $\boldsymbol{A}$ is a square, positive definite matrix, for instance, $\boldsymbol{A}_{GR}$ and $\boldsymbol{A}_{GY}$ defined in Eq. (2.23) and Eq. (2.24). In addition, $\boldsymbol{x}$ is the unknown object. We present the most common descent direction algorithms in the field of image processing to minimize quadratic functions, namely the steepest descent algorithms and the conjugate gradient to solve (2.33) For a detailed discussion of the iterative optimization algorithms for quadratic functions, we invite the readers to consult [Shewchuk 1994, Nocedal 2006]

2.1.3.1 Gradient descent algorithm

The gradient descent optimization algorithm chooses as the direction the opposite of the gradient, in which $\mathcal{J}$ decreases most quickly. Let $\boldsymbol{J} = \nabla\mathcal{J}$ denotes the first

gradient of $\mathcal{J}$, the chosen direction writes

$$\boldsymbol{d}^{(k)} = -\boldsymbol{J}^{(k)}. \tag{2.34}$$

The steepest descent algorithm is detailed in Algorithm 1. The simplicity of this

Algorithm 1: Steepest descent algorithm

Input: $\boldsymbol{A}$, $\boldsymbol{\nu}$
Initialize: $\hat{\boldsymbol{x}}^{(0)}$ = arbitrary
while k $\leqslant$ K
    Direction of the steepest descent
    $\boldsymbol{d}^{(k)} = \boldsymbol{\nu} - \boldsymbol{A}\hat{\boldsymbol{x}}^{(k)}$
    Closed form of the stepsize
    $\alpha^{(k)} = \dfrac{\boldsymbol{d}^{t(k)}\boldsymbol{d}^{(k)}}{\boldsymbol{d}^{t(k)}\boldsymbol{A}\boldsymbol{d}^{(k)}}$
    Update $\hat{\boldsymbol{x}}$
    $\hat{\boldsymbol{x}}^{(k+1)} = \hat{\boldsymbol{x}}^{(k)} + \alpha^{(k)}\boldsymbol{d}^{(k)}$

algorithm and the choice of the descent direction make the steepest descent practical. Moreover, the step size $\alpha^{(k)}$ is computed analytically. However, the convergence is slow, and the algorithm requires many iterations to reach the convergence, yielding an increase in the computational cost.

2.1.3.2 Linear Conjugate Gradient algorithms

At the iteration k, the steepest descent algorithm might take steps in the same direction as the previous steps, mainly because $\boldsymbol{d}^{(k+1)}$ depends only from the previous direction $\boldsymbol{d}^{(k)}$ [Fletcher 1964, Shewchuk 1994]. The linear conjugate gradient algorithm ensures different directions between the iterations by considering $\boldsymbol{A}$-orthogonal descent directions $\boldsymbol{d}^{(0)} \dots \boldsymbol{d}^{(k-1)}$ with

$$\boldsymbol{d}^{t(i)}\boldsymbol{A}\boldsymbol{d}^{(j)} = 0 \qquad \text{for } i \neq j. \tag{2.35}$$

The set of $\boldsymbol{d}$ are computed ensuring that $\boldsymbol{d}^{(k+1)}$ is a linear combination of $\boldsymbol{J}^{(k+1)}$ and $\{\boldsymbol{d}^{(0)} \dots \boldsymbol{d}^{(k)}\}$ with

$$\boldsymbol{d}^{(k)} \begin{cases} -\boldsymbol{J}^{(k)} & \text{for } k = 0 \\ -\boldsymbol{J}^{(k)} + \beta^{(k)}\boldsymbol{d}^{(k-1)} & \text{for } k \geq 1. \end{cases} \tag{2.36}$$

with $\boldsymbol{J}^{(k)}$ is the first gradient of $\mathcal{J}$ at the iteration k and β a parameter ensuring the conjugacy between $\boldsymbol{d}^{(k)}$ and $\boldsymbol{d}^{(k-1)}$. The conjugate gradient is initially developed to minimize quadratic functions by choosing $\beta^{(k)}$ [Fletcher 1964]

$$\beta^{(k)} = \frac{\boldsymbol{J}^{t(k)}\boldsymbol{J}_k}{\boldsymbol{J}^{t(k-1)}\boldsymbol{J}^{(k-1)}} \tag{2.37}$$

The linear conjugate gradient method is given in algorithm. 2

Algorithm 2: Linear Conjugate Gradient algorithm

Input: $\boldsymbol{A}$, $\boldsymbol{\nu}$
Initialize: $\hat{\boldsymbol{x}}^{(0)} = \text{arbitrary}$
$\boldsymbol{J}_0 = \boldsymbol{A}\hat{\boldsymbol{x}}^{(0)} - \boldsymbol{\nu}$ and $\boldsymbol{d}^{(0)} = -\boldsymbol{J}^{(0)}$
while k $\leqslant$ K **do**:
Closed form of the stepsize
$\alpha^{(k)} = \dfrac{\boldsymbol{J}^{t(k)}\boldsymbol{J}^{(k)}}{\boldsymbol{d}^{t(k)}\boldsymbol{A}\boldsymbol{d}^{(k)}}$
Update $\hat{\boldsymbol{x}}$
$\hat{\boldsymbol{x}}^{(k+1)} = \hat{\boldsymbol{x}}^{(k)} + \alpha^{(k)}\boldsymbol{d}^{(k)}$
Conjugate direction
$\boldsymbol{J}^{(k+1)} = \boldsymbol{A}\hat{\boldsymbol{x}}^{(k+1)}\boldsymbol{\nu}$
$\beta^{(k)} = \dfrac{\boldsymbol{J}^{t(k+1)}\boldsymbol{J}^{(k+1)}}{\boldsymbol{J}^{t(k)}\boldsymbol{J}^{(k)}}$
$\boldsymbol{d}^{(k+1)} = -\boldsymbol{J}^{(k+1)} + \beta^{(k)}\boldsymbol{d}^{(k)}$

2.1.4 Quadratic Majorize-Minimize approach

We showed in the previous section that the HQ approaches could be efficiently solved using the iterative optimization algorithms with an analytic form of the step size. In this section, we discuss a more generic approach to minimize a non-quadratic function with a convex regularization based on the Majorize-Minimize (MM) methods. It consists of successively minimizing a quadratic surrogate function $\boldsymbol{Q}\left(\boldsymbol{x}, \boldsymbol{x}^{(k)}\right)$ that majorizes $\mathcal{J}(\boldsymbol{x})$, writing [Allain 2006]

$$Q\left(\boldsymbol{x}, \boldsymbol{x}^{(k)}\right) = \mathcal{J}\left(\boldsymbol{x}^{(k)}\right) + \nabla\mathcal{J}\left(\boldsymbol{x}^{(k)}\right)^t\left(\boldsymbol{x} - \boldsymbol{x}^{(k)}\right) + \frac{1}{2}\left(\boldsymbol{x} - \boldsymbol{x}^{(k)}\right)^t\boldsymbol{A}\left(\boldsymbol{x}^{(k)}\right)\left(\boldsymbol{x} - \boldsymbol{x}^{(k)}\right). \tag{2.38}$$

where $\nabla\left(\mathcal{J}(\boldsymbol{x}^{(k)})\right)$ reads the gradient of $\mathcal{J}(\boldsymbol{x})$, and $\boldsymbol{A}(\boldsymbol{x})$ is a positive definite operator. In addition, with the following assumptions (**A1** and **A2**) for the scalar function ϕ [Chouzenoux 2011]

A1

1. ϕ is $\mathcal{C}^1$ and coercive,
2. ϕ is $\mathcal{L}$ - Lipschitz,

A2

1. $\mathcal{C}^1$, even, coercive,
2. $\phi(\sqrt{\cdot})$ is concave on $\mathbb{R}^+$,
3. and $0 < \dot{\phi}(u)/u < +\infty$, $\forall u \in \mathbb{R}$.

If the assumptions **A1** with $\boldsymbol{A} = \boldsymbol{A}_{GY}$ or **A2** with $\boldsymbol{A} = \boldsymbol{A}_{GR}$ holds, then $Q\left(\boldsymbol{x}, \boldsymbol{x}^{(k)}\right)$ is a convex majorizing quadratic approximation that is tangent to $\mathcal{J}(\boldsymbol{x})$ at $\boldsymbol{x}^{(k)}$ [Allain 2006] where

$$\begin{cases} Q\left(\boldsymbol{x}, \boldsymbol{x}^{(k)}\right) \geq \mathcal{J}(\boldsymbol{x}). \\ Q\left(\boldsymbol{x}^{(k)}, \boldsymbol{x}^{(k)}\right) = \mathcal{J}\left(\boldsymbol{x}^{(k)}\right). \end{cases} \tag{2.39}$$

The quadratic MM algorithms provide a new interpretation of the HQ approaches, allowing the minimization of Eq. (2.29) based on the following iterative scheme [Allain 2006, Chouzenoux 2011](*see Fig. 2.4*)

$$\boldsymbol{x}^{(k+1)} = \boldsymbol{x}^{(k)} + \theta\left(\boldsymbol{x}_q^{(k+1)} - \boldsymbol{x}^{(k)}\right) \tag{2.40}$$

where

$$\begin{aligned} \boldsymbol{x}_q^{(k+1)} &= \arg\min_{\boldsymbol{x}} Q\left(\boldsymbol{x}, \boldsymbol{x}^{(k)}\right) \\ &= -\boldsymbol{A}(\boldsymbol{x}^k)^{-1}\nabla \boldsymbol{J}(\boldsymbol{x}) \end{aligned} \tag{2.41}$$

Equation (2.41) yields to a closed form expression of $\boldsymbol{x}_q^{(k+1)}$. However, the algorithm requires for each iteration k an inversion of the matrix $\boldsymbol{A} \in \mathbb{R}^{N \times N}$ which is computationally burden specially for a large N.

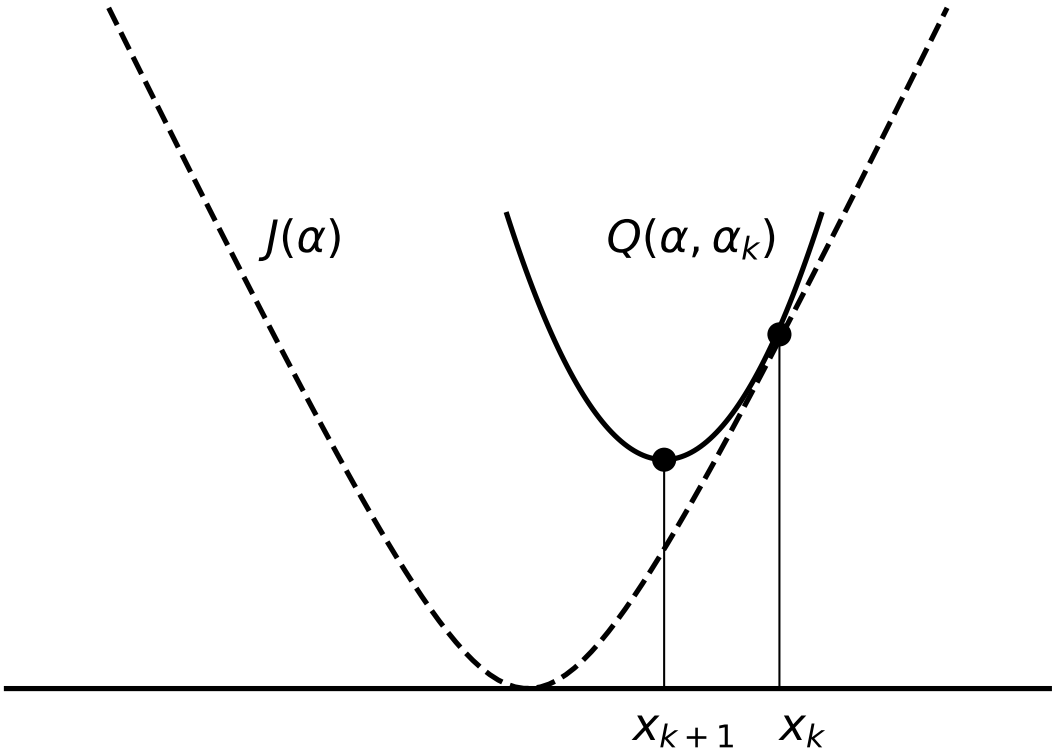

Figure 2.4: Approximation of a convex non-quadratic function $J(\alpha)$, with a quadratic convex majorizing function $Q(\alpha, \alpha^{(k)})$, tangent to $J(\alpha)$ at $\alpha^{(k)}$.

2.1.4.1 Majorize Minimize line search

Recently, the quadratic MM algorithms have been used in the line search procedure to determine the $\alpha^{(k)}$ in Eq. (2.30) on page 35. It amounts at solving the minimization of a non quadratic function in the non-linear conjugate gradient space where the descent direction $\boldsymbol{d}^{(k)}$ is provided in Eq. (2.36) on page 37 and a conjugacy term β can take one of the following forms [Labat 2008]

$$\beta_{HS}^{(k)} = \frac{\boldsymbol{J}^{t(k)}\left(\boldsymbol{J}^{(k)} - \boldsymbol{J}^{(k-1)}\right)}{\boldsymbol{d}^{t(k-1)}\left(\boldsymbol{J}^{(k)} - \boldsymbol{J}^{(k-1)}\right)} \quad \text{Hestenes-Stiefel [Hestenes 1952]}$$

$$\beta_{PRP}^{(k)} = \frac{\boldsymbol{J}^{t(k)}\left(\boldsymbol{J}^{(k)} - \boldsymbol{J}^{(k-1)}\right)}{\|\boldsymbol{J}^{(k-1)}\|^2} \quad \text{Polak-Ribière-Polyak [Polak 1969]}$$

$$\beta_{LS}^{(k)} = \frac{-\boldsymbol{J}^{t(k)}\left(\boldsymbol{J}^{(k)} - \boldsymbol{J}^{(k-1)}\right)}{\boldsymbol{d}^{t(k-1)}\boldsymbol{J}^{(k-1)}} \quad \text{Liu-Storey [Liu 1991]}$$

The quadratic function $\boldsymbol{Q}\left(\boldsymbol{x}, \boldsymbol{x}^{(k)}\right)$ in Eq. (2.38) allows to define a quadratic scalar function $q\left(\alpha, \alpha^{(k)(n)}\right)$ with $n = [1, \ldots, N]$ majorizing the scalar function $j(\alpha)$ defined in Eq. (2.32) on page 36 at the step size $\alpha^{(k)(n)}$ writing [Labat 2008]

$$q\left(\alpha, \alpha^{(k)(n)}\right) = j\left(\alpha^{(k)(n)}\right) + \left(\alpha - \alpha^{(k)(n)}\right) j'\left(\alpha^{(k)(n)}\right) + \frac{1}{2} a^{(k)(n)} \left(\alpha - \alpha^{(k)(n)}\right)^2 \quad (2.42)$$

where the scalar $a^{(k)(n)}$ writes

$$a^{(k)(n)} = \boldsymbol{d}^{t(k)} \boldsymbol{A}^{(k)(n)} \boldsymbol{d}^{(k)} \quad (2.43)$$

and with $\boldsymbol{A}^{(k)(n)} = \boldsymbol{A}\left(\boldsymbol{x}^{(k)} + \alpha^{(k)(n)} \boldsymbol{d}^{(k)}\right)$. The line search procedure to estimate $\alpha^{(k)}$ consists of performing $N \geq 1$ successive minimization of the scalar function q, resulting a sequence $[\alpha^{(k)(0)}, \ldots, \alpha^{(k)(N)}]$ that converges towards a global minimum of q if Q is convex. Given the relaxed MM recurrence in Eq. (2.40) the produced step-size values writes

$$\begin{cases} \alpha^{(k)(0)} = 0 \\ \alpha_q^{(k)(n+1)} = \arg\min_\alpha q\left(\alpha, \alpha^{(k)(n)}\right) \quad n \in \{0 \ldots N-1\} \\ \alpha^{(k)(n+1)} = \alpha^{(k)(n)} + \theta\left(\alpha_q^{(k)(n+1)} - \alpha^{(k)(n)}\right) \end{cases} \quad (2.44)$$

with θ the relaxation parameter $\in \{0, 2\}$ [Labat 2008]

2.1.4.2 Majorize Minimize multi-dimensional line search

[Chouzenoux 2011] proposed an accelerated optimization problem using subspace optimization methods with a dimension larger than one. The iterative optimization algorithm thus rewrites

$$\boldsymbol{x}^{(k+1)} = \boldsymbol{x}^{(k)} + \boldsymbol{\alpha}^{(k)} \boldsymbol{D}^{(k)} \quad (2.45)$$

where $\boldsymbol{D}^{(k)}$ is the $Z-$dimensional subspace. Several subspace algorithms have been provided in [Chouzenoux 2011], particularly the memory gradient algorithms and the Newton type subspace algorithms. In addition, $\boldsymbol{\alpha}^{(k)}$ is a step-size vector of size Z where $\boldsymbol{\alpha}^{(k)} = \left[\alpha_1^{(k)}, \ldots, \alpha_Z^{(k)}\right]$.

Following the same analogy as in Eq. (2.44) the Majorize-Minimize multi-dimensional search produces a step size vector writing

$$\boldsymbol{\alpha}^{(k)(n+1)} = \boldsymbol{\alpha}^{(k)(n)} - \theta\left(\left(\boldsymbol{U}^{(k)(n)}\right)^{-1}\nabla j\left(\boldsymbol{\alpha}^{(k)(n)}\right)\right). \tag{2.46}$$

where $\boldsymbol{U}^{(k)(n)} = \boldsymbol{D}^{t(k)}\boldsymbol{A}^{(k)(n)}\boldsymbol{D}^{(k)}$ is a $Z \times Z$ symmetric positive definite (SPD) matrix and $\boldsymbol{A}^{(k)(n)} = \boldsymbol{A}\left(\boldsymbol{x}^{(k)} + \boldsymbol{D}^{(k)}\boldsymbol{\alpha}^{(k)(n)}\right)$.

[Chouzenoux 2011] showed that choosing a multi-dimensional subspace over the non-linear Conjugate Gradient leads to a faster convergence minimization algorithm. However, the complexity of the problem increases since it requires a multi-dimensional step-size strategy to determine the vector $\boldsymbol{\alpha}^{(k)}$. The authors finally concluded that for a subspace dimension $Z = 2$ and for $N = 1$ iteration shows the best trade-off between the number of iteration k before convergence and the cost per iteration.

2.2 Inverse problem for Hyperspectral reconstruction

We presented in the previous section a general overview of the inverse problem approaches. In particular, we provided reconstruction methods and algorithms based on the minimization of a regularized objective function with various types of regularization terms. This section presents several works and techniques related to the reconstruction of a 2D+λ image using the inverse problem approaches. In particular, we focus on the reconstruction of 2D+λ images with a high spatial and spectral resolution such as the Hyperspectral (HS) images, which is the main objective of this thesis.

We start this section with a brief introduction to the HS images and their different acquisition techniques, then we present works related to the HS reconstruction for different applications.

2.2.1 Hyperspectral technology

Hyperspectral imaging (HSI) is a combination of imaging and spectroscopy that provides high-resolution spectra for every spatial location of an observed field of view (FOV). HSI products are 3-dimensional images holding two spatial dimensions (i, j) and a series of narrow spectral bands forming the third dimension l. HSI was initially implemented on airborne platforms for earth observations but recently has been applied in numerous applications, including food quality control, medical diagnosis, archeology, astrophysics, etc. [Khan 2018].

For astrophysical observations, HS instruments are usually placed at the focal plane of ground-based or space-based telescopes in order to acquire, if possible, spatially resolved spectra of objects. Among these instruments, to name a few, are the Infrared Slit Spectrograph onboard the Spitzer space telescope [Houck 2004], the Space Telescope Imaging Spectrograph on board the Hubble telescope [Woodgate 1998], and lately, the Mid Resolution Spectrometer of the Mid Infrared Instrument onboard the James Webb Space Telescope [Wells 2015]. The measured spectra for these instruments, which are working mainly in the infrared range, allow the remote analysis of the surface and atmospheric composition of planets, the chemical composition of extraterrestrial material, or the evolution of galaxies.

Direct observation of a HS image is not possible because the detectors are 1-dimensional or 2-dimensional, but not 3-dimensional. Therefore, HS acquisition techniques allowing to acquire 2D+λ images must be used. These techniques include point scanning, line scanning, and integral field spectroscopy.

A. Point scanning: The very first used technique is called the point scanning (whiskbroom)[Geladi 2007], and consists of scanning one spatial location at a time. The light of the scanned position is diffracted using a dispersion instrument (prism, diffraction gratings) and projected onto a linear sensor. By pointing the acquisition instrument at successive positions in the two spatial dimensions, a 3D data cube can

be built. This technique is not suitable to build hyperspectral images which cover large FOV because successive pointing at each spatial position takes too long.

B. Line scanning: The line scanning technique (push broom) [Geladi 2007, Arablouei 2016] consists on scanning a complete spatial line (or slit) along one spatial axis. The light is dispersed on a 2D sensor holding one spatial dimension along the slit and one spectral dimension. Then the pointing of the acquisition instrument is progressively moved along the other spatial dimension (perpendicular to the slit) to acquire a 3D hyperspectral image. Even though data acquisition using the line scanning technique is faster than that of the point scanning technique, it still requires multiple exposures, which takes time. The difference between the point scanning and the line scanning techniques is illustrated in Fig. 2.5.

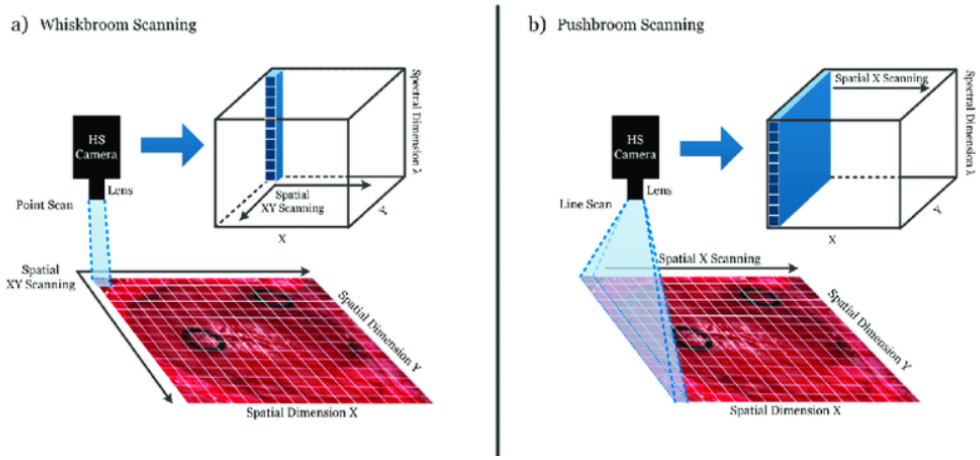

Figure 2.5: Principle of the Whiskbroom and Pushbroom techniques, edited from [Halicek 2019]

C. Integral Field Spectroscopy: Unlike the Point scanning and Line scanning methods, the integral field spectroscopy (IFS) [Vives 2008b] does not require any scanning process. This technique consists of observing a FOV through several slits in parallel via optical instruments such as a fiber array or an image slicer. The light within each slit is diffracted and projected onto 2D detectors. Each pixel on the detector corresponds to one spatial position and one wavelength. A hyperspectral image can be build by assembling 2D measurements along the other spatial dimension. Fig. 2.6 illustrates in detail the concept of the hyperspectral acquisition with an Integral field spectrometer.

In this work, we consider the integral field spectrometer that takes as input a 2D+λ image with a high spatial and spectral resolution, and produces a set of 2D spectral measurements. However, a simple assembly of these measurements along a third dimension, as suggested above, is not directly applicable since the measurements are degraded by spatial and spectral optical responses (Point Spread Functions: PSF), and also corrupted by noise. Another reconstruction approach must

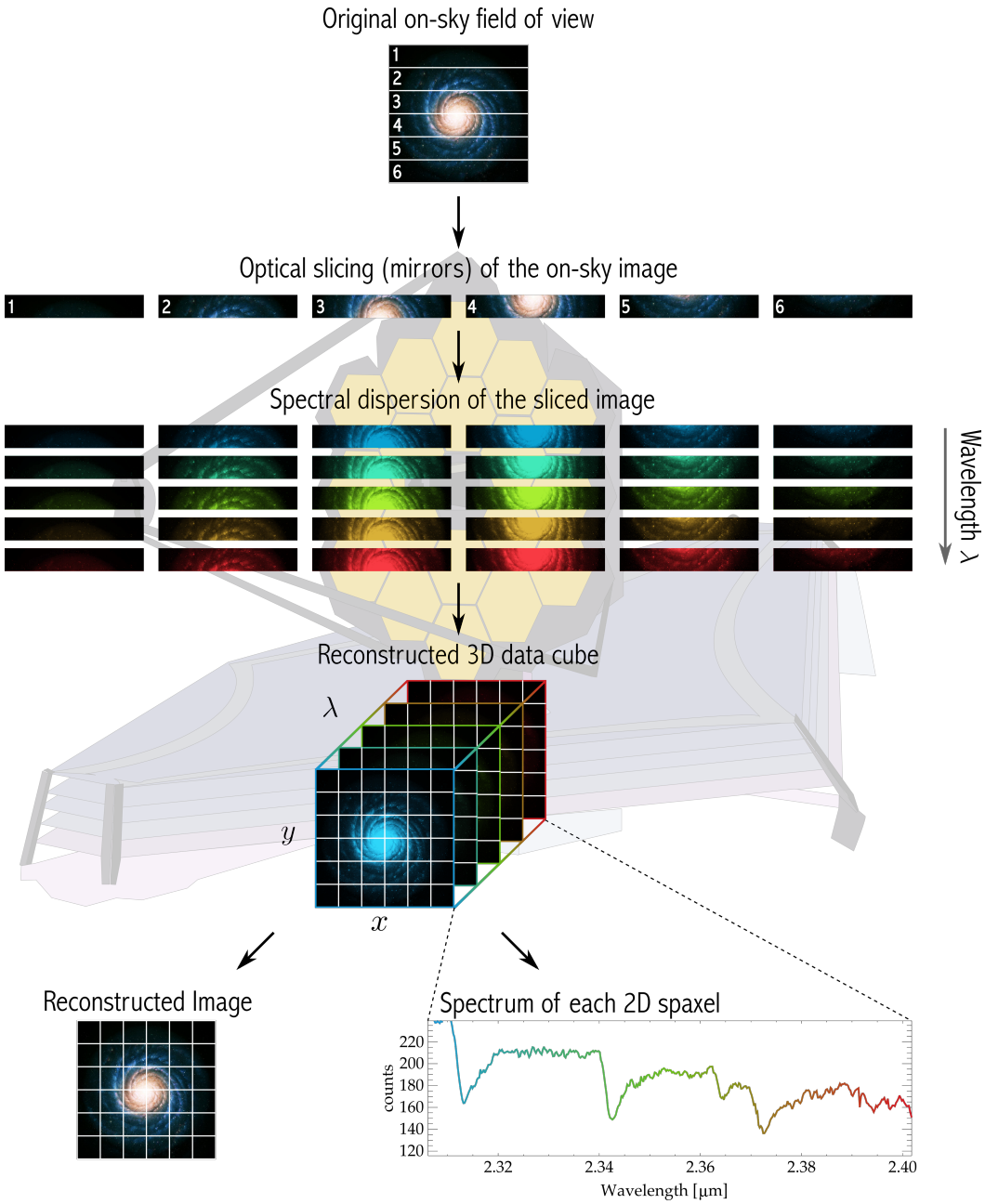

Figure 2.6: Principle of an integral field spectrometer, taken from https://jwst-docs.stsci.edu/methods-and-roadmaps/jwst-integral-field-spectroscopy

be considered, in particular, inverse problem approaches based on the minimization of a regularized objective function.

2.2.2 Spatio-spectral reconstruction

A 2D+λ image (*i.e.* RGB, Multispectral, Hyperspectral) is a series of 2D spatial images stacked along the spectral dimension. We represent such images as $\boldsymbol{x}[i,j,l] \in \mathbb{R}^{IJL}$ with (i,j) denoting the spatial position and l the spectral band. Several works found in the literature tackle the reconstruction of $\boldsymbol{x}[i,j,l]$ from degraded measurements $\boldsymbol{y}[i',j',l'] \in \mathbb{R}^{I'J'L'}$ using inverse problem approaches. The proposed reconstruction algorithms heavily depends on the forward model $\boldsymbol{H} \in \mathbb{R}^{IJL \times I'J'L'}$ that relates $\boldsymbol{y}$ to the unknown $\boldsymbol{x}$.

The first 2D+λ image reconstruction treated a deconvolution problem and considered that the forward model $\boldsymbol{H}$ is a spectral invariant convolution matrix. Consequently, no cross-correlation exists between the spectral bands of $\boldsymbol{y}$, and the reconstruction can be performed separately for each monochromatic image at a fixed spectral band l [Hunt 1984, Galatsanos 1989]. However, treating separately the spatial and spectral dimensions is too limiting in most applications and cannot be used when the spectral correlation exists ($\boldsymbol{H}^{i,j,l_1 \times i,j,l_2} \neq 0$). A typical example of an existing correlation between spectral bands is when $\boldsymbol{H}$ is a wavelength-dependent convolution matrix. [Galatsanos 1991] addressed the reconstruction of an RGB image while considering the spectral correlation between spectral bands. The proposed reconstruction algorithm is based on a spatially adaptive regularized least square approach that handles soft and sharp variations within a local spatial image. In addition, the algorithm includes three regularizing operators to ensure a smooth transition between spectral bands.

Other works proposed reconstruction algorithms for high-dimensional 2D+λ images with a large number of spectral bands, such as the hyperspectral (HS) images. For instance, [Henrot 2011] solved a deconvolution problem to reconstruct a HS image $\boldsymbol{x}$ by jointly processing the spatial and spectral information of $\boldsymbol{y}$. The proposed reconstruction relies on minimizing an objective function $\mathcal{J}$ that includes a data fidelity term and quadratic spatial and spectral regularization and a positivity constraint, yielding to a closed-form expression of the optimizer $\hat{\boldsymbol{x}}$. The authors solved the problem in the Fourier domain to allow fast computations. An extension of [Henrot 2011] was proposed in [Henrot 2013] by considering a convex half quadratic spatial regularization for edge-preserving. The optimizer $\hat{\boldsymbol{x}}$ is obtained by combining the fast algorithm presented in [Henrot 2011] with the iterative half-quadratic algorithm using Geman and Yang (GY) formulation [Geman 1995] and detailed in section 2.1.2.3.

Other works used inverse problems for the reconstruction of astronomical HS images. For instance, [Bongard 2011] developed a forward model $\boldsymbol{H}$ based on an integral field spectrometer instrument to acquire astronomical measurements $\boldsymbol{y}[i',j',l']$. This model considers a spectrally invariant spatial PSF. They proposed a recon-

struction method based on Tikhonov regularization with spectrally variable hyper-parameters to prevent over regularizing large features or under regularizing small features.

However, all the mentioned works considered that the forward model $\boldsymbol{H}$ is a spectrally invariant convolution matrix, meaning that there is no cross-correlation between the spectral channels.

The work proposed in [Bongard 2011] was later extended in [Soulez 2013] where $\boldsymbol{H}$ accounts for a wavelength dependant spatial PSF, approximated with a linear interpolation of weighted monochromatic PSFs. The authors provided a comparison between Tikhonov and spatial sparsity algorithms to reconstruct HS images for the Multi-Unit Spectroscopic Explorer (MUSE)[1]. However, the proposed forward model $\boldsymbol{H}$ for the IFS instrument is unsuitable for our application since it does not consider a wavelength dependant spectral blurring coming from the response of the wavelength dispersing system. In addition, the resulted measurements $\boldsymbol{y}[i', j', l']$ in [Bongard 2011] and [Soulez 2013] are 3D, sampled with uniform spatial and spectral sampling steps that match the sampling steps of the input image $\boldsymbol{x}$. Hence, the proposed reconstruction algorithms cannot be applied for the measurements provided by MRS of JWST/MIRI.

[Rodet 2008] proposed a forward model $\boldsymbol{H}$ for the infrared slit spectrograph on board the Spitzer Space Telescope. The model takes into account a wavelength dependant spatial and spectral blurring and results a set of 2D measurements $\boldsymbol{y}_{j'}[i', l']$ from successive slit spectroscopy scans. Moreover, the uniform spatial and spectral sampling of the measurements are larger than that of the input image $\boldsymbol{x}$. The proposed reconstruction is based on minimizing a regularized least square function with a spatial and spectral quadratic regularization. The input image and the response of the measuring instrument, originally modeled with continuous variables, are decomposed over a family of Gaussian approximations to allow fast computations. However, the spatial and spectral distribution of the measurements are uniformly sampled.

In our work, we proposed a discrete forward model $\boldsymbol{H}$ for the IFS instrument of JWST/MIRI that considers a wavelength-dependent spatial and spectral blurring and results in a set of 2D measurements denoted $\boldsymbol{y}_{j'}[i', l']$, projected onto different 2D detectors with heterogeneous spatial and spectral sampling steps. We then use the proposed $\boldsymbol{H}$ to solve an unconstrained minimization of a regularized objective function with spatial and spectral convex regularization for edge-preserving (detailed in Chapter 4). Our reconstruction algorithm mainly include a spatio-spectral deconvolution step and a super-resolution (SR) step to enhance the spatial resolution of the reconstructed $\hat{\boldsymbol{x}}$ (see section 2.2.4)

[1] https://www.eso.org/sci/facilities/develop/instruments/muse.html

2.2.3 Linear mixing model

The 2D+λ image $\boldsymbol{x}$ with a high spectral resolution, such as Hyperspectral images, can be formulated as a Linear Mixing Model (LMM) with

$$\boldsymbol{x}[i,j,l] = \sum_{m=1}^{M} \boldsymbol{a}_m[i,j] \times \mathbf{s}_m[l] \tag{2.47}$$

where the spectral distribution at all the spatial locations of $\boldsymbol{x}$ is represented as a linear combination of M spectral components $\mathbf{s}_m[l]$, each weighted by mixing coefficients $\boldsymbol{a}_m[i,j]$ with $m = [1,\dots,M]$ [Keshava 2002]. The reconstruction of $\boldsymbol{x}[i,j,l]$ from degraded measurements $\boldsymbol{y}[i',j',l']$ with the LMM formulation corresponds to the estimation of the spectral components $\mathbf{s}$ and the mixing coefficients $\boldsymbol{a}$, known as spectral unmixing.

The LMM formulation is excessively treated for the reconstruction of HS images. For instance, the reconstruction of $\boldsymbol{x}$ using the inverse problem approaches can be computationally a burden because of the large number of spectral bands. However, the spectral distribution between the spatial pixels is often highly correlated at all wavelengths. Consequently, the pixels of $\boldsymbol{x}$ can be assumed to live in a low dimensional linear subspace where $M \ll L$ (L the number of the spectral bands) leading to a reduction of the unknown variables to estimate [P Nascimento 2007, Bioucas-Dias 2012]. The dimension reduction technique can be achieved using several source separation algorithms that explore a low-rank approximation of the HS images. Such algorithms include the Non-Negative Matrix Factorization (NMF) [Lee 1999], the Independent Component Analysis (ICA) [Hyvarinen 1999], the Principal Component Analysis (PCA), [Jolliffe 2016], etc.

Several works assume that the spectral components are known *a priori* from source separation algorithms [Hadj-Youcef 2020] or learned from existing spectral libraries [Zhao 2013]. Thus, the reconstruction problem relies on the estimation of the mixing coefficients $\boldsymbol{a}$ that can be achieved using the regularized least square approaches writing

$$\hat{\boldsymbol{a}} = \arg\min_{\boldsymbol{a}} \Big\{ \|\boldsymbol{y} - \boldsymbol{H}\boldsymbol{x}\|^2 + \mu\mathcal{R}(\boldsymbol{a}) \Big\}. \tag{2.48}$$

For instance, [Song 2019] proposed a joint unmixing-deconvolution algorithm based on the Tikhonov least square approach with a non-negative constraint to estimate $\boldsymbol{a}$ from shift-invariant blurred measurements. [Hadj-Youcef 2020] considered a low-rank approximation for the input $\boldsymbol{x}$ and estimated the mixing coefficients $\boldsymbol{a}$ from low spectral resolution measurements $\boldsymbol{y}$, blurred with a wavelength dependant spatial PSF. The problem in Eq. (2.48) is solved in the Fourier domain for fast computations while enforcing a convex regularization for edge-preserving. [Zhao 2013] assumed that the spectral components $\mathbf{s}$ have been extracted from a spectral library and estimated the mixing coefficients $\boldsymbol{a}$ using the Total variation and sparsity regularization terms to handle the spectral dependant spatial blur. [Chouzenoux 2014] used primal-dual interior-point optimization to solve constrained least square ap-

proaches and estimate mixing coefficient estimations. The algorithm is suitable for parallel GPU implementations, allowing a reduction in computational costs.

Other works are interested in the physical meaning of the spectral components $\mathbf{s}$ to identify materials within the observed Field Of View (FOV). For instance, in earth observations, the spectral components are pure spectra called endmembers, and the mixing coefficients are called abundance. Different endmember extraction algorithms are addressed in the literature, depending on the mixture level of the endmembers within a pixel. Among these categories, we mention the geometrical and statistical approaches [Bioucas-Dias 2012, Keshava 2002]. Algorithms based on geometrical approaches benefit from the existence of a pure pixel per endmember. When this assumption is missing, minimum volume algorithms can be used to fit the measurements in the "minimum volume simplex". On the other hand, algorithms based on statistical approaches are employed when the spectral components are highly mixed within a pixel [Henrot 2014a]. In addition, to preserve the physical meaning of the endmembers, several constraints are usually imposed during the estimation of $\boldsymbol{a}$, in particular, the non-negativity constraint (ANC) and the sum-to-one constraint (ASC). For instance, [Henrot 2014a] considered the unsupervised deblurring-unmixing problem and showed that for the geometrical endmembers extraction algorithms, it is better to perform deconvolution step before unmixing and not the opposite. [Berné 2007] identified the spectral signatures of small interstellar dust particles from measurements acquired by infrared spectrograph onboard spitzer. The authors provided a comparison between two spectral unmixing algorithms; the non-negative matrix factorization (NMF) algorithm [Lee 1999] and fast, independent component analysis (ICA) algorithm [Hyvarinen 1999]. [Dobigeon 2009] proposed a Bayesian method and a Markov chain Monte Carlo (MCMC) algorithm to jointly estimate $\mathbf{s}$ and $\boldsymbol{a}$ while considering the sum-to-one and the non-negativity constraint.

In this thesis, we assume that the 2D+λ input image $\boldsymbol{x}$ lives in a low dimensional subspace and can be expressed as a linear combination of M spectral components $\mathbf{s}$, assumed known, weighted by unknown mixing coefficients $\boldsymbol{a}$. We are only interested in the subspace approximation and not in exploring the physical meaning of $\mathbf{s}$. Consequently, the reconstruction of $\boldsymbol{x}$ relies on the estimation of $\boldsymbol{a}$, based on the minimization of an unconstrained regularized objective function with a convex regularization for edge-preserving.

2.2.4 Spatial Resolution Enhancement

In most applications, the spatial resolution of the measurements is limited because of the sub-sampling at the focal plane of the detector. Thus, obtaining high spatial resolution images remains a challenge due to the limited size and number of the detectors' pixels. Since reducing the pixel size is expensive (if not impossible) and reduces the amount of the captured light, post-processing techniques are necessary to enhance the spatial resolution of hyperspectral measurements

$\boldsymbol{y}$ [Sung Cheol Park 2003].

In the discrete case, the pixel size of the observed 2D+λ input image $\boldsymbol{x}[i,j,l]$ is usually smaller than that of the detectors. Therefore, we consider in this section that the input $\boldsymbol{x}[i,j,l]$ is represented on a high-resolution (HR) grid while the output are 3D hyperspectral measurements $\boldsymbol{y}[i',j',l']$ represented on a low-resolution (LR) one.

Interpolation methods (*e.g., linear, cubic, etc.*) can be used for increasing the size of the LR $\boldsymbol{y}$ to match that of $\boldsymbol{x}$. However, these methods do not compensate for the loss of information since it does not improve spatial resolution.
Alternative methods must be considered, such as the multi-frame Super-Resolution [Sung Cheol Park 2003, Akgun 2005, Zhang 2012] and the data fusion with an auxiliary image [Guilloteau 2020, Wei 2016] to compensate the loss of information and enhance the spatial resolution of the reconstructed object $\hat{\boldsymbol{x}}$.

2.2.4.1 Multi-frame Super resolution

This technique reconstructs HR object $\hat{\boldsymbol{x}}[i,j,l]$ from several number P of shifted and aliased LR measurements $\boldsymbol{y}_p[i',j',l']$ with $p=[1,\ldots,P]$. Each of the LR measurements provides new information lost due to the sub-sampling and contributes to the resolution enhancement. This new information is only useful if the LR measurements are shifted with subpixel steps. [Sung Cheol Park 2003] provides a detailed overview of the multi-frame super-resolution (SR) algorithms that were first applied to monochromatic images. For instance, the shift-and-add algorithm is commonly used for SR reconstruction [Fruchter 2002, Farsiu 2003], consisting of aligning all the observed measurements before co-adding the results to provide a single HR reconstructed object $\hat{\boldsymbol{x}}[i,j,l]$ with an enhanced spatial resolution. A deconvolution step often follows this technique to remove the blurring effects. The shift-and-add can be extended to deal with a 3D spatio-spectral reconstruction. However, the downfall of this method is that the deconvolution step is treated separately for each spectral band and does not consider the cross-correlation between the bands. [Buttingsrud 2006] proposed a multi-frame super-resolution algorithm for HSI based on the maximum entropy method. Other works consider that the spectral bands at each object's pixel live in a low dimensional subspace. This dimensional reduction is beneficial because it reduces the number of unknowns and allows fast computations, as discussed in section 2.2.3. Moreover, these works assumed that the spectral components are known and proposed methods to estimate the mixing coefficients. For instance, [Zhang 2012] addressed the multi-frame HS image reconstruction from shift invariant spatial blurred and spatially sub-sampled measurements $\boldsymbol{y}[i',j',l]$ in the principle components analysis (PCA) transform domain. The authors divided the principal components into three categories, where they used the first few components to estimate the motion and to reconstruct the input object using the maximum a posteriori (MAP) algorithm. [Akgun 2005] proposed a complex forward model that depends on the known spectral components to produce blurred, sampled and aliased measurements. The SR multi-frame recon-

struction algorithm is based on the projection onto convex sets (POCS) [Stark 1989] to estimate the mixing coefficients $\boldsymbol{a}$. However, the work proposed in [Akgun 2005] is unsuitable for our application because the forwards model does not account for a wavelength-dependant spatial and spectral blurring. In addition the spatial sampling of the measurements are uniform across the measured spectral bands.

2.2.4.2 Fusion with auxiliary Images

The multi-frame SR reconstruction often requires many observations to compensate for the spatial information lost at the focal plane of the detector, leading to high computational costs. In addition, the measuring instrument may not enable multiple observations of the same input in real-life applications. Therefore, another spatial enhancement technique can be considered as an alternative, consisting of fusing low spatial resolution (LR) HS measurements with a high spatial resolution (HR) auxiliary images observing the same input scene, such as Panchromatic (PAN) or Multi-spectral (MS) [Yokoya 2017]. The most widespread fusion technique is the pan-sharpening that fuses HS measurements with HR panchromatic images (monochromatic image with high spatial resolution). This method consists of extracting the spatial structure information from the PAN image and inject it into an interpolated version of the LR measurements [Vivone 2014]. Pan-sharpening provides a fast fusion technique with an accurate spatial enhancement but does not consider the spectral correlation between the spectral bands.

Other works considered the fusion between LR HS measurements with an HR MS measurements (HS-MS fusion), both measuring the same spectral range but with different spectral resolutions [2]. For instance [Yokoya 2012] proposed a coupled non-negative matrix factorization (CNMF) that performs an alternate spectral unmixing for HS and MS measurements using the NMF technique [Lee 1999]. The 2D+λ reconstructed image is obtained by extracting the HR mixing coefficients from the MS measurements and the HR spectral components from the HS measurements. However, this method does not fully exploit the spatial and spectral details provided by HS and MS, respectively.

HS-MS fusion has also been addressed in the inverse problems framework [Guilloteau 2020, Simões 2014, Wei 2015]. The fusion process is based on minimizing an objective function associated with two data fitting terms for HS and MS and a regularization term describing the *a priori* information we have on the 2D+λ input image. Most of the fusion procedures applied with the inverse problem assume that the input $\boldsymbol{x}$ lives in a low-dimensional subspace. In addition, these works usually assume that the instrument response spatially blurs the HS and MS measurements. For instance, [Simões 2014] used a TV regularization for blind MS-HS fusion, in which the spatial and spectral responses are estimated from the observed measurements. [Wei 2015] promoted sparse regularization by representing the input object as a combination

[2] The spectral resolution of the HS measurements is higher than that of the MS measurements

of dictionary atoms learned from the observed measurements.
However, these works assumed that the spatial blur is a spectrally-invariant. [Guilloteau 2020] considered a wavelength-dependent spatial blurring and proposed a regularized least square algorithm with a quadratic regularization. The problem was computed in the frequency domain to handle the high dimensionality of astrophysical measurements.

The related works presented in this section considered 3D measurements $\boldsymbol{y}[i', j', l']$ where a spectral distribution is associated with a 2D spatial position. These measurements are, in most cases, spatially blurred and spatially sampled with a regular sampling step across the spectral bands.
In this thesis, we are interested in the reconstruction of a 2D+λ input image $\boldsymbol{x}[i, j, l]$ from a set j' of astronomical 2D measurements $\boldsymbol{y}'_j[i', l']$ that are degraded with a wavelength-dependant spatio-spectral blurring and sampled onto different detectors with heterogeneous spatial and spectral sampling steps. Since the spatial sampling is insufficient at all wavelengths, we consider the dithering method to compensate the loss of spatial information. This technique consists of observing different FOV of the same scene by slightly shifting the pointing of the measuring instrument, yielding to a multi-frame super-resolution problem (see section 2.2.4.1).

Chapter 3

Mid-Infrared Resolution characteristics

Contents

3.1 Introduction

In the previous chapter, we discussed several works handling the reconstruction of hyperspectral (HS) images with inverse problem approaches. These reconstruction techniques rely on an observation matrix $\boldsymbol{H}$ or a forward model that mathematically describes the response of the measuring system and establishes a relationship between an HS input image $\boldsymbol{x}$ and the simulated measurements $\boldsymbol{y}$. Our work falls within this framework, where we seek to reconstruct an HS image from a set of measurements with a high spectral resolution provided by an Integral Field Spectrometer instrument, in particular, the Mid-Resolution Spectroscopy (MRS)

of the Mid-Infrared Instrument (MIRI) on board the James Webb Space Telescope (JWST) [Wells 2015]. The MRS instrument involves a series of complex components with a wavelength dependent spatial and spectral blurring and spatial sub-sampling.

In this chapter, we detail the MRS instrument by addressing the related optical behaviour and issues and by identifying the response of its components. We also provide characteristics specific to this instrument such as the wavelength coverage, the observed Field of Views, and the spectral resolving power. The work provided in this chapter is crucial for developing an explicit forward model used in the reconstruction process that accounts for the MRS limitations.

In the following, we first give a general presentation of the JWST and provide details about its optical system. We then describe the MRS instrument which mainly relies on several integral field spectrometers (IFS), each measuring a fraction of the spectral range of the instrument.

3.2 James Webb Space Telescope

The James Webb Space Telescope (JWST) [Mather 2004, Gardner 2009](*see fig. 3.1*), which is scheduled to be launched in October 2021, is the next space observatory succeeding the Hubble Space Telescope (HST) [Lallo 2012]. It is expected to make breakthrough discoveries in astrophysics and to resolve several important questions concerning the formation of stars and planets, the first light of the universe, or the birth of galaxies. The JWST project is an international collaboration between the National Aeronautics and Space Administration (NASA), the European Space Agency (ESA), and the Canadian Space Agency(CSA).
While the HST contains a monolithic primary mirror of 2.4 m in diameter, the JWST will include the biggest primary mirror ever launched to space, measuring 6.5 m in diameter. This mirror will allow unprecedented sensitivity, due to the large number of collected photons, and angular resolution. Moreover, the JWST will measure a broad spectral range, between 0.6 and 28.3 μm, extending into the mid-infrared. It will allow the observation of faint or distant objects that HST failed to observe. The JWST includes a set of four scientific instruments mounted on the focal plane of the telescope. These instruments will observe specific spectral ranges with varying FOV (*see fig. 3.2*). They offer a unique combination of observation modes, such as coronagraphy, imaging, and spectroscopy. These instruments are:

- NIRSpec: Near-Infrared Spectrograph ($0.6 - 5\,\mu$m),
- NIRCam: Near-Infrared Camera ($0.6 - 5\,\mu$m),
- NIRISS: Near-Infrared Imager and Slitless Spectrograph ($0.6 - 5\,\mu$m),
- MIRI: Mid-Infrared Instrument ($4.9 - 28.3\,\mu$m).

The Mid-Infrared Instrument (MIRI) offers a unique combination of imaging and spectroscopy facilities through its imager (MIRIM) [Bouchet 2015] and its mid-

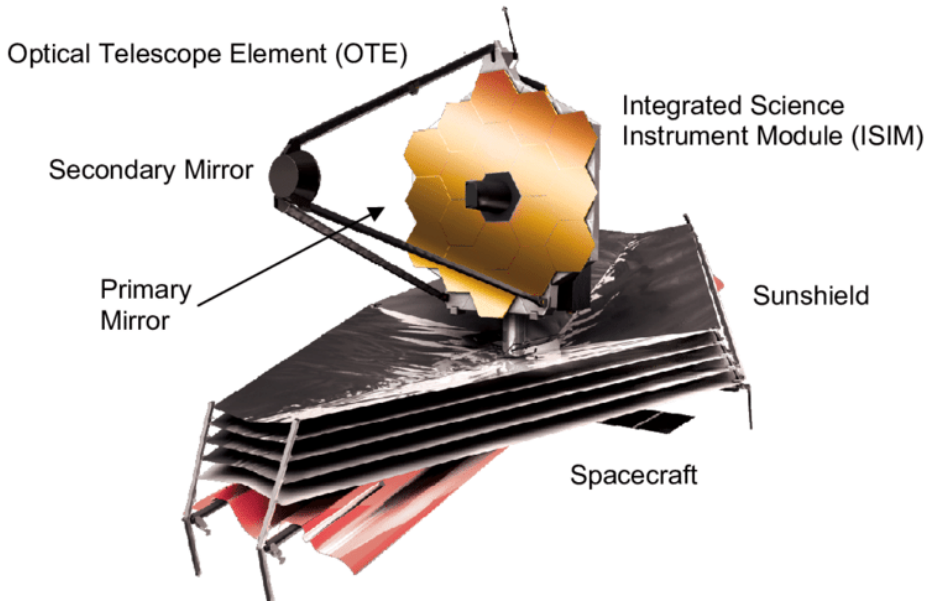

Figure 3.1: The James Webb Space Telescope [Mather 2004]

resolution spectroscopy (MRS) [Wells 2015], respectively. Both instruments observes the same infrared range (between 4.9 and 28.3 μm) but with different spectral resolutions and distinct spatial fields of view. MIRIM provides Multispectral (MS) measurements with a good spatial information in terms of detector sampling and observed field of view,(74×113 arcseconds^2) but with a limited spectral resolution ($\lambda/\Delta\lambda \approx 5$) because of the wavelength integration over broad spectral filters. On the other hand, the MRS observes a relatively small field of view (up to 6.9×7.9 arcseconds^2) and provides measurements with insufficient spatial sampling but with high spectral resolution ($\lambda/\Delta\lambda \approx 1500 - 3500$). In this work, we are interested in processing infrared 2D measurements provided by the integral field spectrometer (IFS) instrument (such as the MRS) to reconstruct a 2D+λ image with high resolution.

3.3 Optical System for JWST

The JWST incorporates an all-reflective optical system. It focuses the light received from the observed spatio-spectral object on the focal plane, where the scientific instruments are mounted. This optical system includes the primary mirror made by 18 hexagonal segments aligned to form one mirror of 6.5 m in diameter. Increasing the aperture of the telescope allows the collection of more photons and a better detection of faint astronomical objects. Due to the diffraction, the angular resolution of the optical system heavily depends on the diameter of the aperture function with:

$$\theta \approx \frac{\lambda}{D} \tag{3.1}$$

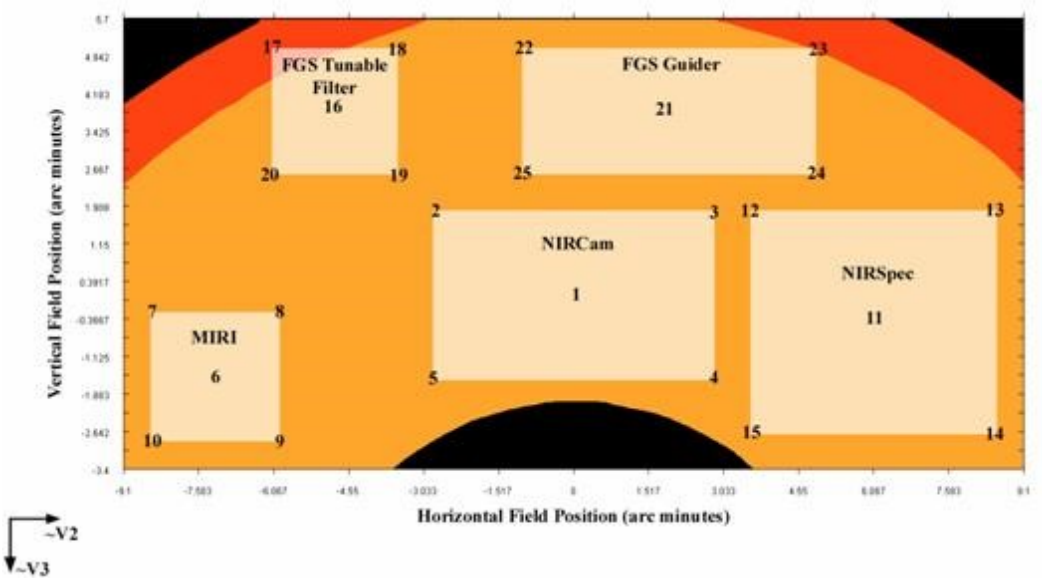

Figure 3.2: The JWST focal plane layout (https://www.cosmos.esa.int/web/jwst-nirspec/home-old)

where D is the diameter of the telescope and λ the wavelength (*see Fig. 3.3*).

Accurate knowledge of the response of the optical system, also known as the point spread function (PSF), is crucial in many applications for data analysis, such as PSF-fitting to measure the flux of point-sources, or deconvolution. The PSF strongly depends on the shape and the size of the aperture function of the primary mirror, denoted $A(x, y)$. Since in astrophysics very distant objects are observed, the PSF can be calculated using the Franhaufer approximation. In that case the intensity of the PSF is simply the square module of the Fourier transform of $A(x, y)$ [Goodman 1996]

$$PSF = \|FT\{A(x, y)\}\|^2 \tag{3.2}$$

The PSF shape depends on the complexity of the primary mirror. For instance, the Spitzer Space telescope [Houck 2004] included a monolithic primary mirror with a circular aperture function. Therefore, an accurate analytical form of the PSF, known as the Airy function [Goodman 1996], could be used. On the other hand, the mirror of the JWST is not monolithic, but composed of 18 hexagonal segments. An analytical form of the PSF can not be accurately provided with the Franhaufer approximation mainly because of the gaps between the segments [Elliott 2005]. In [Makidon 2007], different numerical tools to compute the JWST PSF are presented.

In this work, the monochromatic PSFs of the JWST are simulated with the official webbPSF tool [Perrin 2012, Perrin 2014] developed by the Space Telescope Science Institute (STScI). This simulator is not a full optical model but rather a tool that transforms optical path difference (OPD) maps into PSFs adapted for

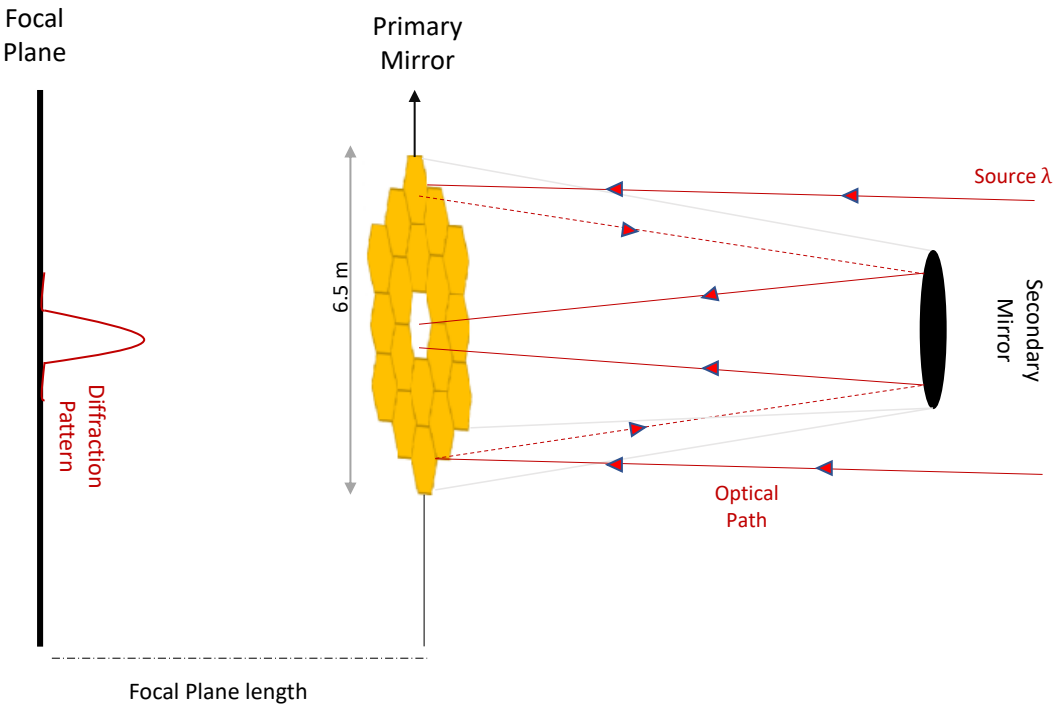

Figure 3.3: Illustration of the optical path of the observed light source.

the JWST. It computes for any JWST instrument realistic PSFs with requested properties, such as the pixel size of the detector, the PSF image size, the rotation, the spectral filters, etc.

Using the WebbPSF simulator, we have computed monochromatic PSFs as a function of the wavelengths. We illustrate in *Fig.* 3.4 six monochromatic PSFs ranging from 4.8 to 28 μm, corresponding to the spectral range observed by the MRS instrument. All PSFs are normalized to one and shown in logarithmic scales. We see that the complex shape of the PSFs due to the segmented and hexagonal shape of the primary mirror. Moreover, the PSF widens with increasing wavelengths: it is spectrally non-stationary.

3.4 MIRI Medium Resolution Spectroscopy

The Mid-Resolution Spectrometer (MRS) of the Mid-Infrared Instrument(MIRI) is an Integral Field Spectrometer (IFS) that observes a specific infrared range of the light collected by the optical system within a finite Field Of View (FOV). All details of the MRS instrument are provided in [Wells 2015]. Here, we are interested in the optical issues related to the instrument rather than its mechanical layout.

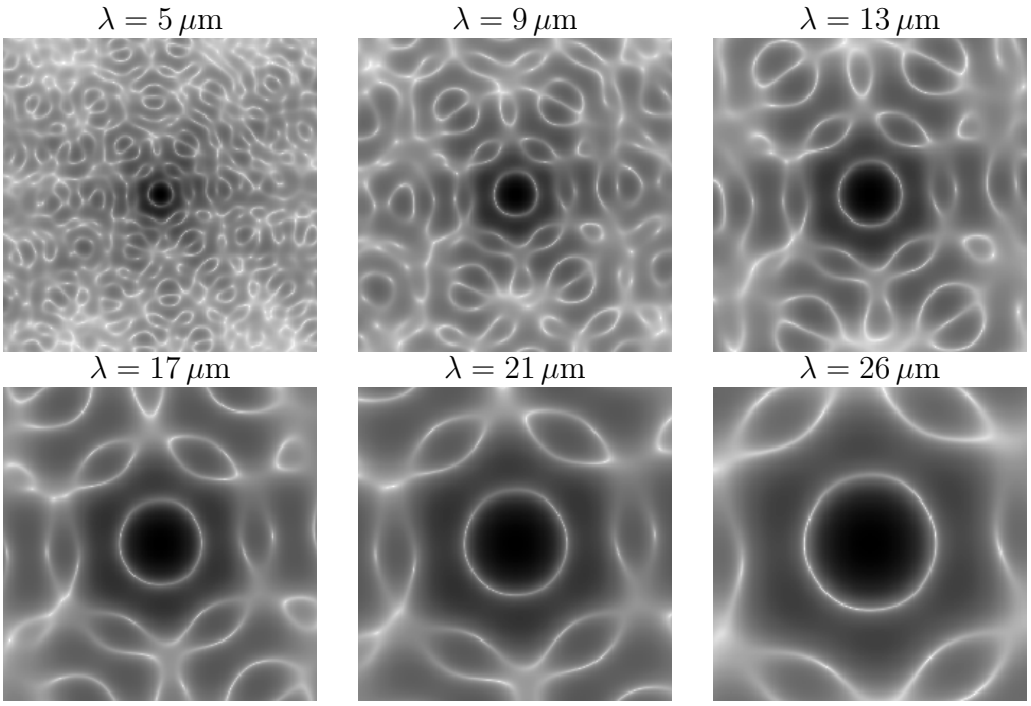

Figure 3.4: Monochromatic PSFs of the JWST at six different wavelengths computed with the WebbPSF simulator (logarithmic scales).

3.4.1 Spectral coverage

The MRS covers a wide spectral range, between 4.9 μm and 28.3 μm with a spectral resolving power [1] ranging between 1500 and 3000. Four spectral channels are required to cover the complete spectral range, each including an Integral Field Unit (IFU) and a diffraction grating for the light dispersion. These channels are observed simultaneously, with co-aligned FOV of different sizes, from 3.2×3.7 up to $6.9 \times 7.9\,\mathrm{arcsec}^2$ as reported in Table 3.1 and shown in Figure. 3.5. [2] The spectral bands of the channels were chosen such that $\lambda_{long}/\lambda_{short} = (28.3/5)^{1/4} = 1.54$, where λ_{short} and λ_{long} are the shortest and longest wavelengths of operation for each channel respectively.

The MRS uses two detectors, the first one for the two short-wavelength channels (*Channels 1-2*) and the second one for the two long-wavelength channels (*Channels 3-4*). Each detector provides a spectral coverage slightly larger than one-third the full spectral range of each channel. Therefore, three successive exposures within three spectral *sub-bands* are required to provide full spectral coverage. Note that there is a spectral overlap of typically $10-15\%$ between adjacent sub-bands (see also

[1] The spectral resolving power R is equal to $\lambda\,/\,\Delta\lambda$, where λ is a monochromatic wavelength and $\Delta\lambda$ the Full Width at Half Maximum of the spectral resolution

[2] The observed FOVs are rotated among them. However in the following chapters, the rotations will not be taken into account because it introduces non-linearity to the system.

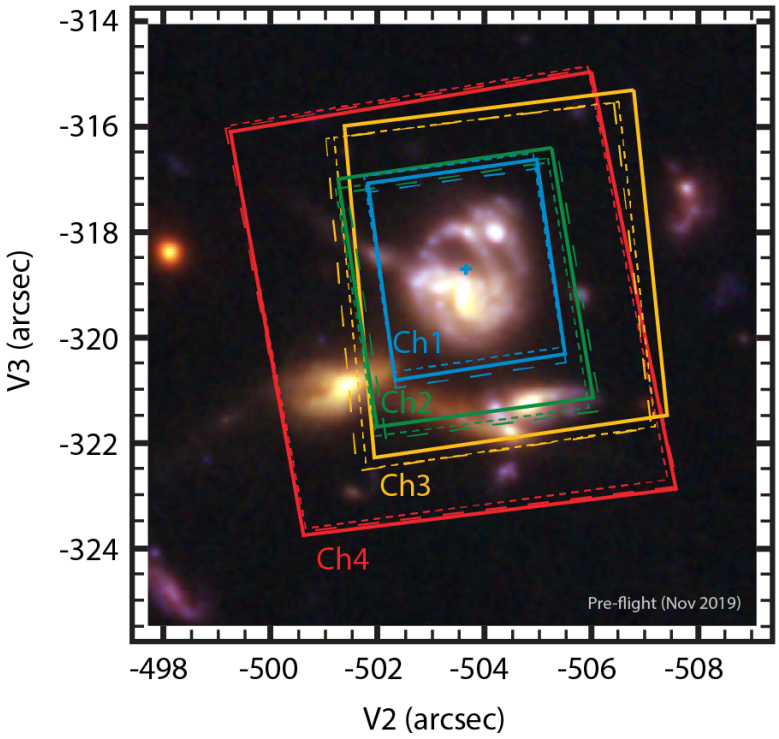

Figure 3.5: Figure showing the co-aligned spatial FOV of the four MRS spectral channels. Edited from: https://jwst-docs.stsci.edu/mid-infrared-instrument/miri-instrumentation/miri-mrs-field-and-coordinates

Fig. 3.6). Table 3.1 gives the spectral range for each spectral channel and sub-band, the different sizes of the observed FOV for each channel, measured in *arcsec*, and the spectral resolving power for each sub-band.

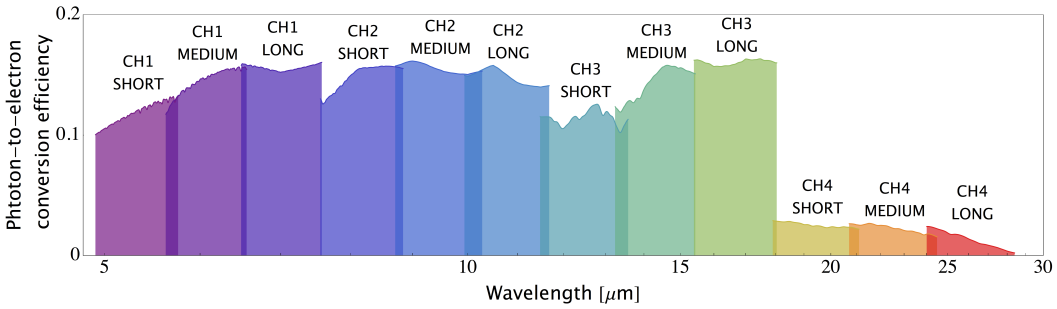

Figure 3.6: wavelength bands response for the MRS instrument. (image credit : https://jwst-docs.stsci.edu/mid-infrared-instrument/miri-observing-modes/miri-medium-resolution-spectroscopy

3.4.2 Integral field units

Each spectral channel incorporates an Integral Field Spectrometer (IFS) to efficiently produce spatial maps of spectroscopic measurements. The four IFS for the MRS instrument comprise an integral field unit (IFU) and a diffraction grating. The IFUs observe a rectangular FOV through several slits in parallel, shown in Figure 3.7, where each slit is reformatted and rearranged at the input of the spectrometer. The number and size of the slits are determined by the design of the IFU for each channel. The width of the slits defines the spectrometer entrance slit. Moreover, the detector pixel size changes across channels (all number are given in Tab. 3.2). We can note that, for channels 1-3, the slit width is less than two pixels, which means that these three channels are undersampled spectrally.

3.4.3 Spectrometer

The optics of spectrometers generally contains at least two lenses (or mirrors): (1) a collimating lens (or mirror) to obtain a parallel light beam, and (2) a focusing lens (or mirror) that projects the image of the input slit dispersed by the grating onto the detector. Between these two lenses (or mirrors), a diffraction grating is placed. The light entering the grating is dispersed at wavelength-dependent angles and then arrives on the detector at wavelength-dependent spatial positions (see Fig. 3.8).

Ideally, the image on the detector plane for a monochromatic (at a wavelength λ) and punctual source looks like a Dirac. But this is not the case because of the diffraction. For a monochromatic point source at wavelength λ, the response of an ideal grating (or the spectral PSF), denoted h_r, depends on the angle of incidence

Channel name Spectral range (μm)	FOV (arcsec)	Sub-band name Spectral range (μm)	Resolving Power ($\lambda/\Delta\lambda$)
Channel 1 $4.88 - 7.52$	3.2×3.7	Short (A) $4.88 - 5.75$	$3,320 - 3,710$
		Medium (B) $5.63 - 6.63$	$3,190 - 3,750$
		Long (C) $6.41 - 7.52$	$3,100 - 3,610$
Channel 2 $7.48 - 11.75$	4×4.8	Short (A) $7.48 - 8.76$	$2,990 - 3,110$
		Medium (B) $8.71 - 10.23$	$2,750 - 3,170$
		Long (C) $10.02 - 11.75$	$2,860 - 3,330$
Channel 3 $11.52 - 18.08$	5.5×6.2	Short (A) $11.52 - 13.49$	$2,530 - 2,880$
		Medium (B) $13.36 - 15.65$	$1,790 - 2,640$
		Long (C) $15.43 - 18.08$	$1,980 - 2,790$
Channel 4 $17.65 - 28.34$	6.9×7.9	Short (A) $17.65 - 20.94$	$1,460 - 1,930$
		Medium (B) $20.41 - 24.22$	$1,680 - 1,770$
		Long (C) $23.88 - 28.34$	$1,630 - 1,330$

Table 3.1: Properties of the different spectral channels and sub-bands of the MRS instrument.

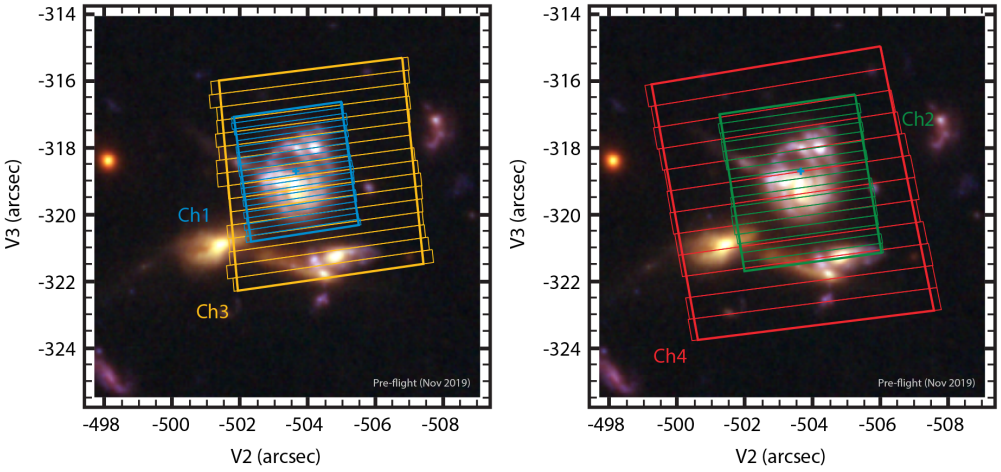

Figure 3.7: Figure showing the IFU for channels 1 and 3 (left image) and channels 2 and 4 (right image). Edited from: https://jwst-docs.stsci.edu/mid-infrared-instrument/miri-instrumentation/miri-mrs-field-and-coordinates

Channel name Spectral range (μm)	FOV (arcsec)	Slit number	Slit width (arcsec)	Pixel size (arcsec)
Channel 1 $4.88 - 7.52$	3.2×3.7	21	0.176	0.196
Channel 2 $7.48 - 11.75$	4×4.8	17	0.277	0.196
Channel 3 $11.52 - 18.08$	5.5×6.2	16	0.387	0.245
Channel 4 $17.65 - 28.34$	6.9×7.9	12	0.645	0.273

Table 3.2: Slit number, slit size and pixel size of the different spectral channels of the MRS instrument.

θ_β and the output angle θ (that depends linearly on λ) shown in Fig. 3.8. It can be expressed as [Pérez 2004]):

$$h_r(\theta, \theta_\beta, \lambda) = B \, \mathrm{sinc}^2 \left(\pi L \left(\frac{\sin(\theta) - \sin(\theta_\beta)}{\lambda} - \frac{m}{a} \right) \right). \tag{3.3}$$

We consider here a calibrated instrument where the angle of incidence θ_β can be related to β, the spatial position of the source in the input slit. Given the small size of the slit width, the variations of β are relatively small. Consequently, using the small angle hypothesis, $\sin(\theta_\beta)$ in Eq. (3.3) can be approximated to β, and $\sin(\theta)$ to the position of the output on the detector, denoted λ'. Moreover, L refers to the width of the grating instrument, and a to the grid step (the distance between two successive grooves). The response of the gratings is centered on m/a, where m denotes the order of the diffraction. For the MRS instrument, the spectral channels enable the use of diffraction gratings in first order ($m = 1$).

We show in Fig. 3.9(a) spectral PSFs for three monochromatic point sources at wavelengths $\lambda = 10$, 15 and 25 μm located at the same spatial position β inside the slit. First, we see that the PSFs peak at the input wavelenght λ. Moreover, the PSFs becomes broader with the increasing wavelengths. Hence, the output of the spectrometer is spectrally non-stationary.

In Fig. 3.9(b), we illustrate the influence of the spatial position β inside the slit (in arcseconds) on the spatial position λ' of the PSF onto the detector array. We see that identical punctual sources, placed at different spatial positions β inside the slit, are spectrally separated on the detector plane.

3.4.4 Detector

The detector is a device that converts for each pixel the incident photons into electrons. The MRS instrument contains two 1024×1024 detectors for the spectral channels (1-2) and (3-4), respectively. The diffracted light within each slit is projected onto 2D detectors, spanning a spatial dimension along one axis and a spectral dimension along the other (Fig. 3.10 (Middle)). The resulting spectral image on the detectors is not straightforward to analyze. The flux measured in each pixel is associated with one spectral wavelength and one spatial location. Therefore, a reconstruction process is imposed, allowing to reconstruct 3D cubes from a set of 2D measurements (Fig. 3.10 (Right)).

Before applying the 3D reconstruction procedure, a calibration step is required to convert the measurements from instrumental to spatial and spectral physical units. It is also necessary to correct the instrumental artefacts and distortions [Wells 2015, Labiano 2016]. For instance, the MRS calibration includes, to name a few, a flat-field correction to cancel the artefacts caused by sensitivity variations between pixels, a stray-light correction to remove unwanted light originated from the MRS components due to their own heat, and a fringe correction caused by interference effects in the detector. A calibration pipeline is being developed and tested by the Space

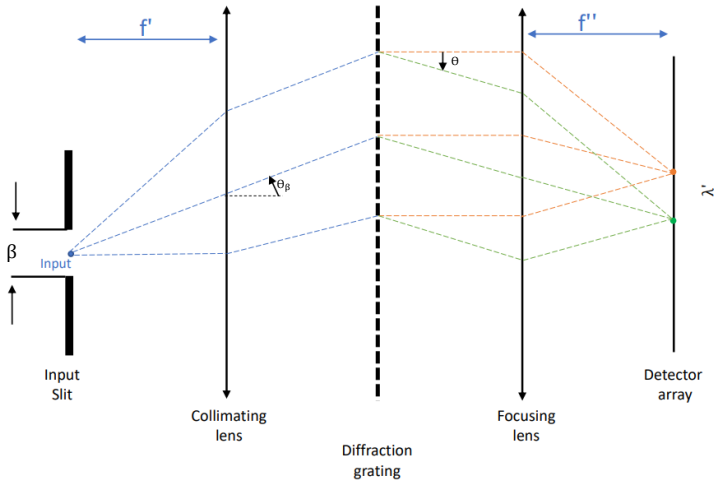

Figure 3.8: Illustration of the optical scheme for a spectrometer. It includes a collimating lens (or mirror), a diffraction gratings and a focusing lens (or mirror). A light source, placed inside the input slit at spatial position β, is spectrally diffracted then projected onto the detector array at a wavelength-dependent position.

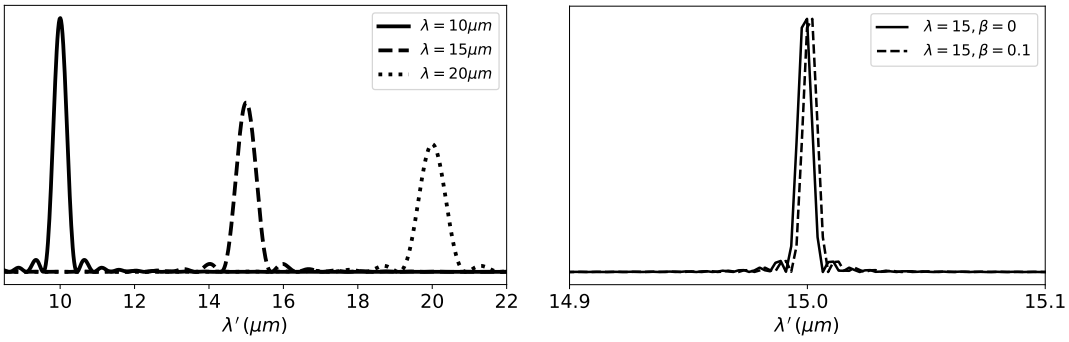

(a) (b)

Figure 3.9: Cuts across monochromatic punctual sources, diffracted and projected onto a detector array, (a) for three monochromatic point sources at $\lambda = 10$, 15, and 20 μm entering the input slit with the same spatial position β, and (b) for two identical punctual monochromatic sources at $\lambda = 15\,\mu$m, but placed at different β (in arcseconds).

Telescope Science Institute (STScI) [3] to calibrate the measurements acquired by the

[3] https://jwst-pipeline.readthedocs.io/en/latest/jwst/introduction.html

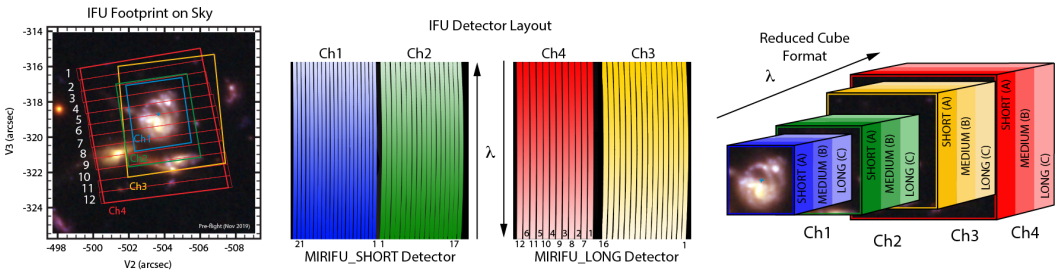

Figure 3.10: (Left): FOV observed through several slits coming from different channels. (Middle): Measurements from each spatio-spectral selection projected onto 2D detectors. (Right) Post-processed 3D data-cube from 2D measurements.
https://jwst-docs.stsci.edu/mid-infrared-instrument/miri-observing-modes/miri-medium-resolution-spectroscopy)

JWST instruments, including the MRS [Labiano 2016, Bushouse 2015].

3.4.5 Dithering

Ideal sampling of the image by the detector should provide at least 2 pixels across the full width at half maximum (FWHM) of the PSF, which is not the case for the MRS instrument. Fig. 3.11 shows the Full Width at Half Maximum (FWHM) of a point source as a function of the wavelength (solid black line). The dashed line denotes the ideal sampling, which is half of the FWHM. In addition, the colored solid and dashed lines for each channel denote the actual sampling of the MRS along and across the slits, respectively. This figure shows that the spatial sampling of the image by the detectors is insufficient at all wavelength values, particularly at the shortest wavelengths within each channel. Therefore, the dithering method is wildly exploited for astrophysical observations to compensate for the loss of information and improve the spatial sampling [Hook 2000]. This method slightly shifts the telescope pointings between exposures following a specific pattern. We have seen that the MRS instrument holds four spectral channels, each with different slit width and pixel size. Since all the four channels are observed simultaneously, the dithering pattern which is selected[4] is necessarily the same for all channels.

3.5 Conclusion

The MRS instrument onboard the JWST observes a 2D+λ sky image denoted $\boldsymbol{x}$ measuring the infrared range and produces a set of measurements $\boldsymbol{y}$ projected onto

[4]https://jwst-docs.stsci.edu/mid-infrared-instrument/miri-operations/miri-dithering/miri-mrs-dithering

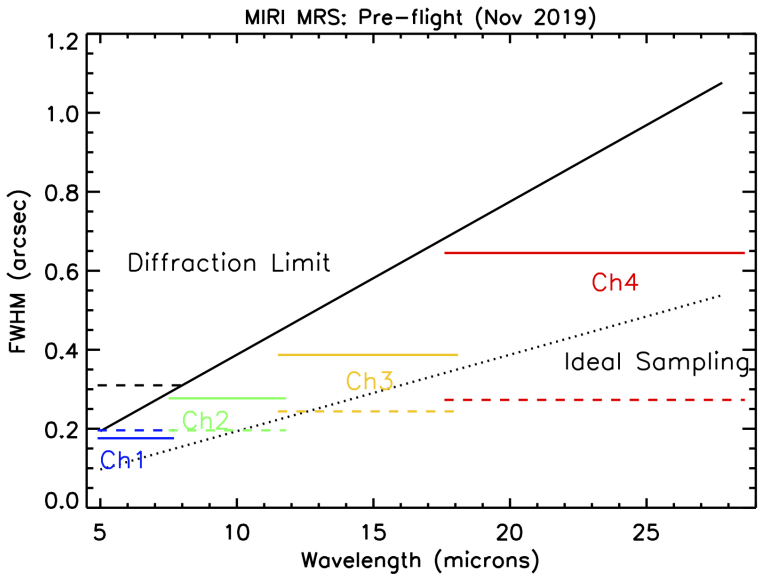

Figure 3.11: MRS spatial resolution as a function of wavelength, taken from https://jwst-docs.stsci.edu/mid-infrared-instrument/miri-operations/miri-dithering/miri-mrs-dithering.

2D detectors. These measurements, however, are spatially and spectrally modified and degraded by the complex components of the instruments presented in this chapter. We particularly account for the following optical issues:

1. The optical system of the telescope projects the collected infrared light on the focal plane of the telescope where the MRS instrument is mounted. However, the optical system is limited by the diffraction [Goodman 1996], as shown in Section 3.3, and introduces a wavelength dependent spatial blurring to the focused sky images. The response of the optical system, or spatial PSF, can be numerically provided with the WebbPSF simulator [Perrin 2014].

2. The MRS observes different parts of the diffracted object. In particular, the spectral range is observed by different spectral channels, and the spatial field of view related to each channel is observed through several slits in parallel (IFU) as shown in Section 3.4. The characteristics of the channels and IFU are known [Wells 2015] and reported in Tables 3.1 and 3.2.

3. The wavelength dispersing instrument, which is made of diffraction gratings for the MRS case, is not perfect and introduces a spectral blurring to the diffracted light inside each slit that depends on the wavelength as shown in Figure 3.9. The response of the grating, or the spectral PSF, can be mathematically modeled and provided in Eq. (3.3).

4. The output of the spectrometer is finally sampled onto 2D detectors with different pixel sizes depending on the channels as reported in Table 3.2. More-

over, the sampling of the image by the detector is insufficient at all wavelengths, as shown in Fig. 3.11. To enhance the spatial resolution lost at the detector, the JWST enables a dithering mode with a pattern shared between all the channels, leading to multi-frame observations.

The spatially and spectrally blurred, truncated and spatially sub-sampled measurements $\boldsymbol{y}$ are not straightforward to analyze, therefore, we rely on the inverse problems approaches to reconstruct the unknown input $\boldsymbol{x}$. In the following chapters, we develop a forward model for the IFS, particularly adapted to the MRS, that links the input $\boldsymbol{x}$ to the measurements $\boldsymbol{y}$ while accounting for the identified instruments limitations and modifications. This forward model is used during the reconstruction process, which mainly includes (1) a data-fusion step that merges the different 2D measurements into a composite 2D+λcube, a (2) deblurring step to invert the effect of the spatial and spectral blurring, and (3) a multi-frame Super-Resolution step [Sung Cheol Park 2003] to enhance the spatial resolution of the reconstructed $\boldsymbol{x}$.

Chapter 4

Hyperspectral reconstruction from 2D IFS measurements

Contents

4.1 Introduction

A hyperspectral (HS) image is a 2D+λ image, with two spatial dimensions (i, j) and one spectral dimension l. However, and as discussed in chapter 2, direct observation of 3D images is not possible because the detectors are 2D. Several techniques are adopted to acquire 3D images, particularly using Integral Field Spectrometers (IFS) [Vives 2008b]. They observe a spatial field of view (FOV) through several slits in parallel via optical instruments, such as a fiber array or an image slicer. The light within each slit is diffracted and projected onto 2D detectors (one spatial dimension and one spectral dimension). However, the analysis of the measurements is not straightforward and requires a stage of reconstruction.

This chapter addresses the reconstruction of a discrete 2D+λ image with a high spatial and spectral resolution from a set of 2D measurements with high spectral resolution. Several challenges arise during the reconstruction process since the spatial and spectral responses of the acquisition system significantly degrade the measurements. First, because of the diffraction phenomenon [Goodman 1996], the optics introduce a spatial blurring that depends on the wavelength. Concretely, the input is more blurred at higher wavelengths. Second, the light dispersion, done with prisms or gratings, introduces a spectral blurring also wavelength-dependent [Pérez 2004]. Finally, the signal at the output of the dispersion system is sampled onto different detectors with varying spatial sampling steps. However, this sampling can be insufficient at all wavelengths, leading to a loss of spatial information. A "dithering" method [Fruchter 2002, Hook 2000] is then adopted to compensate the loss of information, consisting of observing different FOV of the same object by slightly shifting the pointing of the measuring instrument. The multi-frame measurements resulted from multiple pointing lead to a super-resolution (SR) problem [Sung Cheol Park 2003].

Several SR reconstruction algorithms have been proposed to restore the original 2D+λ image. The state-of-art algorithm for SR reconstruction is based on the shift and addition (S&A) method [Farsiu 2003, Hook 2000]. It combines all the 2D measurements from the different pointings (after correcting the detector effects) to enhance the spatial resolution of the reconstructed object. This method provides fast algorithms but does not account for spatial and spectral blurring. For short-wavelength observations, applying the S&A algorithm can be sufficient since the blurring is not important. However, we are considering instruments with broad spectral range in the long wavelengths, and the blurring effects are significant (and also the under-sampling). Thus, the S&A method can be followed by a deblurring step, for instance total variation (TV) [Chambolle 2011]. However, for hyperspectral images this additional step is not optimal since it is applied separately for each spectral band, without considering any correlation between bands.

Our proposed approach relies on an explicit forward model which describes the IFS instrument. It provides a mathematical relationship between the unknown 2D+λ input image and a set of blurred, truncated, and sampled 2D multi-frame

measurements with heterogeneous sampling steps. The reconstruction algorithm is based on the regularized least square method [Demoment 1989]. It consists of optimizing a criterion composed of a data fidelity term that models the instrument effects using the developed forward model and a convex regularization term that preserves the edges by preventing excessive penalization of high spatial gradients [Idier 2001a]. Our forward model is primarily developed for the Mid Resolution Spectrometer of the Mid Infrared Instrument on board the James Webb space telescope (JWST) [Wells 2015], detailed in chapter 3.

This chapter is organized as follows. First, we present a new explicit forward model for the IFS instrument that produces a set of blurred, truncated, and aliased 2D multi-frame measurements given a 2D+λ image. Second, from the developed forward model and the 2D measurements, we formulate two reconstruction algorithms (the state-of-art and the proposed) to estimate the unknown 2D+λ input. Furthermore, we test the forward and reconstruction algorithms on two sets of synthetic inputs with various spatial and spectral distributions. To highlight the importance of the convex edge-preserving regularization choice, we also compare the reconstruction algorithm to the classic l_2 regularization algorithm [Tikhonov 1995]. Finally, we examine the influence of the noise level on the performance of the reconstruction algorithms.

4.2 Forward model

The forward model takes as input a discrete 2D+λ hyperspectral image denoted by a vector $\boldsymbol{x}[i,j,l] \in \mathbb{R}^{I\times J\times L}$, where $(i,j) \in [1,\dots,I]\times[1,\dots,J]$ are the spatial dimensions and $l \in [1,\dots,L]$ the spectral dimension. The input is uniformly sampled with (T_i, T_j) the spatial steps, and T_l the spectral step.

4.2.1 Spatial filtering

The optical system collects the light of the 2D+λ input and focuses sky images on the focal plane where the IFS instrument is mounted. However, because of the diffraction phenomenon [Goodman 1996], the focused images are spatially blurred. The response of the optical system, also known as the spatial point spread function (PSF), is spectrally non-invariant since it varies linearly with the wavelength. On the other hand, the PSF at all wavelengths is assumed to be spatially stationary. Therefore, the spatial filtering writes as a 2D spatial convolution *that depends on the wavelength* between the original 2D+λ image and a discrete PSF $\boldsymbol{h}$, also sampled with a step size (T_i, T_j). Thus, the focused sky image writes

$$\boldsymbol{x}_{\text{opt}}[i,j,l] = \sum_{i',j'} \boldsymbol{x}[i',j',l]\boldsymbol{h}[i-i',j-j',l]. \tag{4.1}$$

We illustrate in Fig. 4.1 the effect of this spatial filtering for three synthetic monochromatic images as original input at wavelengths 5 μm, 15 μm and 25 μm, respectively.

The monochromatic PSFs in the figure are specific to the JWST and simulated with the official WebbPSF tool [Perrin 2014]. However, other forms of PSFs can be considered. The spatial convolution between the input objects and its corresponding PSF results in blurred images, with more blur as the wavelength increases.

For fast computation, the spatial convolution is calculated using the discrete Fourier transform (DFT) [Hunt 1971]. However, the forward model include spatially truncated observations (see section 4.2.2), since the field of view (FOV) observed by the IFS instrument is smaller than that of the original input, as illustrated in Fig. 4.2 (left). Therefore, working in the Fourier space does not introduce any periodic pattern that may affect the results.

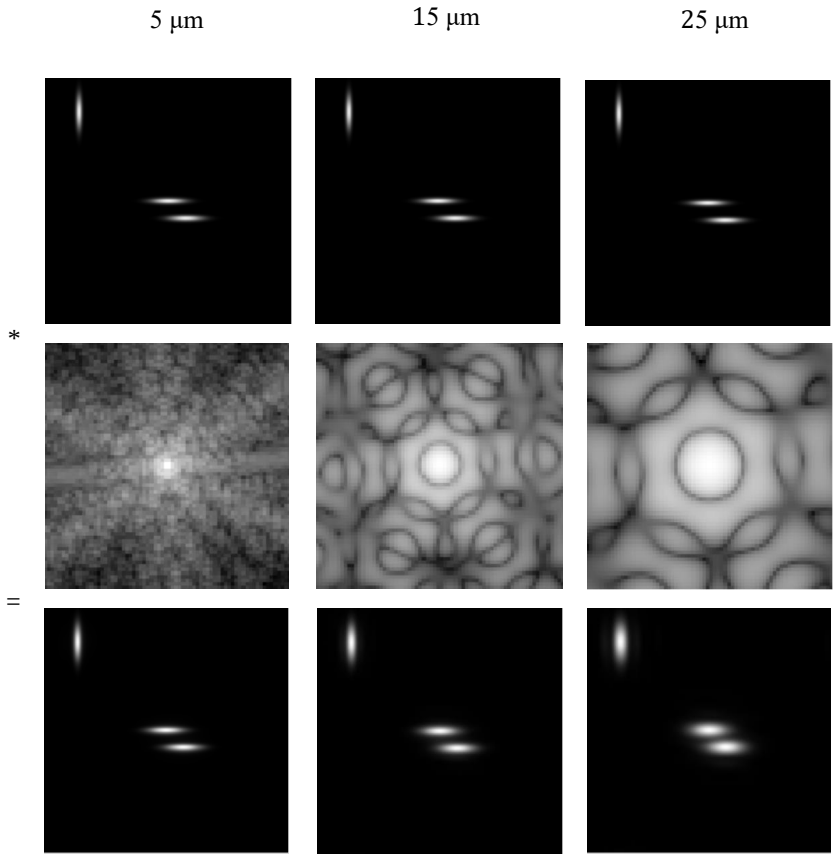

Figure 4.1: Illustration of the spatial filtering: (Top) Three monochromatic synthetic images at wavelength 5, 15 and 25 μm. (Middle) Three monochromatic PSFs simulated with the WebbPSF simulator at the same wavelengths. (Bottom) Filtered images.

4.2.2 Spatio-spectral Field of View

Different regions of the focused sky object $\boldsymbol{x}_{opt}$ are observed with (1) various spatial and spectral fields of views (FOV) and (2) various pointing of the same instrument.

First, $\boldsymbol{x}_{\text{opt}}$ is spectrally divided into distinct channels $c \in [1, \dots, C]$. Each channel possesses its physical properties, spectral range, spatial FOV, and sampling step size. In other words, each channel is perceived as an independent instrument with specific characteristics. In Fig. 4.2(middle), we illustrate the spectral separation of $\boldsymbol{x}_{\text{opt}}$ into four distinct channels with four different FOV. Moreover, the integral field unit (IFU) observes the rectangular FOV through several independent slits in parallel, as illustrated in Fig. 4.2(right). The size and number of slits depend on the selected channel. The spectral selection into distinct channels and the spatial selection into slits with distinct widths and lengths are modeled by multiplying $\boldsymbol{x}_{\text{opt}}$ by channel windows:

$$\begin{cases} \boldsymbol{w}_c[i,j,l] \neq 0 & \forall (i,j,l) \in (\mathcal{I}_c, \mathcal{J}_c, \mathcal{L}_c) \\ \boldsymbol{w}_c[i,j,l] = 0 & \text{otherwise,} \end{cases} \tag{4.2}$$

where $(\mathcal{I}_c, \mathcal{J}_c, \mathcal{L}_c)$ are convex subsets of $[1, \dots, I] \times [1, \dots, J] \times [1, \dots, L]$. We have considered the simple case, where the spatial window size $(\Delta_{i,c}, \Delta_{j,c})$, specific for each channel, is assumed to be a multiple of the sampling step size of the observed object : $(\Delta_{i,c}, \Delta_{j,c}) = (n_c T_i, m_c T_j)$, with $(n_c, m_c) \in \mathbb{N}^2$.

Second, the forward model allows the dithering mode, which is observing different spatial FOV of the same object by slightly shifting the pointing of the measuring instrument. The spatial shifts, indexed by p, are shared between all channels. The pointing positions $(\Delta_{i,p}, \Delta_{j,p})$ are considered as multiples of the step sizes of the original object: $(\Delta_{i,p}, \Delta_{j,p}) = (i_p T_i, j_p T_j)$, with $(i_p, j_p) \in \mathbb{N}^2$.

Finally, the spatio-spectral FOV selection for a particular pointing writes as a windowing:

$$\boldsymbol{x}_{c,p}[i,j,l] = \boldsymbol{x}_{opt}[i,j,l] \times \boldsymbol{w}_c[i - i_p, j - j_p, l], \tag{4.3}$$

where c and p denotes the selected channel and spatial shift, respectively.

4.2.3 Spectral blurring

For each spatio-spectral cube $\boldsymbol{x}_{c,p}$ the light is redirected towards the entrance of the dispersion instrument (here a grating), which disperses it into a series of monochromatic light projected onto a 2D detector.

Assuming that the instrument is calibrated, the diffraction gratings assimilate to each wavelength input $\lambda = lT_l$ a spatial position $\lambda' = l'T_{l'}$ on the detector (in wavelength unit) with $T_{l'}$ the step size. However, in a more accurate model, the diffraction gratings are not perfect and introduce spectral blurring. We need to model the response of the diffraction system, also known as the spectral PSF.

For a monochromatic punctual source entering the grating at the wavelength lT_l from the particular channel c and the pointing p, the spectral response writes [Pérez 2004]:

$$h_{c,j,p}(l', l) \propto \text{sinc}^2 \left(\pi W \left(\frac{l'T_{l'} - b \times q_{j,p}}{lT_l} - 1 \right) \right). \tag{4.4}$$

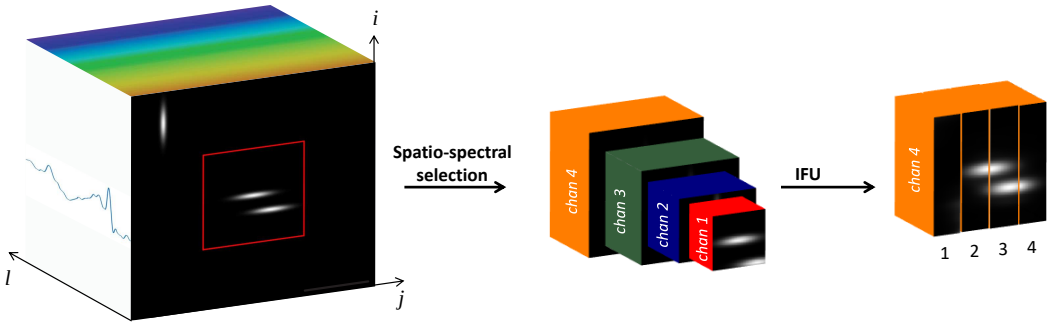

Figure 4.2: Spatio-spectral selection: (Left) Focused object on the focal plane. The red rectangular frame represents the largest FOV observed by the instrument. (Middle) Spatio-spectral selection of the object into four distinct spectral channels with distinct FOV. (Right) Spatial FOV of the fourth channel: it observes through four slits in parallel (the other channels have different number of slits with different sizes).

where $q_{j,p} \in [-\Delta_{j,c}/2, \Delta_{j,c}/2]$ is the relative spatial position of the input source, determined by the position j and pointing p within each spatial window (c, p). This response is independent from the other spatial position, indexed by i.

Several particularities of the spectral PSF are inferred from Eq. (4.4) that we take into account in this work (they are also illustrated in Fig. 4.3) :

1. The spatial position of $\lambda' = l'T'_{l'}$ at the detector depends on the input wavelength $\lambda = lT_l$.

2. The PSF is spectrally not stationary, since it becomes broader with the increase of λ.

3. The relative spatial position of the input source $q_{j,p}$ influences the spatial position of the projected light by introducing shifts to its maximum. The parameter b is a scale factor that converts the spatial position into wavelength.

Moreover, the spectral PSF also depends on W, a parameter related to the length of the grating. It controls the width of the spectral PSF. Thus, it is linked to the usually known spectral resolution $R = \lambda/\Delta\lambda$ where $\Delta\lambda$ refers to the full width at half maximum (FWHM) of the spectral PSF for a wavelength $\lambda = lT_l$ for a particular channel c[1]. $\Delta\lambda$ is obtained using the known form of the FWHM of the spectral PSF in Eq. (4.4) with

$$\Delta\lambda \approx 2 * 1.4\,\lambda/\pi W \tag{4.5}$$

which gives

$$W = 2.8\,R/\pi. \tag{4.6}$$

[1]For the MRS case, the spectral resolution for every spectral channel is given in chapter 3.

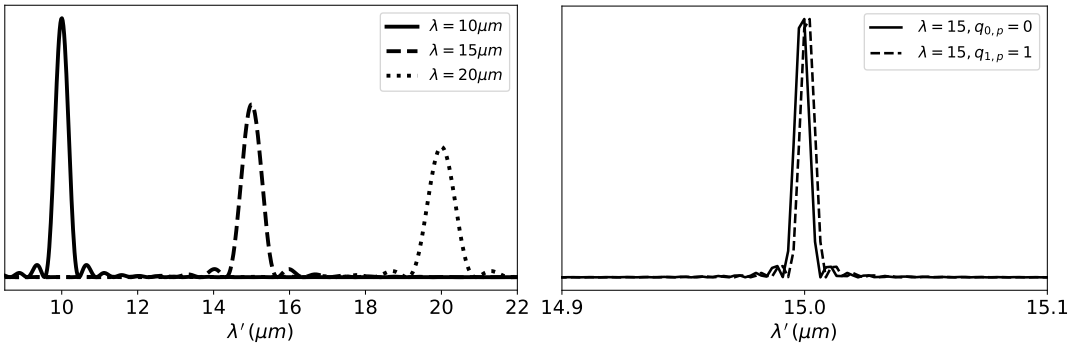

Figure 4.3: (Left) Spectral dependence of the grating response,(Right) influence of the spatial position j of the input source, $q_{j,p}$ for a particular pointing p, on the position of the diffracted light.

Finally, the grating is a non stationary linear system that projects the dispersed light of a particular spatio-spectral selection $\boldsymbol{x}_{c,p}[i,j,l]$ on the detector with

$$\boldsymbol{g}_{c,p}[i,j,l'] = \sum_{l \in \mathcal{L}_c} \boldsymbol{x}_{c,p}[i,j,l]\ \boldsymbol{h}_{c,j,p}[l',l] \tag{4.7}$$

where $l' \in \mathcal{L}'_c$ refers to the wavelength sampled on detector. $\boldsymbol{h}_{c,j}[l',l]$, is the discrete form of the spectral PSF introduced in Eq. (4.4). Note that our model is not limited to this specific spectral response and can easily be replaced by another. Moreover, since the grating is a non stationary system, Eq. (4.7) is not a spectral convolution.

4.2.4 Spatial Sampling

The 3D cubes $\boldsymbol{g}_{c,p}[i,j,l']$, spatially and spectrally blurred by the responses of the acquisition system, are not directly observed since the detectors are 2D. They are spatially sampled along both the j-axis and the i-axis, with sampling steps depending on the channel.

First, the nature of the spectral response in Eq. (4.7) imposes that all wavelengths at all spatial positions inside $\mathcal{J}_{c,p}$ contribute to the output of the gratings. Since the system is linear, these contributions are summed on the detector. Therefore, the sampling of $\boldsymbol{g}_{c,p}[i,j,l']$ along the j-axis is imposed by the j-width of the window w_c, variable across channels.

On the other hand, the sampling of $\boldsymbol{g}_{c,p}[i,j,l']$ along the i-axis is imposed by the detector step size, most often larger than T_i (sampling step of the input along the i-axis), and which depends on the channel. Here, since we are working in the discrete case, we suppose that the step size of the detector for each channel c is a multiple of T_i, that is $T_{i'} = d_c T_i$, with $d_c \in \mathbb{N}$.

The projection of the 3D spatio-spectral selections onto 2D detectors is illustrated in Fig. 4.4. The light at wavelength indexed by $l \in \mathcal{L}_c$ within each selection c is dispersed and sampled on the detector, at wavelength indexed by l'. In addition,

the spatial position along the j-axis with $j \in \mathcal{J}_c$ are summed at the detector along the dispersion axis (indexed by l') writing

$$\boldsymbol{g}'_{c,p}[i, l'] = \sum_{j \in \mathcal{J}_{c,p}} g_{c,p}[i, j, l'] \tag{4.8}$$

Because of this summation, the projected output of a 3D selection becomes 2D (spatial dimension along the i-axis and a spectral dimension along the l' axis, influenced by $l \in \mathcal{L}_c$ and $j \in \mathcal{J}_c$). Finally, the spatial positions along the i-axis are sampled along the other axis of the detector and indexed by i'.

Since the step size of the detector and the j-width of the window w_c are larger than the step size of the input, the projected measurements are under-sampled and aliased. This loss of spatial resolution motivates the use of different pointing (i_p, j_p) of the instrument. Finally, the 2D measurements $\boldsymbol{y}_{c,p}$ for a particular channel c and pointing p writes

$$\boldsymbol{y}_{c,p}[i', l'] = \sum_{i=i'd_c}^{(i'+1)d_c} \boldsymbol{g}'_{c,p}[i, l'], \text{ with } i \in \mathcal{I}_{c,p} \tag{4.9}$$

where i' and l' denotes the spatial and spectral index respectively on the 2D detector. In practice, the summation over i is computed by convolution with a square impulse response of size d_c followed by sub-sampling every d_c elements.

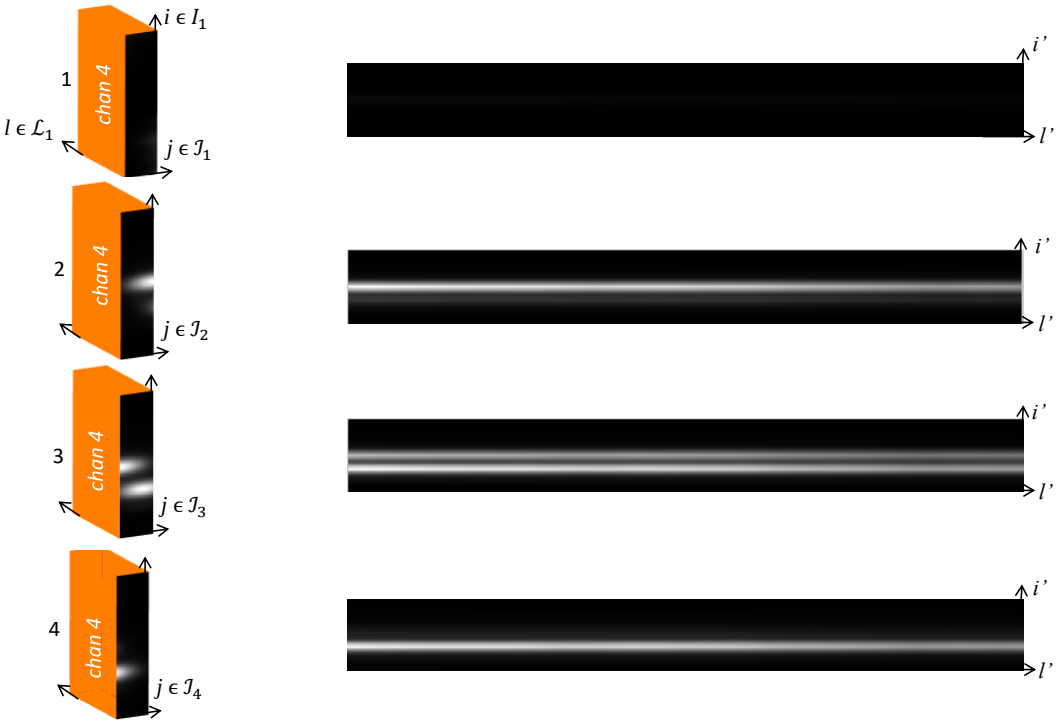

Figure 4.4: Diffracted and projected measurements onto 2D detectors

4.2.5 Complete model

To conclude, we developed a linear but non-stationary forward model that reproduces multi-frame 2D measurements $\boldsymbol{y}_{c,p}$ by accounting for the response of the measuring instrument. We will see in the next section that it is adapted to the inversion algorithm and allows the extraction of an observation matrix $\boldsymbol{H}$ and its transpose $\boldsymbol{H}^t$. The full model then writes:

$$\boldsymbol{y}_{c,p}[i',l'] = \sum_{i,j}\sum_{l\in\mathcal{L}_c}\left(\boldsymbol{x}[i,j,l] \underset{i,j}{*} \boldsymbol{h}[i,j,l]\right)\boldsymbol{w}_c[i-i_p, j-j_p, l] \times \boldsymbol{h}_{c,j,p}[l',l]. \quad (4.10)$$

Our model can be summarized as

$$\boldsymbol{y}_{c,p} = \boldsymbol{H}_{c,p}\boldsymbol{x} = \boldsymbol{\Sigma}_{i,j,l}\boldsymbol{R}_{c,j,p}\boldsymbol{W}_{c,p}\boldsymbol{C}\boldsymbol{x}. \quad (4.11)$$

Here $\boldsymbol{C}$ computes the spatial convolution at each wavelength, $\boldsymbol{W}_{c,p}$ denotes the windowing, $\boldsymbol{R}_{c,j,p}$ is a multiplication operator for the spectral blurring and $\boldsymbol{\Sigma}_{i,j,l}$ is a summation on i, j and l to model the spatial and spectral integration on the detector. Then, the concatenated measurements give $\boldsymbol{y} = \boldsymbol{H}\boldsymbol{x}$ with $\boldsymbol{y}^t = [\boldsymbol{y}^t_{0,0}, \ldots, \boldsymbol{y}^t_{C,P}]$ and $\boldsymbol{H}^t = [\boldsymbol{H}^t_{0,0}, \ldots, \boldsymbol{H}^t_{C,P}]$ the full data model. The adjoint (transpose) operator then writes

$$\boldsymbol{e}_{c,p} = \boldsymbol{H}^t_{c,p}\boldsymbol{y}_{c,p} = \boldsymbol{C}^t\boldsymbol{W}^t_{c,p}\boldsymbol{R}^t\boldsymbol{\Sigma}^t_{i,j,l}\boldsymbol{y}_{c,p} \quad (4.12)$$

with $\boldsymbol{\Sigma}^t_{i,j,l}$ a duplication operator, $\boldsymbol{R}$ a multiplication with a flipped response, $\boldsymbol{W}^t_{c,p}$ a zero filling operator and $\boldsymbol{C}^t$ a convolution with flipped response. This model is relatively complex and accounts for several effects:

- 2D spatial convolutions that depend on the wavelengths described in Eq. (4.1).
- Spatio-spectral windowing that takes into account different spatial pointing and different spatio-spectral FOV described in Eq. (4.3).
- Non-stationary spectral blurring with varying grating parameters described in Eq. (4.7).
- the spatial and spectral sampling, with steps specific for each detector and different from the input sky's sampling steps, described in Eq. (4.10).
- Multi-frame observations, with subpixel shifts leading to a Super-Resolution problem.

4.3 Reconstruction

We present in this section two SR algorithms to reconstruct the unknown 2D+λ input image $\boldsymbol{x}$ from a set of blurred, truncated, and aliased 2D multi-frame measurements $\boldsymbol{y}_{c,p}$. The first is the state-of-art algorithm, which is a fast multi-frame SR reconstruction algorithm based on the shift and addition (S&A) method [Farsiu 2003, Hook 2000]. The second is the proposed algorithm, based on the regularized least square approaches with a convex edge-preserving regularization [Allain 2006].

4.3.1 State-of-art algorithm

Since the unknown input $\boldsymbol{x}[i,j,l]$ is 3D and the acquired measurements $\boldsymbol{y}_{c,p}[i',l']$ are 2D, a post-processing technique is required. First, for a fixed pointing p, this technique combines the spatio-spectral information of the measurements acquired from the different selections c, to produce a composite 3D data cube. It is illustrated in Fig. 4.5. The left image shows the spatial FOV observed through the IFU for each spectral channel [2]. The center figure shows the 2D raw measurements acquired from the different channels and projected onto different detectors. Finally, the right image shows the reconstructed 3D data cube, where a spatio-spectral FOV is associated with each channel.

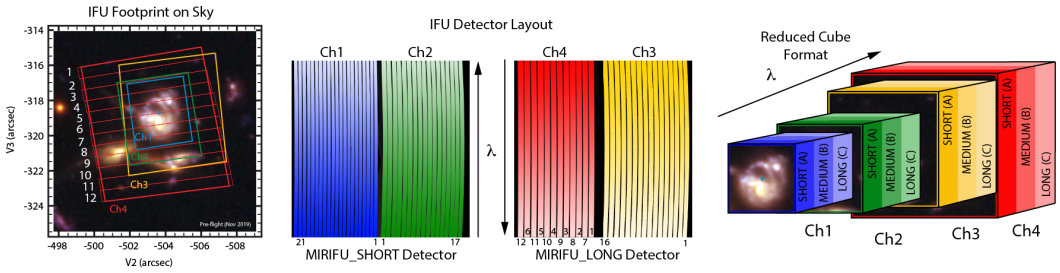

Figure 4.5: (Left): FOV observed through several slits coming from different channels. (Middle): Measurements from each spatio-spectral selection projected onto 2D detectors. (Right) Post-processed 3D data-cube from 2D measurements. Taken from https://jwst-docs.stsci.edu/mid-infrared-instrument/miri-observing-modes/miri-medium-resolution-spectroscopy.

The different pointings p of the instrument allow multi-frame observations of the same scene, with subpixel shifts. By combining all these observations, the spatial resolution lost because of the detector integration can be compensated. This combination is achieved using the shift and add method (S&A) [Farsiu 2003, Hook 2000], which is shifting $\boldsymbol{y}_{c,p}[i',j']$ for every observation to align them and then co-add the results. Mathematically, this method yields to the minimization of a least-square criterion [Demoment 1989] with

$$\hat{\boldsymbol{x}}_{\mathrm{SA}c,p} = \arg\min_{\boldsymbol{x}} \|\boldsymbol{y} - \boldsymbol{S}\boldsymbol{x}\|^2 \tag{4.13}$$

$$= (\boldsymbol{S}^t\boldsymbol{S})^{-1} \sum_i \boldsymbol{S}^t_{c,p}\boldsymbol{y}_{c,p}. \tag{4.14}$$

$\boldsymbol{S}$ is a sub-sampling matrix, equivalent to the model developed in Section 4.2, but where the spatial and spectral PSF are a Dirac, and the spectral upsampling is not considered. In that case, $\boldsymbol{S}^t_{c,p}$ is the spatial upsampling matrix for a particular

[2] The different channels are in different colors. In this work, we do not take into account the rotation of the spatial FOVs between channels

channel c and pointing p, and $(\boldsymbol{S}^t\boldsymbol{S})^{-1}$ is a diagonal normalization matrix that counts the number of time a pixel is measured. This method provides a fast and non-iterative algorithm. However, non-stationary spatial and spectral blurring are not taken into account. Moreover, the shift-and-add algorithm is applied separately for each channel since they have different characteristics.

4.3.2 Proposed algorithm

We propose a new SR algorithm to reconstruct the 2D+λ input image. Our approach relies on the full-forward model, developed in Eq. (4.10), that considers non-stationary spatial and spectral blurring, different observations from multiple sources, and different spatial sampling. The reconstruction with the Least-Square approach presented in the previous sub-section suffers from ill-conditioning, mainly because of the blurring effects [Idier 2001b]. Therefore, we base our approach on the regularized least square method, that relies on the optimization of a cost function composed of a data fitting term and a regularization term $\mathcal{R}(\boldsymbol{x})$ with

$$\hat{\boldsymbol{x}} = \arg\min_{\boldsymbol{x}} \|\boldsymbol{y} - \boldsymbol{H}\boldsymbol{x}\|^2 + \mathcal{R}(\boldsymbol{x}). \tag{4.15}$$

As discussed in Chapter 2, different regularization have been proposed in the literature. The l_2 regularization [Tikhonov 1995] enforces smoothness to the solution and provides fast reconstruction algorithms but fails to preserve high gradient values, and also introduces ringing artifacts to the solution. To overcome these limitations, non-quadratic regularizations are used such as Total variation (TV) regularization [Rudin 1992] or dictionary based approaches with sparsity [Zhao 2011]. However, these methods introduce cartoon-like effects to the solution. On the other hand, half-quadratic approaches (*i.e.* l_2/l_1-norm, [Idier 2001a, Geman 1992, Geman 1995]) promotes smoothness to the solution while preserving high gradient values (*i.e.* contours and edges). This is why we have decided to use such approaches.

The optimised cost function, denoted $\hat{\boldsymbol{x}}_{hq}$, is expressed as

$$\hat{\boldsymbol{x}}_{hq} = \arg\min_{\boldsymbol{x}} \|\boldsymbol{y} - \boldsymbol{H}\boldsymbol{x}\|^2 + \mu_{\text{spat}} \sum_{u \in \mathcal{U}} \phi(\boldsymbol{v}_u^t \boldsymbol{x}) + \mu_{\text{spec}} \sum_{w \in \mathcal{W}} \phi(\boldsymbol{v}_w^t \boldsymbol{x}). \tag{4.16}$$

$\boldsymbol{v}_u$ is the first order difference operator between two pixels in row and columns along the spatial dimension, and $\boldsymbol{v}_w$ the first order difference operator along the spectral dimension. μ_{spat} and μ_{spec} denote the regularization parameters used as a trade off for spatial smoothness between pixels and spectral smoothness between wavelengths, respectively. Finally ϕ denotes a convex potential function. Several options of convex potential functions for half-quadratic regularization are found [Charbonnier 1997]. We choose in this work the Huber function with:

$$\phi(\delta, T) = \begin{cases} \delta^2, & \text{if } |\delta| \leq T. \\ 2T|\delta| - T^2 & \text{otherwise, } T \in \mathbb{R}^+. \end{cases} \tag{4.17}$$

Nevertheless, other convex potential function for edge-preserving can be easily considered such as Hyperbolic function. The Huber potential is convex and continuously differentiable. It takes a quadratic behavior below the threshold T to promote denoising and smoothness, and a linear behavior above the threshold for edge-preserving purposes.

Two different formulations of the half quadratic regularization are proposed by Geman and Reynolds (GR) [Geman 1992], and Geman and Yang (GY) [Geman 1995] respectively to solve (4.16). Both formulations provide iterative optimization algorithms that benefit from global convergence. The GY formulation provides overall more efficient algorithms when the Hessian matrix (related to the observation matrix $\boldsymbol{H}$) can be inverted at a low cost [Allain 2006]. In our case, the fast inversion is not applicable because the forward model is already computationally burden. Therefore, we adopt the half-quadratic formulation proposed by (GR) [Geman 1992] which provides more robust algorithms. It consists of introducing to the cost function multiplicative spatial and spectral auxiliary variables $\boldsymbol{b}_{spat} = (b_u)_{u\in\mathcal{U}}$ and $\boldsymbol{b}_{spec} = (b_w)_{w\in\mathcal{W}}$. Consequently, the half-quadratic function ϕ is expressed as the minimum of a quadratic function and a dual auxiliary function $\psi(b)$, related to ϕ (with respect to the auxiliary variable b) writing

$$\phi(b) = \underset{b\in\{0,b_\infty\}}{inf} \left\{ \frac{1}{2} b\delta^2 + \psi(b) \right\}, \quad \forall \delta \in \mathbb{R}. \tag{4.18}$$

The spatial and spectral auxiliary variables $\boldsymbol{b}_{spat}$ and $\boldsymbol{b}_{spec}$ are proportional to the spatial and spectral gradients of $\boldsymbol{x}$, respectively. The higher the gradient, the higher the auxiliary variables. To address the half quadratic strategy proposed by Geman and Reynolds [Geman 1992], we define an augmented cost function $\mathcal{J}*$ using the quadratic surrogate function and the auxiliary variables as

$$\begin{aligned}\mathcal{J}^*(\boldsymbol{x}, \boldsymbol{b}_{spat}, \boldsymbol{b}_{spec}) = \|\boldsymbol{y} - \boldsymbol{H}\boldsymbol{x}\|^2 + \frac{\mu_{spat}}{2} \sum_{u\in\mathcal{U}} \left[b_u (\boldsymbol{v}_u^t \boldsymbol{x})^2 + \psi_{spat}(b_u) \right] \\ + \frac{\mu_{spec}}{2} \sum_{w\in\mathcal{W}} \left[b_w (\boldsymbol{v}_w^t \boldsymbol{x})^2 + \psi_{spec}(b_w) \right]\end{aligned} \tag{4.19}$$

where the augmented cost function $\mathcal{J}^*(\boldsymbol{x}, \boldsymbol{b}_{spat}, \boldsymbol{b}_{spec})$ shares the same minimizer as $\mathcal{J}(\boldsymbol{x})$ with

$$\min_{\boldsymbol{b}_{spat}, \boldsymbol{b}_{spec}} \mathcal{J}^*(\boldsymbol{x}, \boldsymbol{b}_{spat}, \boldsymbol{b}_{spec}) = \mathcal{J}(\boldsymbol{x}). \tag{4.20}$$

Consequently, the half quadratic solution is solved by minimizing $\mathcal{J}*$. The latter combines three terms which are (1) a least square term measuring the fidelity to the data, (2) two quadratic terms expressing the difference between the spatial pixels and spectral wavelengths and which depend on the spatial and spectral auxiliary terms respectively, and (3) spatial and spectral auxiliary functions that only depends on the auxiliary variables. The minimization of the cost function in Eq. (4.20) is solved by iteratively alternating two minimization problems until

convergence [Charbonnier 1997].

$$\hat{\boldsymbol{x}}_{hq}^{(k)} = \underset{\boldsymbol{x}}{\operatorname{argmin}}\, \mathcal{J}^*(\boldsymbol{x}, \boldsymbol{b}_{spat}^{(k-1)}, \boldsymbol{b}_{spec}^{(k-1)}), \tag{4.21}$$

$$\hat{\boldsymbol{b}}_{spat}^{(k)}, \boldsymbol{b}_{spec}^{(k)} = \underset{\boldsymbol{b}_{spat}, \boldsymbol{b}_{spec}}{\operatorname{argmin}}\, \mathcal{J}^*(\boldsymbol{x}^{(k)}, \hat{\boldsymbol{b}}_{spat}, \boldsymbol{b}_{spec}). \tag{4.22}$$

Eq. (4.21) corresponds to the minimization of $\mathcal{J}^*$ with respect to (w.r.t) $\boldsymbol{x}$, yielding to

$$\hat{\boldsymbol{x}}_{hq} = \arg\min_{\boldsymbol{x}} \|\boldsymbol{y} - \boldsymbol{H}\boldsymbol{x}\|^2 + \frac{\mu_{\text{spat}}}{2} \boldsymbol{x}^t \boldsymbol{V}_{spat}^t \boldsymbol{B}_{spat} \boldsymbol{V}_{spat} \boldsymbol{x} + \frac{\mu_{\text{spec}}}{2} \boldsymbol{x}^t \boldsymbol{V}_{spec}^t \boldsymbol{B}_{spec} \boldsymbol{V}_{spec} \boldsymbol{x} \tag{4.23}$$

where $\boldsymbol{B}_{spat} = \text{Diag}(\boldsymbol{b}_{spat})$ and $\boldsymbol{B}_{spec} = \text{Diag}(\boldsymbol{b}_{spec})$.
Moreover, $\boldsymbol{V}_{spat} = [\boldsymbol{v}_1 \dots \boldsymbol{v}_U]^t$, and $\boldsymbol{V}_{spec} = [\boldsymbol{v}_1 \dots \boldsymbol{v}_W]^t$. Therefore, the solution $\hat{\boldsymbol{x}}_{hq}$ is deduced by solving the following linear system

$$\left(\boldsymbol{H}^t\boldsymbol{H} + \mu_{spat}\boldsymbol{V}_{spat}^t\boldsymbol{B}_{spat}\boldsymbol{V}_{spat} + \mu_{spec}\boldsymbol{V}_{spec}^t\boldsymbol{B}_{spec}\boldsymbol{V}_{spec}\right)\boldsymbol{x} = \boldsymbol{H}^t\boldsymbol{y}. \tag{4.24}$$

Eq. (4.24) yields to a closed form expression of the minimizer $\hat{\boldsymbol{x}}_{hq}$. However, solving the problem is untractable because the complete model $\boldsymbol{H}$ is computationally burden. Therefore, the algorithm is solved iteratively using the conjugate gradient algorithm (Algorithm 2) described in section 2.1.3.

Eq. (4.22) corresponds to the minimization of $\mathcal{J}^*$ w.r.t $\boldsymbol{b}_{spat}$ and $\boldsymbol{b}_{spec}$ with

$$\hat{\boldsymbol{b}}_{spat}, \hat{\boldsymbol{b}}_{spec} = \arg\min_{b_w, b_u} \frac{\mu_{spat}}{2} \sum_{u \in \mathcal{U}} b_u (\boldsymbol{v}_u^t \boldsymbol{x})^2 + \psi_{spat}(b_u) + \frac{\mu_{spec}}{2} \sum_{w \in \mathcal{W}} b_w (\boldsymbol{v}_w^t \boldsymbol{x})^2 + \psi_{spec}(b_w). \tag{4.25}$$

The minimization problem in Eq. (4.25) can be achieved in parallel. In addition, b_u and b_w are expressed explicitly and does not require a known form of ψ_{spat} and ψ_{spec} since the infimum of the Eq. 4.18 is uniquely reached when [Idier 2001a]

$$\hat{b}_u = \frac{\phi'(\boldsymbol{v}_u^t \boldsymbol{x})}{2\boldsymbol{v}_u^t \boldsymbol{x}}, \tag{4.26}$$

and similarly for the spectral dimension

$$\hat{b}_w = \frac{\phi'(\boldsymbol{v}_w^t \boldsymbol{x})}{2\boldsymbol{v}_w^t \boldsymbol{x}}, \tag{4.27}$$

where $\hat{\boldsymbol{b}}_{spat} = (\hat{b}_u)_{u \in \mathcal{U}}$ and $\hat{\boldsymbol{b}}_{spec} = (\hat{b}_w)_{w \in \mathcal{W}}$ and ϕ' is the first Huber derivative.

4.4 Simulation and Results

4.4.1 Description of the spatio-spectral input images

The forward model described in section 4.2 is general but primarily developed for the Mid Resolution Spectrometer of the Mid Infrared Instrument onboard the JWST [Wells 2015], detailed in Chapter 3. It is used to reproduce multi-frame 2D measurements for a given 2D+λ input image. The forward model and the proposed reconstruction algorithm have been tested on two synthetic objects with complex spatial and spectral distributions.

The first object, denoted obj_1, contains a spatial distribution with sharp edges, illustrated in Fig. 4.6. It is uniformly sampled on a spatial grid with a step size of $T_i = T_j = 0.1$ arcsec and a size of $I \times J = 120 \times 120$ pixels. The spectral distribution of this object is provided by [Berné 2007] and has been computed from astrophysical measurements. The spectral dimension counts 3500 pixels, uniformly sampled from 4.82 to 28.5 μm with a step size $T_l = 3\,10^{-3}\,\mu$m. To certify the performance of the reconstruction algorithm, we also test it on another synthetic object called "Urban"[3], denoted obj_2. Compared to obj_1, the spatial distribution of obj_2 is more complex and includes small scale details with more discontinuities, illustrated in Fig. 4.7. The spatial size and sampling are similar to obj_1, and the spectral dimension counts 2000 pixels uniformly sampled from 7.42 to 18 μm with a step size $T_l = 5\,10^{-3}\,\mu$m.

Ch.	Spectral range (μm)	FOV (pixels)	Slit width (arcsec)	Slit number	$T_{i'}$ (arcsec)	$T_{l'}$ (μm)	I' pixels	L' pixels	R
1	4.9 – 7.7	34×42	$2 \times T_j$	21	$2 \times T_i$	$4\,10^{-3}$	17	750	867
2	7.4 – 11.7	42×51	$3 \times T_j$	17	$2 \times T_i$	$6\,10^{-3}$	21	750	760
3	11.5 – 18.1	57×64	$4 \times T_j$	16	$3 \times T_i$	$9\,10^{-3}$	19	750	596
4	17.7 – 28.5	72×72	$5 \times T_j$	12	$3 \times T_i$	$1.6\,10^{-2}$	24	750	410

Table 4.1: Characteristics specific to the four spectral channels of the IFS instrument considered in this work.

4.4.2 Simulation of 2D multi-frame measurements

The developed forward model imposes several spectral and spatial FOV selections. Therefore, obj_1 is divided into four distinct spectral channels (Channels 1 to 4). Each channel ensures a unique spectral coverage, spatial FOV, slit width imposed by the j-width of the window w_c, and slit number (see Table. 4.1). On the other hand, obj_2 is divided into two distinct spectral channels that correspond to the second and third channels. Finally, to allow multi-frame observations, the acquisition system provides multiple observations of the same object, with a dithering pattern of 8 pointing directions.

[3] taken from http://lesun.weebly.com/hyperspectral-data-set.html

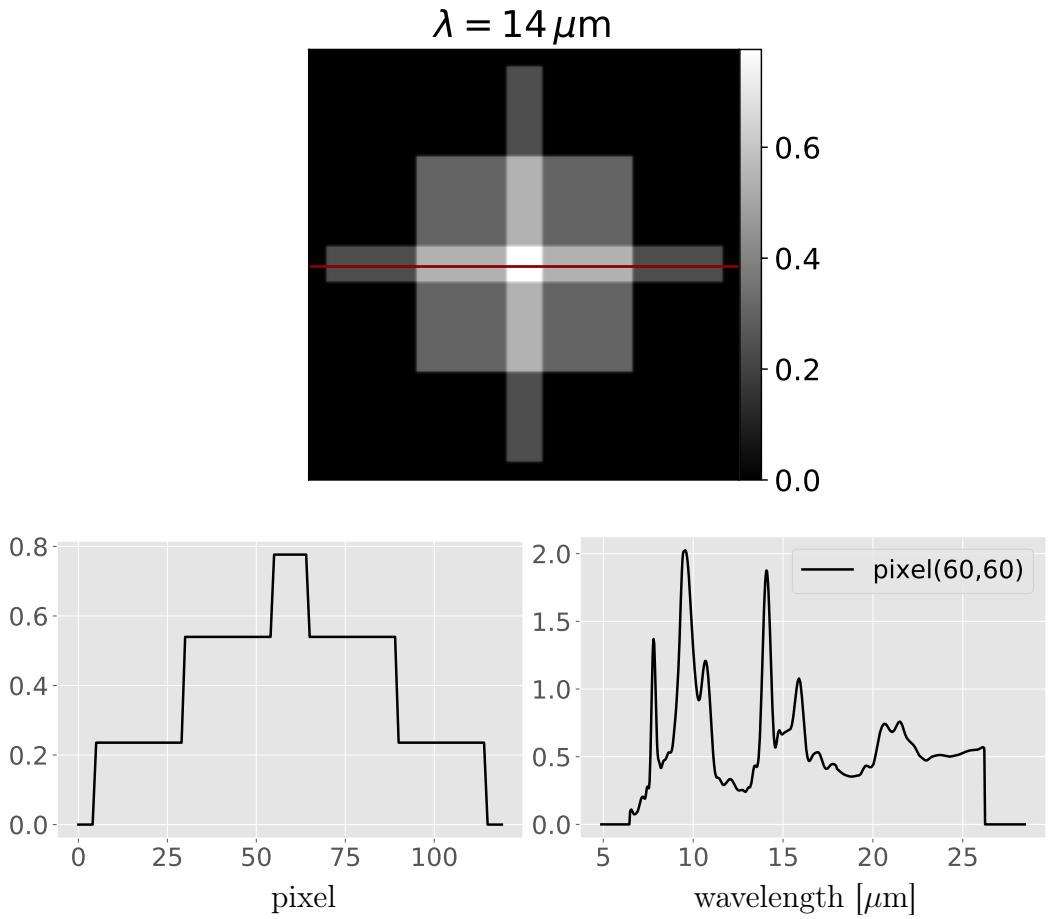

Figure 4.6: (Top): illustration of a monochromatic image at $\lambda = 14\,\mu$m for obj_1. (Left): the spatial distribution of the central row (red line) of the monochromatic image. (Right): Spectral distribution located at the center of the monochromatic image.

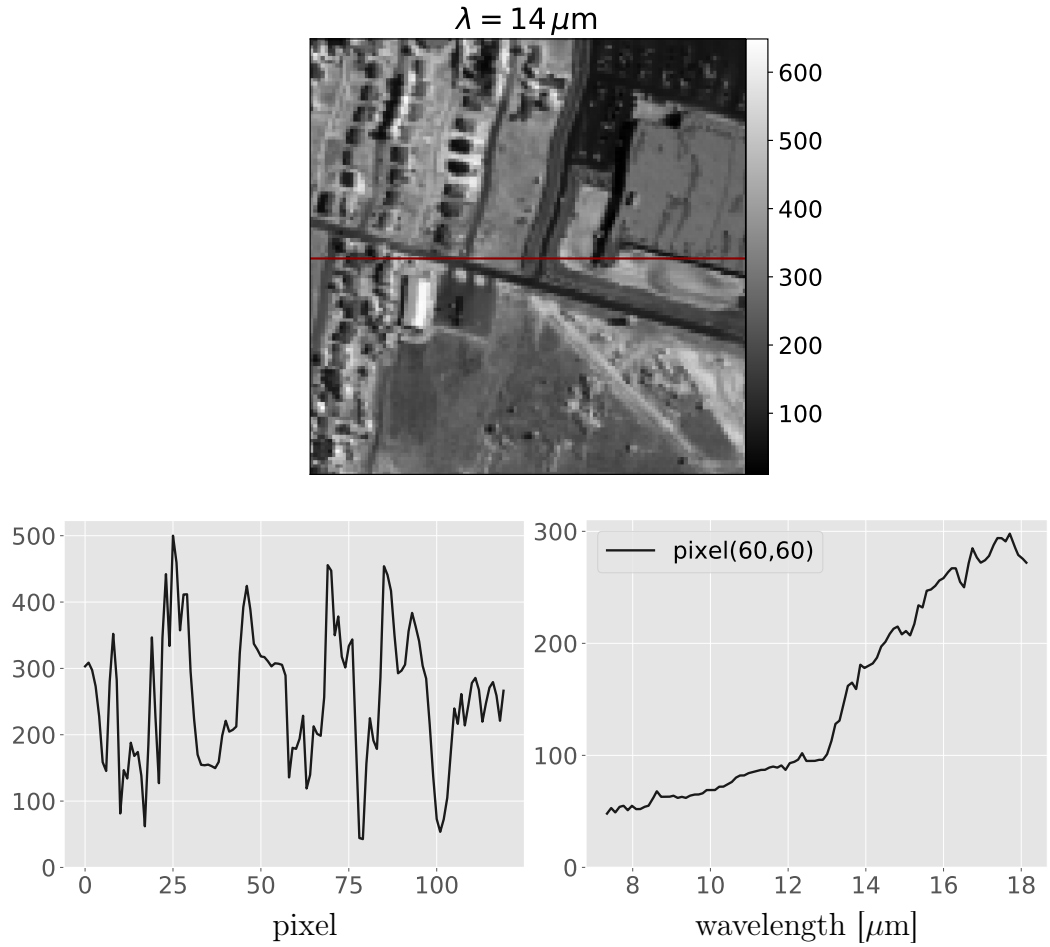

Figure 4.7: (Top): illustration of a monochromatic image at $\lambda = 14\,\mu$m for obj_2. (Left): the spatial distribution of the central row (red line) of the monochromatic image. (Right): Spectral distribution located at the center of the monochromatic image.

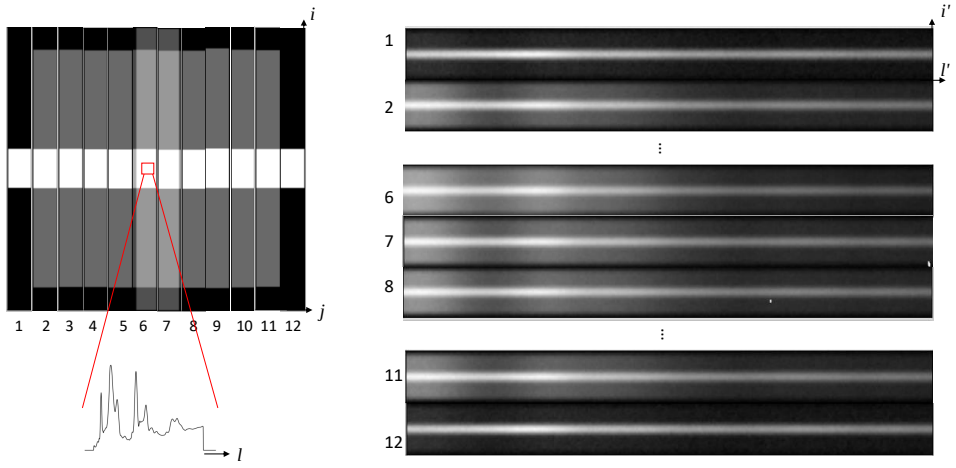

Figure 4.8: (Left): 12 adjacent spatio-spectral cubes $\boldsymbol{x}_c[i, j, l]$ for a particular pointing p, belonging the fourth channel of obj_1. (Right): Blurred, diffracted and sampled 2D measurements $y_c[i', l']$.

For a particular pointing p, the light inside each spatio-spectral selection $\boldsymbol{x}_c[i, j, l]$ is diffracted and projected onto 2D detectors, resulting in 2D measurements $\boldsymbol{y}_c[i', l']$. In addition, the spectral resolution R and the spatial and spectral sampling of the measurements changes depending on the selected channel. The step size of the detector imposes the spatial sampling of the measurements $T_{i'}$. Moreover, the MRS instrument has large detectors. Thus, to reduce the computational cost of the problem, we assume here that the spectral sampling of the measurements $T_{l'} = 4 \times T_{l'}^{\text{MRS}}$ and $R = R^{\text{MRS}}/4$ where $T_{l'}^{MRS}$ and R^{MRS} are the spectral sampling and the spectral resolution of the actual MRS instrument (see [Wells 2015]). Table 4.1 provides the spectral resolution R, the spatial sampling $T_{i'}$ and the spectral sampling $T_{l'}$ considered in the work, along with the size in pixels of the acquired measurements (I', L') for each channel.

Finally, the measurements calculated with Eq. (4.10) are corrupted with an additive zero-mean white Gaussian noise with an SNR of 30 dB, computed as

$$\text{SNR}_c\,(\text{dB}) = 10 \times \log_{10} \frac{\|\boldsymbol{y}_c\|_2^2}{N_c \times \sigma_n^2}. \tag{4.28}$$

N_c is the total pixel number of the output for a particular channel, and σ_n the standard deviation of the noise.

We show in Fig. 4.8 a set of noisy, blurred and sampled 2D measurements, for obj_1. These measurements belong to the fourth spectral channel for a fixed pointing p. Similarly, we show in Fig. 4.9 the acquired measurements form the third channel of obj_2.

Given the measurements, our proposed SR reconstruction algorithm, developed in section 4.3.2, is applied to estimate the unknown 2D+λ input image. To complement our results, we compare our algorithm to the shift-and-add (S&A) algorithm,

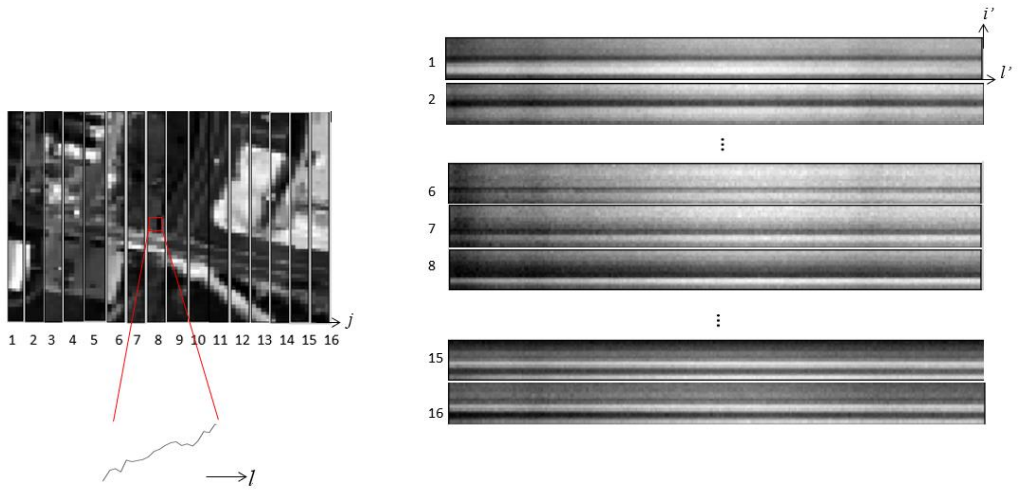

Figure 4.9: (Left): 16 adjacent spatio-spectral cubes $\boldsymbol{x}_c[i,j,l]$ for a particular pointing p, belonging the third channel of obj_2. (Right): Blurred, diffracted and sampled 2D measurements $y_c[i',l']$.

detailed in section 4.3.1. However, as the latter does not consider the blurring effects, we enforce a Total variation (TV) regularization after the S&A step, that performs spatial deconvolution separately for each wavelength writing

$$\hat{\boldsymbol{x}}^{l'}_{\mathrm{SA}} = \arg\min_{\boldsymbol{x}} \|\boldsymbol{y} - \boldsymbol{H}^{l'}\boldsymbol{x}^{l'}\|_2^2 + \mu|\nabla \boldsymbol{x}^{l'}|_1. \tag{4.29}$$

$\boldsymbol{H}^{l'}$ is a monochromatic spatial PSF at wavelength l' and $\nabla \boldsymbol{x}^{l'}$ computes the first-order difference of the image. We rely on the primal dual Chambolle-Pock algorithm [Chambolle 2011] to solve Eq. (4.29). Unlike our proposed method, the S&A algorithm followed by TV deconvolution at each wavelength does not allow data fusion. Finally, we compare our algorithm to the classical l_2 regularization to showcase the importance of the convex edge-preserving regularization choice, particularly around sharp edges, with

$$\hat{\boldsymbol{x}}_{\mathrm{q}} = \arg\min_{\boldsymbol{x}} \|\boldsymbol{y} - \boldsymbol{H}\boldsymbol{x}\|^2 + \mu_{spat}\|\boldsymbol{V}_u\boldsymbol{x}\|^2 + \mu_{spec}\|\boldsymbol{V}_w\boldsymbol{x}\|^2 . \tag{4.30}$$

Since the unknown input is a high-dimensional image, Eq. (4.30) is solved iteratively using the conjugate gradient optimization algorithm (Algorithm 2), provided in section 2.1.3.

All the reconstruction algorithms are implemented in python with numpy toolbox and computed with a single CPU at 5GHz with 32 GB of memory, and tested with a number of iteration sufficient enough to ensure a convergence towards the solution, reported in Table 4.2[4]

[4]For the proposed algorithm with half quadratic approaches, the global number of iterations corresponds to the number of iterations for the conjugate gradient algorithm used to estimate $\hat{\boldsymbol{x}}^k_{hq}$ in Eq. (4.24) at the iteration k $\times$ the total number of iterations k.

	Size	Algorithm	Number of iterations	Time [minutes]
Obj_1	$120 \times 120 \times 3500$	Proposed	20×20	94
		l_2	400	75
		S&A + TV	400	52.5 (0.015 per λ)
Obj_2	$120 \times 120 \times 2000$	Proposed	20×20	50
		l_2	400	40
		S&A + TV	400	30 (0.015 per λ)

Table 4.2: Number of iterations and computational time of the iterative reconstruction algorithms.

4.4.3 Results and Discussion

Estimating the 2D+λ image $\boldsymbol{x}[i,j,l]$ relies on the totality of the blurred, sampled, and noisy measurements $\boldsymbol{y}$. We compare in the following the reconstructed spatial and spectral distributions obtained with the different reconstruction methods. We also display the normalised least square error, computed between the original $\boldsymbol{x}[i,j,l]$ and the estimated $\hat{\boldsymbol{x}}[i,j,l]$ object, for a particular wavelength, with

$$\text{Error} = \|\boldsymbol{x}^l[i,j] - \hat{\boldsymbol{x}}^l[i,j]\|_2 / \|\boldsymbol{x}^l[i,j]\|_2 \tag{4.31}$$

Spatial distribution: Comparisons between the original and the reconstructed 2D+λ images are shown for obj_1 at 6.5 ,9, 14 and 21 μm in Figs. 4.10, 4.11 and 4.14, and for obj_2 at 9 and 14 μm in Figs. 4.12 and 4.13, using the S&A, proposed, TV and l_2 algorithms.

For both objects, the proposed algorithm shows a good reconstruction with the smallest error values at all wavelengths. The spatial dynamic is fully restored, and the spatial resolution significantly improved.

The S&A algorithm succeeds at reconstructing large-scale patterns, but, due to blurring and noise, it fails to completely reconstruct small-scale structures, particularly for obj_2 as illustrated in Fig. 4.12. We also notice in Figs. 4.10 and 4.12 that the images reconstructed for both objects with the S&A algorithm are significantly more blurred at long wavelength than the small wavelength, and the errors higher. Such results are expected since the width of the spatial PSF increases linearly with the wavelength.

To highlight the importance of the convex edge-preserving regularization, we compare in Fig. 4.11 and 4.13 the spatial reconstruction with our algorithm to the S&A + TV algorithm (Eq. 4.29) and with the classic l_2 algorithm (Eq. 4.30). The S&A + TV shows better qualitative results with minor errors than the simple S&A

algorithm. However, this method does not outperform the proposed algorithm for both objects. For instance, at $\lambda = 9\,\mu$m, enforcing a TV regularization allows denoising and good restoration of the edge, but becomes less efficient at long wavelengths since the blur is important. In addition, the spatial reconstruction is not performed jointly for all spectral bands but separately. We also show the spatial reconstruction using the l_2 algorithm, which is performed jointly for all spectral bands and channels. It outperforms the S&A + TV algorithm, especially at long wavelengths, but not our algorithm since it fails to preserve the edges, as illustrated for obj_1 in Fig. 4.11 where the reconstructed edges are smoothed and present ringing artifacts.

Finally, to better showcase the performance of all algorithms on the reconstructed images, particularly around the edges, we show in Fig. 4.14 a plot of the spatial distribution at the central row of the reconstructed obj_1, at $\lambda = 6.5$ and $14\,\mu$m. The reconstruction with the proposed algorithm is the only one which restores the edges and the spatial dynamic at both wavelengths. Whereas the S&A algorithm fails to restore the edges because of the blurring. With the additional TV regularization, the edges are more preserved, particularly at small wavelengths but the spatial dynamic is not properly restored . On the other hand, the l_2 regularization succeeds in recovering the spatial dynamic, but with ringing artifacts, especially around the edges.

Spectral distribution: We display in Fig. 4.15 and 4.16 the original spectral distribution $\boldsymbol{x}$, the S&A solution $\hat{\boldsymbol{x}}_{S\&A}$, and the half-quadratic solution $\hat{\boldsymbol{x}}_{hq}$, for two selected pixels indicated in the legend for obj_1 and obj_2, respectively.

In Fig. 4.15 (left), the spectral distribution of the reconstructed 2D+λ image for obj_1 with both algorithms fits the original spectral distribution over the whole measured range (from 4.75 to 28.5 μm) because the chosen spatial position corresponds to a smooth region. Whereas in Fig. 4.15 (right), the spatial position is chosen in a region with high gradients. Here the spectral reconstruction using the proposed algorithm is significantly improved compared to the spectral reconstruction using the S&A algorithm. In fact, because of spatial filtering, different spectra from different neighboring spatial positions are mixed within a pixel. Since the S&A algorithm does not consider deconvolution, the spectral reconstruction cannot perfectly match the original spectral distribution. This problem is better illustrated in Figure 4.16 for the spectral reconstruction of obj_2 since the spatial distribution of the latter contains small-scale details with different spectral distributions between neighboring pixels. We show in Figure 4.16 (left) a spectral reconstruction for a spatial position located in a smooth region. The spectral reconstruction with the S&A algorithm is highly contaminated by the noise and fails to match the original distribution perfectly, however, the layout of the distribution is preserved. On the other hand, Figure 4.16 (right) shows that the spectral reconstruction with the S&A algorithm, at a spatial position located at high gradients, fails to preserve the layout of the original distribution since the spectra are highly mixed within a pixel. We also see that the proposed algorithm allows denoising.

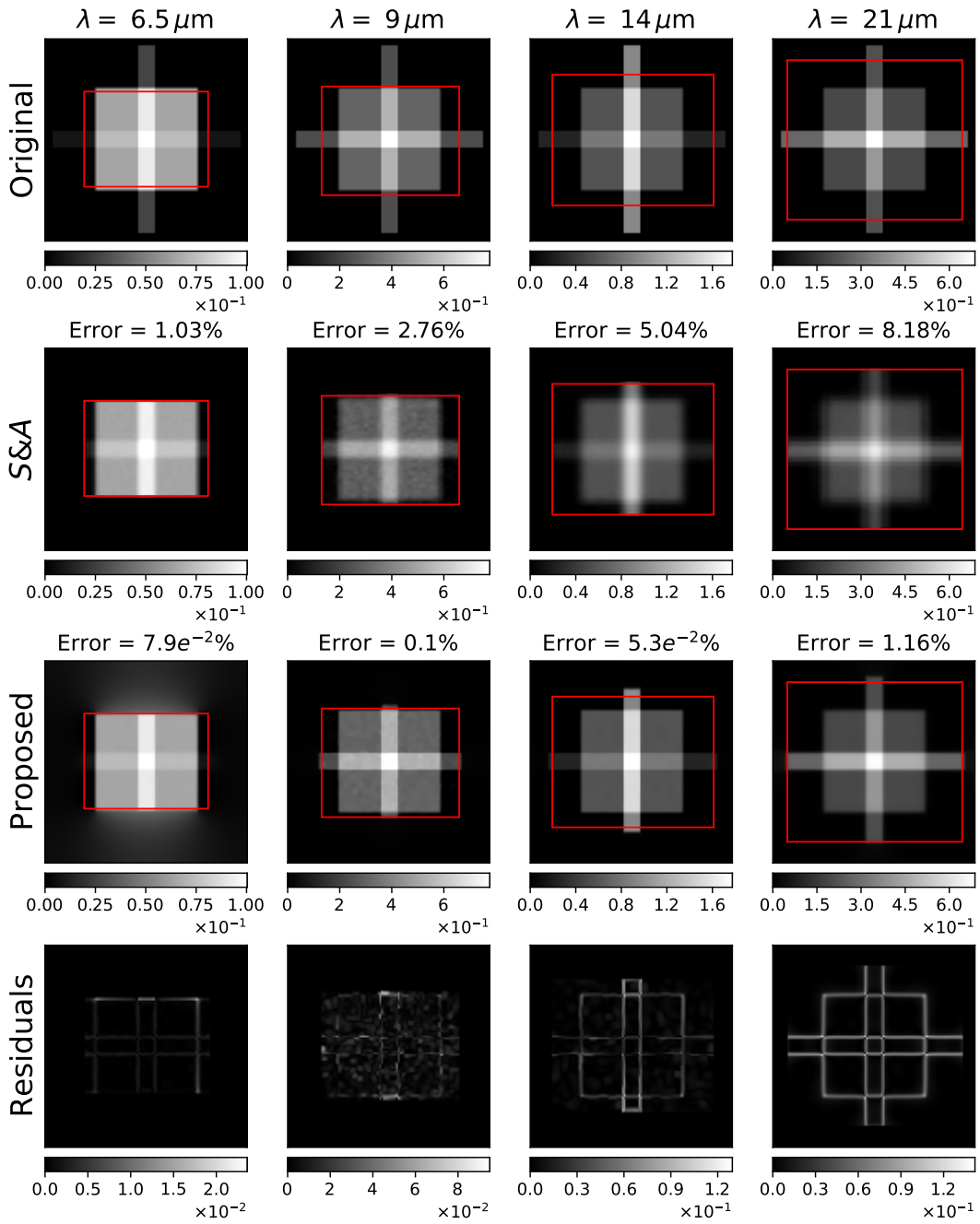

Figure 4.10: Spatial reconstruction for Obj_1 at 30dB: [1st row] Original images at 6.5, 9, 14 and 21 μm. [2nd row] Reconstruction with S&A. [3rd row] Proposed restoration. [4th row] Residuals between the proposed reconstruction and the original image.

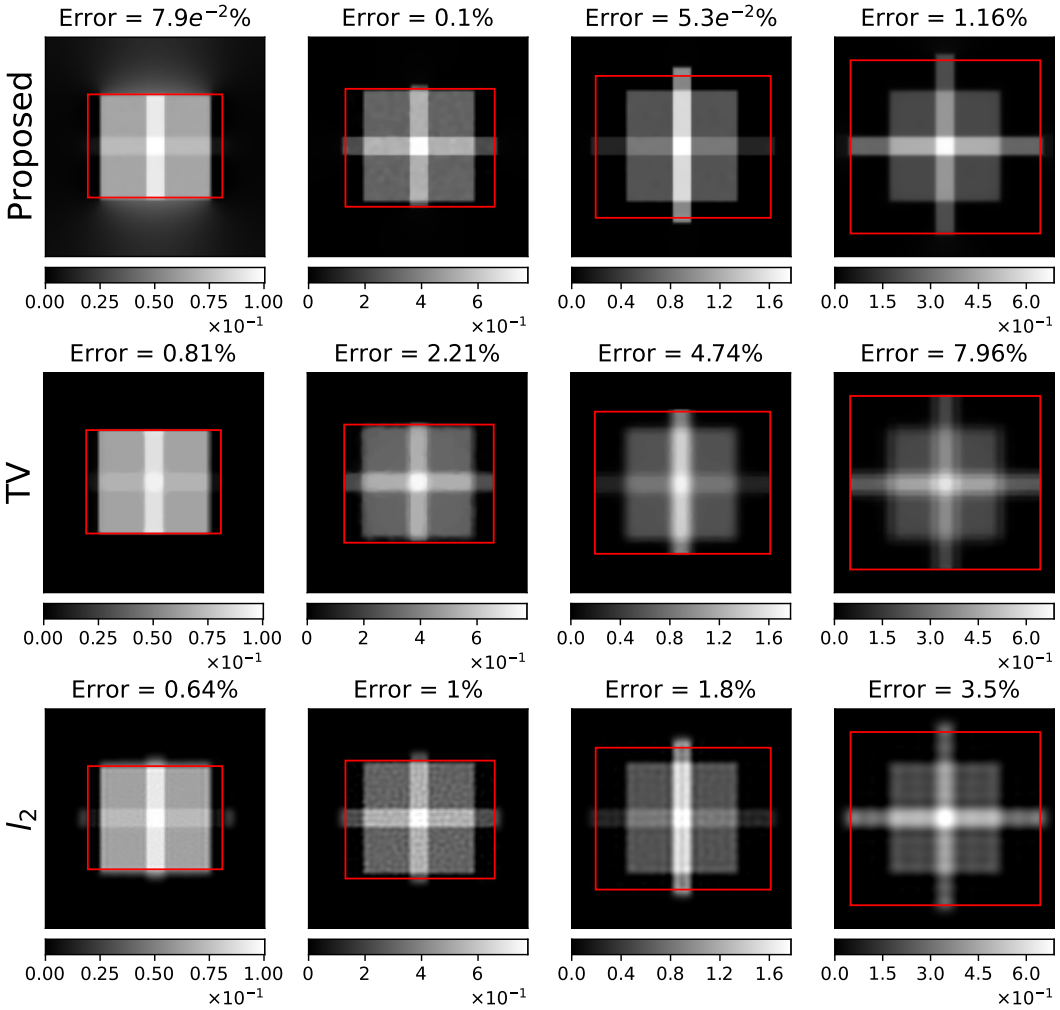

Figure 4.11: Spatial reconstruction for Obj_1 at 30dB: [1st row] Reconstruction with the proposed algorithm at 6.5, 9, 14 and 21 μm. [2nd row] Reconstruction with TV regularization. [3rd row] Reconstruction with l_2 regularization.

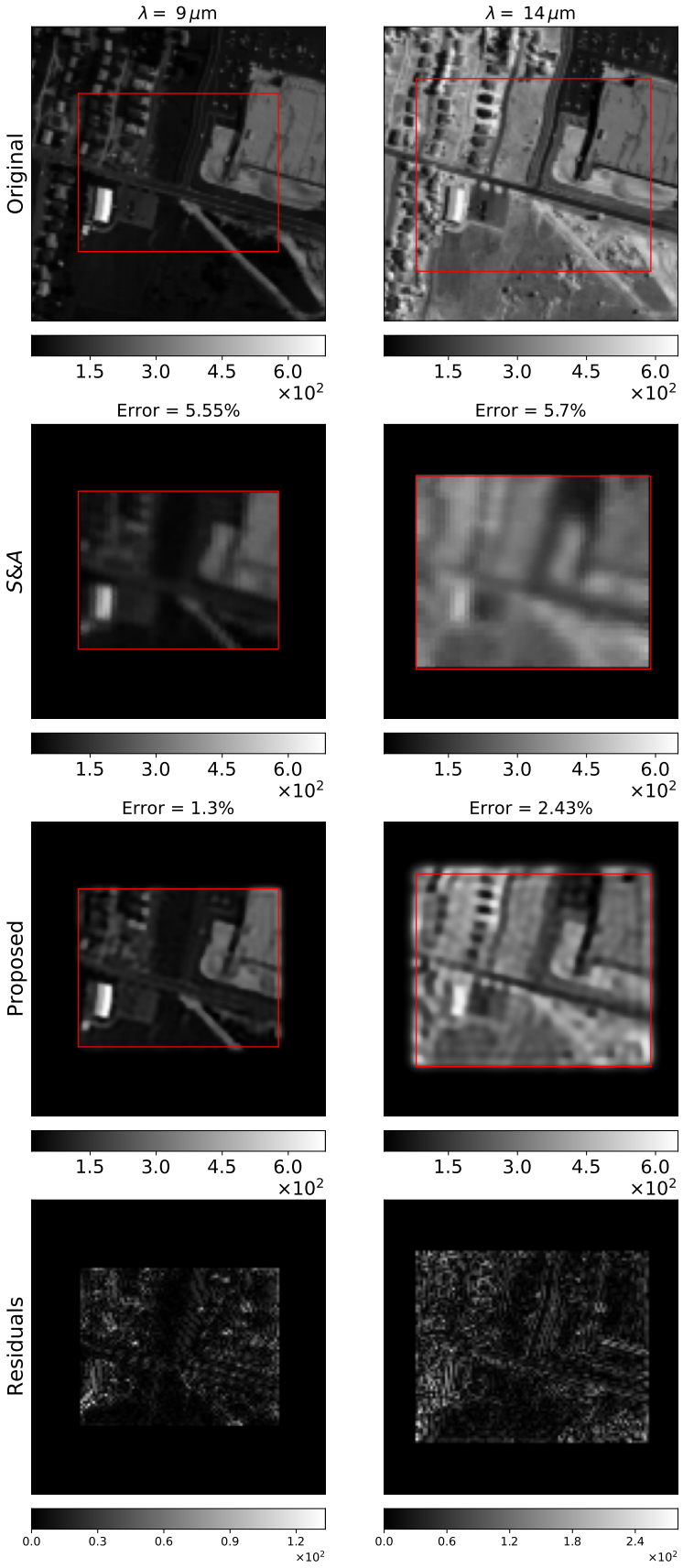

Figure 4.12: Spatial reconstruction for Obj_2 at 30dB: [1st row] Original images at 9 and 14 μm. [2nd row] Reconstruction with S&A. [3rd row] Proposed restoration. [4th row] Residuals between the proposed reconstruction and the original image.

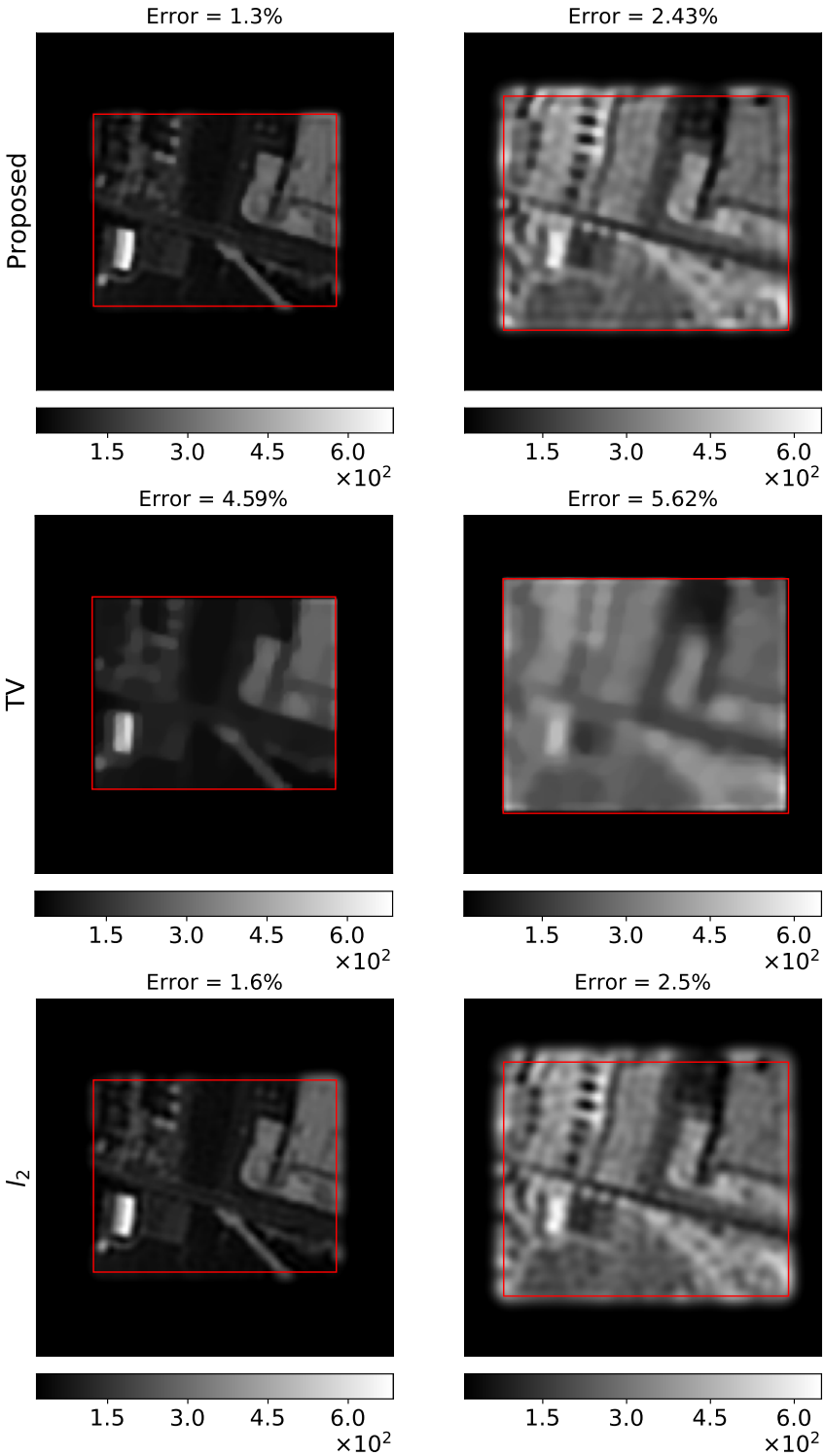

Figure 4.13: Spatial reconstruction for Obj_2 at 30dB: [1st row] Reconstruction with the proposed algorithm at 9, and 14 μm. [2nd row] Reconstruction with TV regularization. [3rd row] Reconstruction with l_2 regularization.

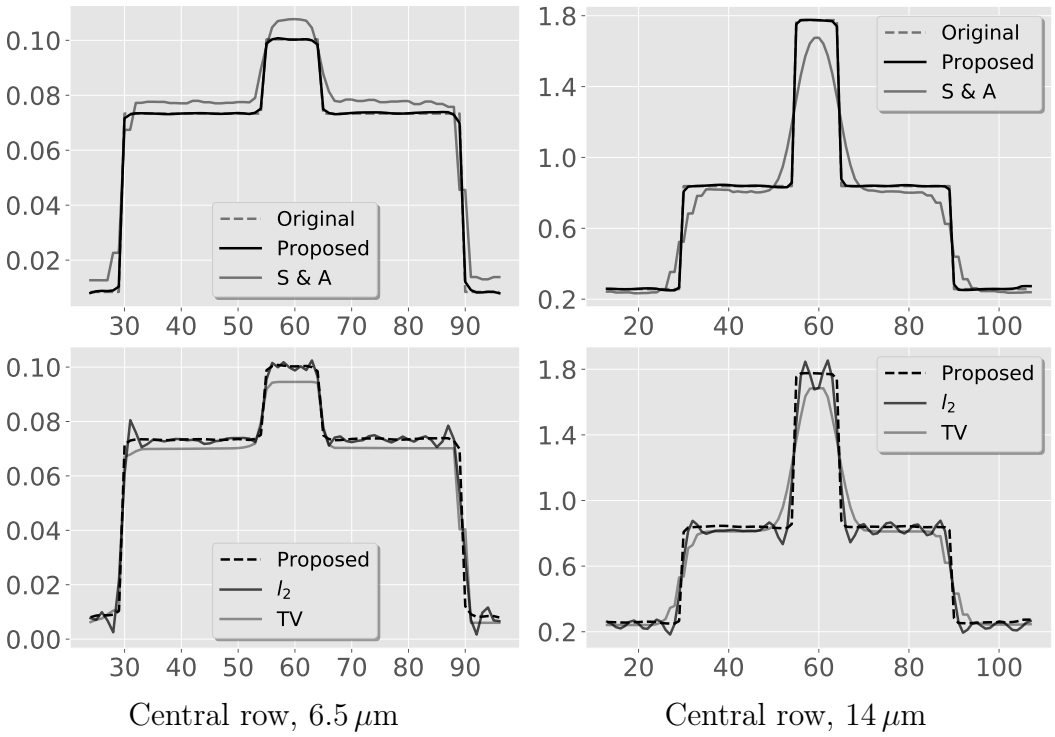

Figure 4.14: Spatial reconstruction of the central row for obj_1 at $\lambda = 6.5\,\mu$m (left) and $\lambda = 14\,\mu$m (right). The top panels show a comparison between the original spatial distribution and the reconstructed spatial distribution via the proposed and the S&A algorithm. The bottom panels show a comparison of the reconstructed spatial distribution with the proposed, TV and l_2 algorithms.

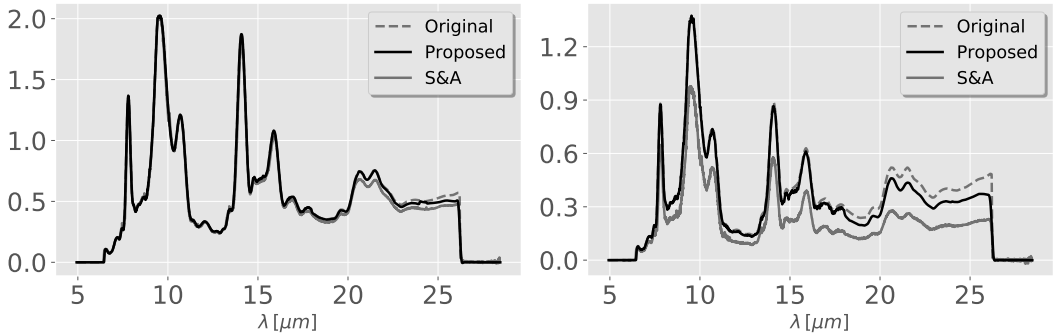

(a) Pixel (60,60) (b) Pixel (55,30)

Figure 4.15: Comparison of the spectral reconstruction for obj_1 with the S&A and proposed algorithms for the spatial position (60,60) located in a smooth region (left) and the spatial position (55,30) located in a region presenting high gradients (right).

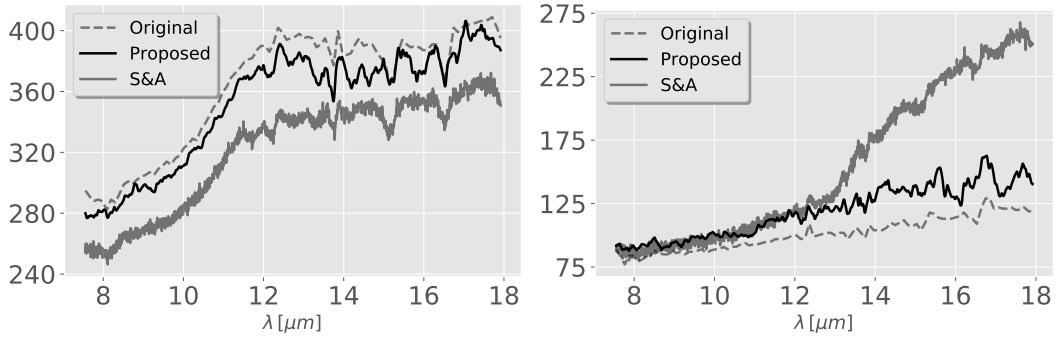

(a) Pixel (50,75) (b) Pixel (70,75)

Figure 4.16: Comparison of the spectral reconstruction for obj_2 with the S&A and proposed algorithms for the spatial position (50,75) located in a smooth region (left) and the spatial position (70,75) located in a region presenting high gradients (right).

4.4.4 Influence of the Regularization Parameters

Several parameters must be tuned to ensure the best reconstruction of the unknown 2D+λ image using the regularized least square approaches. The proposed algorithm is based on convex spatial and spectral regularization terms for edge-preserving (see 4.3.2). Consequently, we must determine four different parameters, which are the spatial and spectral regularization parameters μ_{spat} and μ_{spec}, and the spatial and spectral thresholds T_{spat} and T_{spec} that ensure denoising without excessive penalization of high gradient values of the solution.

We adopt a supervised strategy by testing different combinations of these parameters in a determined range, and keep the combination that minimizes at best the normalised least square error between the original and the estimated objects with

$$\text{Error} = \frac{\|\boldsymbol{x} - \hat{\boldsymbol{x}}\|^2}{\|\boldsymbol{x}\|^2}. \tag{4.32}$$

This approach is time-consuming, mainly because of the large number of hyper-parameters that needs to be tuned and also because the forward model is already computationally expensive. Therefore, we use high performance computing (HPC) resources from the "Mésocentre" computing center of CentraleSupélec and École Normale Supérieure Paris-Saclay supported by CNRS and Région Île-de-France [5].

We display in Fig. 4.17 (top) the computed errors after running the proposed reconstruction algorithm several times with different values of μ_{spat} and T_{spat} for a fixed μ_{spec} and T_{spec}, and then the other way around. This process was repeated two times to ensure a good convergence towards the correct combination of parameters. The hyper-parameters for obj_1 are finally set to $\mu_{spat} = 0.5$, $T_{spat} = 0.0005$ and $\mu_{spec} = T_{spec} = 0.1$, which correspond to the values minimizing the computed error (red circles on the top panels in Fig. 4.17). The reconstruction with the classical l_2 regularization requires two hyper-parameters to be tuned, and we have obtained $\mu_{spat} = 0.001$ and $\mu_{spec} = 0.5$, as shown in Fig. 4.17 (bottom).

The same tuning process is used for obj_2 to determine the hyper-parameters, with $\mu_{spat} = 0.001$, $T_{spat} = 20$, $\mu_{spec} = 0.5$, $T_{spec} = 25$ for the proposed algorithm, and with $\mu_{spat} = 0.001$ and $\mu_{spec} = 0.5$, as shown in Fig. 4.18

4.4.5 Source separation

In hyperspectral images, the spectral distribution between spatial pixels is often highly correlated at all wavelengths. Consequently, the HS image can be represented by a Linear Mixing Model (LMM) [Keshava 2002] with

$$\boldsymbol{x}[i,j,l] = \sum_{m=1}^{M} \boldsymbol{a}_m[i,j] \times \mathbf{s}_m[l]. \tag{4.33}$$

For all spatial coordinates (i,j), the object writes as a linear combination of M spectral components $\mathbf{s}_m$ where $M \ll L$. This dimension reduction is used for

[5] http://mesocentre.centralesupelec.fr

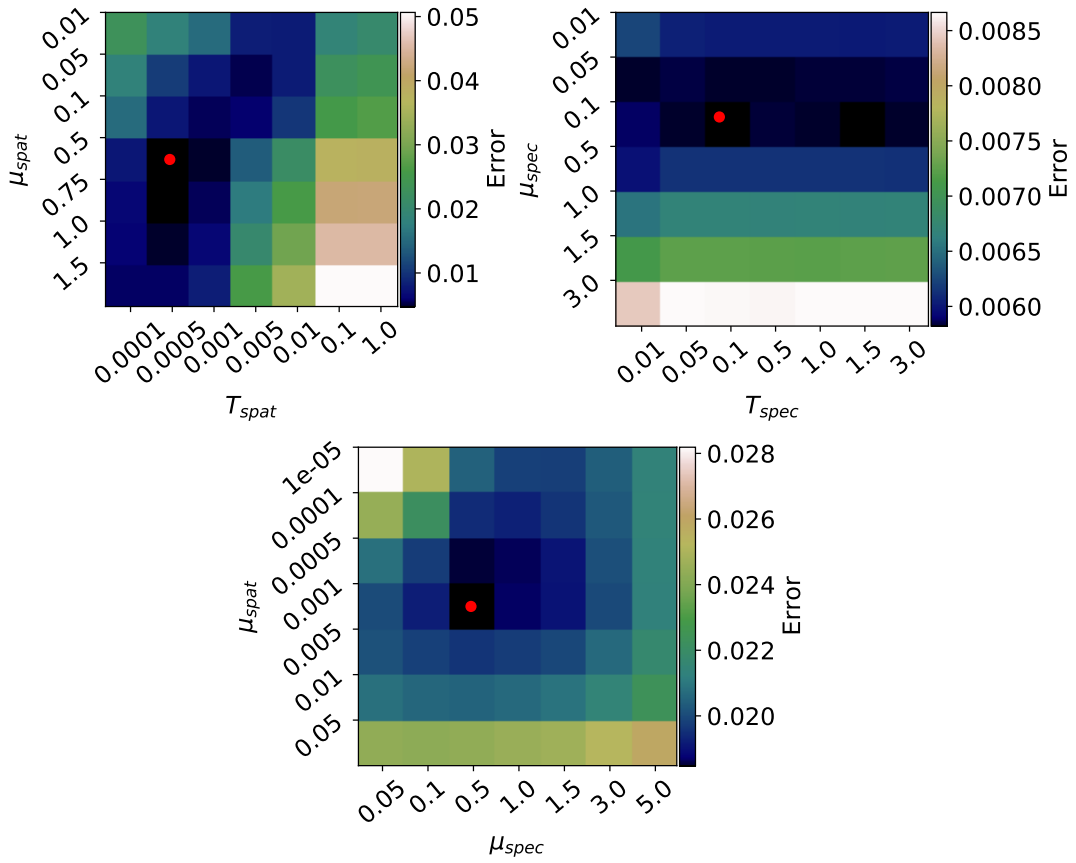

Figure 4.17: Influence of the hyper-parameters on the proposed algorithm (top images) and on the l_2 algorithm (bottom image) for obj_1.

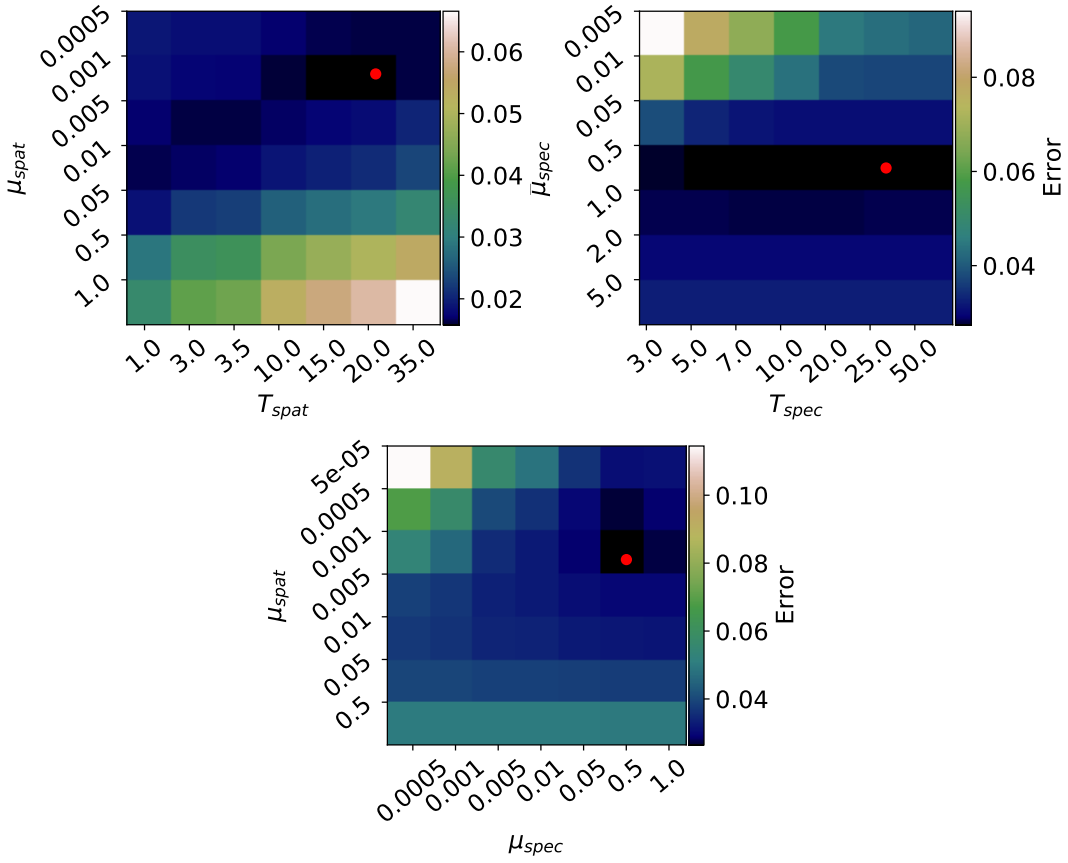

Figure 4.18: Influence of the hyper-parameters on the proposed algorithm (top figure) and on the l_2 algorithm (bottom image) for obj_2

a wide range of applications [Bioucas-Dias 2012] and can be achieved using several source separation techniques, in particular the principle components analysis (PCA) [Zhang 2012] and the non-negative matrix factorization [Lee 1999] that forces a non-negative constraint to the spectral components and the mixing coefficients.

As mentioned earlier, the non-stationary blurring, introduced by the spatial PSF, leads to mixed spectra within a spatial pixel. This section seeks to showcase the effect of this blurring on the M extracted spectral components. Obj_2 is a perfect candidate for such analysis since it contains small spatial details with different spectral distributions. Hence, we perform a PCA and NMF on the original obj_2 and the estimated $\hat{obj}_2$ using the S&A and the proposed algorithms. The first three spectral components which are extracted with PCA and NMF algorithms are shown in Fig. 4.19 and Fig. 4.20, respectively. We see with both source separation techniques that the proposed algorithm provides the most accurate spectral components compared to the original ones, mainly because our algorithm performs spectral unmixing via deconvolution and super-resolution. On the other hand, the S&A algorithm provides spectral components that does not match the original ones. Such results could be predicted because the spectral distribution of reconstructed object is highly mixed, mainly in high gradient regions. Finally, we also show in Fig. 4.19 and Fig. 4.20 the spectral components extracted from $\boldsymbol{x}_{opt}$, that is the output of the forward model considering only the spatial filtering to visualize the effect of only the spatial blurring on the extracted components. We see that these extracted components are more accurate than those provided from the result of the S&A algorithm, since the spatial sampling of the former matches that of the input image. However, we can clearly visualize the inaccuracy of the extracted components compared to the original ones and the importance of the deconvolution step during the reconstruction process.

4.4.6 Influence of the noise

The measurements are corrupted with an additive white Gaussian noise. Through the whole reconstruction analysis in the previous sections, the SNR was fixed to 30 dB. However, we are interested in examining the influence of additive noise on the performance of the reconstruction algorithms. Therefore, we add different noise levels to the measurements acquired from the third channel of obj_1 (see Table 3.1) by changing the SNR, and we test for each case the proposed, S&A and l_2 reconstruction algorithms.

We display in Fig. 4.21 the normalized least square error between the original object and the estimated object with the mentioned algorithms. The performance of all algorithms strongly depends on the noise level, with the error decreasing dramatically as the SNR increases (particularly for the S&A algorithm since it does not perform denoising). In any case, whatever the value of the SNR, the proposed algorithm always provides the smallest errors compared to the l_2 and S&A algorithms.

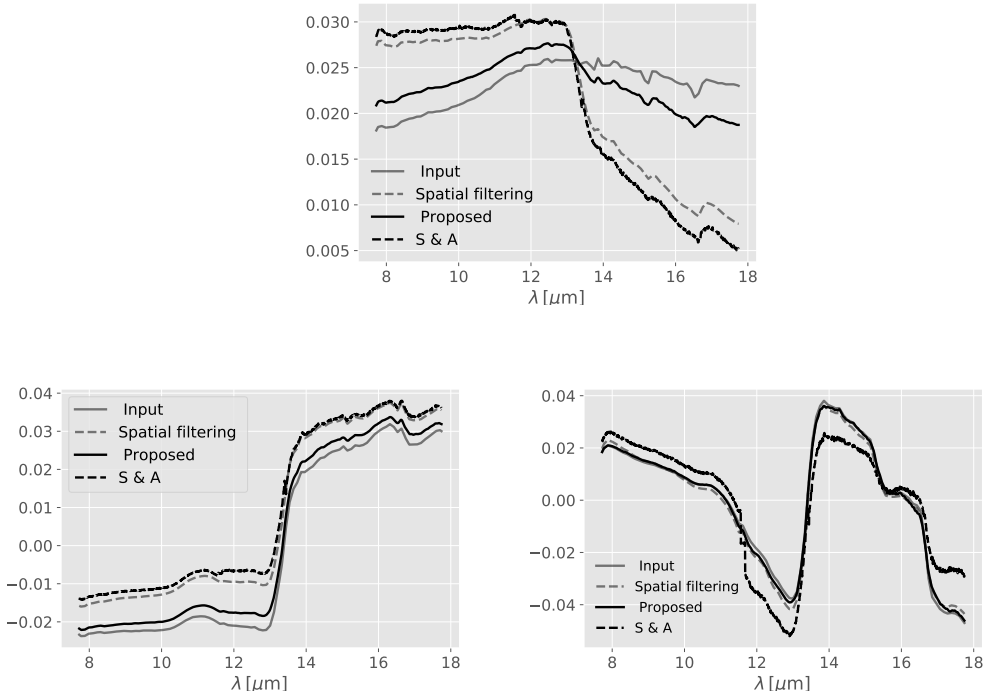

Figure 4.19: Spectral components resulted from a PCA applied on the original object, the spatially blurred object and the reconstructed object with S&A and the proposed algorithm for obj_2

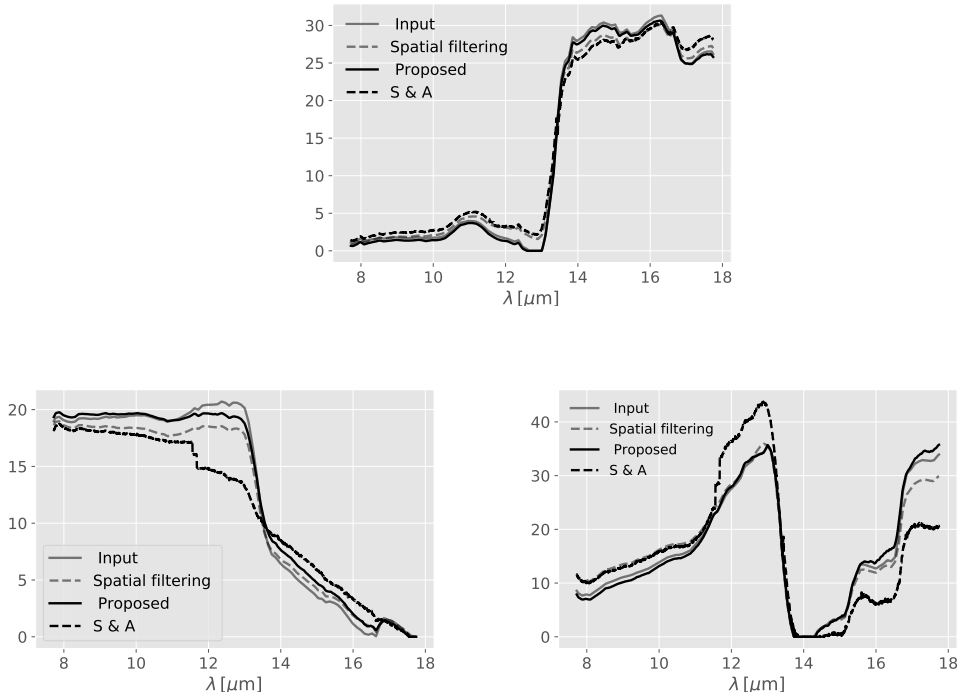

Figure 4.20: Spectral components resulted from a NMF applied on the original object, the spatially blurred object and the reconstructed object with S&A and the proposed algorithm for obj_2

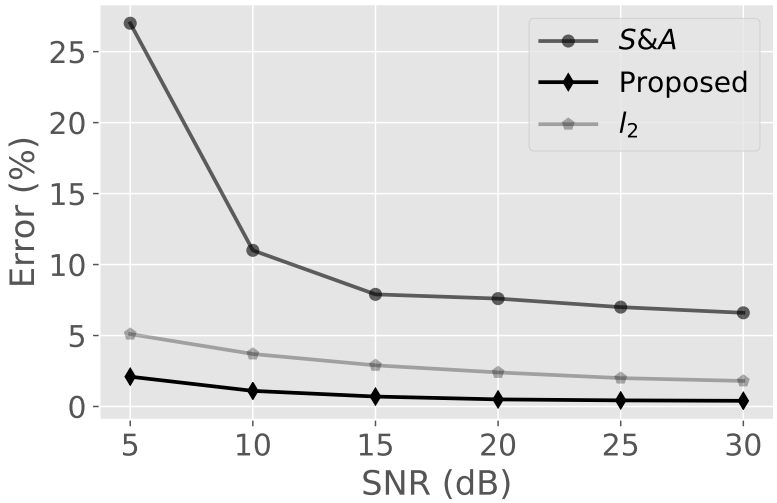

Figure 4.21: Influence of the noise level on the reconstruction of channel 3 for obj_1 with the proposed, l_2 and S&A algorithms.

4.4.7 Conclusion

This chapter presents a super-resolution (SR) reconstruction of a 2D+λ image from a set of 2D measurements that are spatially and spectrally degraded. The proposed approach relies on developing an explicit forward model of an IFS instrument, characterizing a relationship between the 3D input and the 2D measurements. This complex forward model takes into account (1) wavelength-dependent spatial and spectral blurring, (2) different observations coming from multiple sources with different spatial fields of view and spectral windows, and different pointings of the instrument, and (3) irregular spatial sampling at the detector. This model is primarily developed to simulate measurements for the Mid-Resolution Spectrometer of the Mid-Infrared Instrument on board the JWST. The proposed reconstruction algorithm is based on the regularized least square approaches with convex spatial and spectral half-quadratic regularizations in order to preserve high spatial and spectral gradients.

We have validated the performance of the proposed algorithm using two synthetic objects with complex spatial and spectral distributions. It shows a significant increase in the spatial and spectral resolution of the reconstructed object compared to other reconstruction algorithms, particularly the shift and add algorithm (S&A) followed by a TV deconvolution step and the classical l_2 algorithm. Even though our algorithm is computationally the most expensive, it outperformed the other reconstruction algorithms and provided the best qualitative results with an error less than 1.5% for obj_1 and 2.5% for obj_2 for an SNR = 30 dB at all wavelengths.

However, the proposed reconstruction algorithm presents limitations. First, the reconstructed HS images, measuring a broad spectral range in the infrared, are composed of several thousand spectral bands. Therefore, the number of unknowns to estimate is relatively significant, leading to an increase in the computational complexity of the reconstruction algorithm. Moreover, the proposed algorithm requires the determination of four hyperparameters (two for spatial and spectral regularizations and two thresholds for edge-preserving) to ensure the best reconstruction of the 3D object, which is a long process regarding the computational costs. Finally, the spectral information, particularly for astronomical observations, is very complex and also contains spectral rays, which can require, in some cases, different hyper-parameters for different types of spectral information.

In the following chapter, we present a new linear model of the 2D+λ input. In particular, we assume that $\boldsymbol{x}$ lives in a low dimensional subspace, and represented as a linear combination of a small number of spectral components $\mathbf{s}$, assumed known, and with unknown mixing coefficient $\boldsymbol{a}$. In that case, the number of the values to be estimated significantly decreases, and the proposed reconstruction algorithm requires only the determination of two spatial hyper-parameters. A spectral regularization is not required since the known spectral components impose the spectral resolution.

Chapter 5

Hyperspectral Reconstruction via Mixture coefficient estimation with Low-Rank Approximation

Contents

5.1 Introduction

In this work, we address the reconstruction problem of a 2D+λ image with high spatial and spectral resolutions from a set of 2D infrared measurements with high spectral resolution provided by the Integral Field Spectroscopy (IFS) of JWST/MIRI (see Chapter 3). In Chapter 4, we developed a forward model establishing a relationship between the unknown 2D+λ input image $\boldsymbol{x}$ and the set of 2D degraded measurements $\boldsymbol{y}$ and then used it for the reconstruction of $\boldsymbol{x}$.

In this chapter, we consider another linear model for the input image $\boldsymbol{x}$, assuming that the latter lives in a low dimensional subspace and can be expressed as a Linear

Mixing Model (LMM) writing

$$\boldsymbol{x}[i,j,l] = \sum_{m=1}^{M} \boldsymbol{a}_m[i,j] \times \mathbf{s}_m[l] \tag{5.1}$$

where for each spatial location (i,j), the spectral distribution of the 2D+λ input image is a linear combination of M spectral components $\mathbf{s}_m$, each weighted by a mixing coefficient $\boldsymbol{a}_m$. Choosing a LMM model for the input preserves the spatial and spectral distribution of $\boldsymbol{x}$. In addition, the number of the unknown that we want to estimate is reduced since we consider a low-rank approximation where $M \ll L$ (L denotes the number of the spectral bands). We also assume that $\mathbf{s}_m$ are known *a priori*, for instance, extracted from source separation algorithms such as the principal components analysis (PCA) [Jolliffe 2016], non-negative matrix factorization (NMF) [Lee 1999] and independent components analysis (ICA) [Hyvarinen 1999], or from existing spectral libraries [Zhao 2013]. Hence, the reconstruction of $\boldsymbol{x}$ relies on estimating the unknown mixing coefficients $\boldsymbol{a}$. Consequently, $\mathbf{s}_m$ in Eq. (5.1) can be included in the IFS forward model developed in Chapter 4 and provided in Eq. (4.10) on page 77. This combination between the LMM model of the input and the IFS forward model yields a new spectral dependent linear forward model that relates $\boldsymbol{y}$ to the unknown $\boldsymbol{a}$.

We propose a reconstruction method for the unknown $\boldsymbol{a}$ that uses the new spectral dependent forward model and relies on minimizing a regularized objective function with a convex spatial regularization for edge-preserving. Unlike the spatio-spectral reconstruction of $\boldsymbol{x}$ directly from the measurements $\boldsymbol{y}$ (see Chapter 4), the proposed reconstruction here is limited to the spatial estimation of $\boldsymbol{a}$ and requires only a spatial regularization. Consequently, the final reconstructed 3D image $\hat{\boldsymbol{x}}$ is a linear combination of the estimated coefficients $\hat{\boldsymbol{a}}$ and the known $\mathbf{s}$, where the latter imposes the spectral resolution of $\hat{\boldsymbol{x}}$.

We also relied in Chapter 4 on the fast half-quadratic algorithms with the Geman and Reynolds [Geman 1992] formulation to solve the reconstruction problem of $\boldsymbol{x}$. However, the computational cost of the reconstruction is significant since the forward model is already a computational burden. We rely in this Chapter on a more efficient optimization algorithm based on the Majorize-Minimize step and the subspace optimization [Chouzenoux 2011], in particular, the Majorize-Minimize Memory Gradient (3mg) [Chouzenoux 2011] [1].

This Chapter is organized following two main sections. In the first section, we explicitly include a publication submitted in "IEEE Transactions on Computational Imaging". It provides a detailed mathematical description of the new spectral dependent forward model and the proposed reconstruction algorithm. Since the new forward model depends on the IFS forward model provided in Chapter 4, the latter is also explicitly detailed in this publication. The performance of the reconstruction algorithm is validated using two synthetic 3D images with complex spatial and spectral distributions in the infrared range.

[1] `code available online https://github.com/forieux/qmm/`

In the second section, we use a synthetic 2D+λ image to provide a comparison between the spatio-spectral reconstruction algorithm of $\boldsymbol{x}$ directly from the measurements $\boldsymbol{y}$ (Chapter 4) and the reconstruction of $\boldsymbol{x}$ as a linear combination of the estimated mixing coefficients $\hat{\boldsymbol{a}}$ and the known $\mathbf{s}$. We use quality metrics such as the peak signal-to-noise ratio (PSNR), the Structural Similarity Index (SSIM) [Zhou Wang 2004], and the Spectral Angular Mapper (SAM) [Chein-I Chang 2000] to qualitatively compare the reconstructed spatial and spectral distributions with both reconstruction algorithms.

Super-Resolution Hyperspectral Reconstruction with Majorization-Minimization Algorithm and Low-Rank Approximation

Ralph Abi-Rizk, François Orieux and Alain Abergel

***Abstract*—Hyperspectral imaging (HSI) is extensively used in various applications. However, direct observation of these 3D spatio-spectral images is not possible since the real measurements are 2D. Moreover, the measurements suffer from spatial and spectral limitations, such as wavelength-dependent spatial and spectral blurring, projection onto multiple 2D detectors with different spatial sampling steps, spectral coverage, and spatial fields of view.**

We develop an explicit forward model based on the integral field spectroscopy that establishes a relationship between multiple HSI observations, assumed living in a low-dimensional subspace with known spectral components, and the measurements projected onto different 2D detectors while considering the spatio-spectral limitations. To address this ill-posed problem, we propose a multi-frame "Super-Resolution" algorithm, based on the regularized least square approach, with a convex edge-preserving regularization that allows spatial enhancements via multi-frame observations and deconvolution while preventing spectral distortions thanks to the known spectral components. The proposed algorithm is solved via the majorize-minimize memory gradient (3MG) optimization and tested on synthetic 3D input images, measuring in the Infra-Red range, hence, suitable for the upcoming Infrared Instrument onboard the James Webb Space Telescope (JWST). We show that the reconstruction with the proposed algorithm shows good performance compared to the state-of-art algorithm.

***Index Terms*—Inverse Problems - Super Resolution - Hyperspectral Imaging - Deconvolution - Spectral unmixing**

I. Introduction

HYPERSPECTRAL imaging (HSI) simultaneously collects high-resolution spectra at different spatial locations. It is wildly used for remote sensing applications in numerous domains such as in astrophysics [1], fluorescence microscopy [2], military [3], medical diagnosis [4], and others. HSI products are 3-dimensional (3D) images (i, j, l) where (i, j) are the two spatial dimensions and l the spectral dimension. Unfortunately, direct observations of hyperspectral (HS) images are not straightforward because 3D detectors do not exist. Instead, HS instruments, primarily relying on dispersive spectrometers, are designed to acquire measurements projected onto 2D detectors. In particular, HS instruments based on Integral-Field Spectrometers (IFS) [5] simultaneously observe the field of view (FOV) of the 3D input image through several thin slits in parallel. The dispersed wavelength from each slit is then projected onto 2D detectors, spanning a spatial dimension along one axis and a spectral dimension along the other axis. Consequently, a reconstruction stage is required to estimate the 3D input image from the collected 2D measurements. Although having a high spectral resolution, the 2D measurements suffer from spatial and spectral limitations during the acquisition process, such as blurring, sampling, and noise. First, because of the diffraction [6], the optical response known as the Point Spread function (PSF) introduces a wavelength-dependent spatial blurring. Second, the response of the dispersing system introduces a spectral blurring, which is also wavelength-dependent [7]. Finally, the spatial sampling on the detector is often insufficient at all wavelengths. To enhance the spatial resolution lost at the detector, a "dithering" method is considered [8], [9], consisting of observing the same scene multiple times by slightly shifting the measuring instrument. The resulted multi-frame measurements lead to a Super Resolution (SR) problem [10].

Several multi-frame SR algorithms have been addressed to reconstruct a discrete 3D input image from a set of measurements degraded by the HS instrument. The state-of-art approach for multi-frame SR 3D reconstruction is based on the shift and addition (S&A) method [8], [11]. It consists of merging the overall sampled and aliased measurements to provide a single reconstructed 3D image with an enhanced spatial resolution. Even though the S&A provides fast and non-iterative algorithms, it does not consider spatial and spectral blurring. Hence, it can be followed by a deblurring step, such as a Total Variation (TV) regularization [12]. This technique is efficient for reconstructing monochromatic images, but not for HS images since the deblurring step treats the spatial and spectral dimensions separately without considering the correlations between spectral bands.

Multi-frame SR reconstruction algorithms for HS images have also been treated as an inverse problem allowing a joint process of the spatial and spectral information from all the measurements. Such approaches rely on an explicit forward model that considers the limitations of the HS instrument and some additional priors about the 3D input image [13], [14]. Moreover, most of these approaches assume a low-rank structure, where the input is represented with a small number of spectral components. For instance, [13] developed a forward model that simulates optically blurred, sampled,

R. Abi-Rizk and F. Orieux are at the Laboratoire des Signaux et Systèmes (L2S), Université Paris-Saclay, CNRS, CentraleSupélec, 3 rue Joliot-Curie, 91 190 Gif-Sur-Yvette, France, e-mail: *ralph.abirizk@centralesupelec.fr*

A. Abergel is at the Institut d'Astrophysique Spatiale, Université Paris-Saclay, CNRS, 91405 Orsay, France

This project is funded by CNES. This work was performed using HPC resources from the "Mésocentre" computing center of CentraleSupélec and École Normale Supérieure Paris-Saclay supported by CNRS and Région Île-de-France (http://mesocentre.centralesupelec.fr/)

and aliased HS multi-frame measurements. They proposed a SR reconstruction algorithm based on the projection onto convex sets (POCS) method [15] that relies on the forward model to restore the observed HS image, approximated in the low-dimensional subspace. [14] handled the multi-frame SR reconstruction in the principal component analysis (PCA) domain. They used the first few principal components [16] to estimate motion and to reconstruct the 3D input image via the maximum a posteriori (MAP) [17]. However, these works do not consider wavelength-dependent spatial blurring.

Another solution for the spatial resolution enhancement is to perform a fusion of spatially sampled HS measurements with an auxiliary image of the same scene with high spatial resolution, if available, such as panchromatic (PAN) [18], or multispectral (MS) [1]. In particular, the HS-MS fusion has been excessively addressed in the inverse problem framework [1], [19], [20]. It relies on minimizing an objective function associated with two data fitting terms for HS and MS, respectively, and some priors about the 3D input image. [1] proposed an HS-MS fusion method while accounting for wavelength-dependent spatial blur. They provide fast algorithms in the Fourier domain while assuming a low-rank structure of the astronomical input image. However, the works proposed in [1], [13], [14] consider 3D measurements with a uniform spatial and spectral sampling steps, and without accounting for a wavelength-dependent spectral PSF.

We present in this work a complex forward model based on an IFS dedicated to astronomical observations in the infrared spectral range. It takes as input a 3D spatio-spectral image with a high resolution, approximated in a low-rank subspace, and simulates a set of multi-frame measurements projected onto different 2D detectors of different characteristics. The proposed model allows different input observations from different instruments like IFS and different pointings with the same instrument to perform multi-frame measurements. Moreover, it considers wavelength-dependent spatial and spectral blurring, as well as heterogeneous spatial and spectral sampling on the detectors. The proposed reconstruction method relies on the forward model and is based on the regularized least square approaches with convex edge-preserving regularization [21]. To solve the inversion problem, we choose the iterative Majorize-Minimize Memory Gradient (3MG) optimization algorithm [22] tested on two synthetic 3D input images with different spatial and spectral distributions. The results show significant improvement of the spatial and spectral resolutions comparing to the shift-and-add (S&A) algorithm [8], [11] followed by a spatial total variation (TV) regularization for each wavelength [12], and the classic l_2 regularization [23].

The paper is organized as follows. Section II discusses the proposed methodology, first for the instrument model developed for the IFS (Section II-A), and second for the forward model based on the linear mixing model (LMM) [24] (Section II-B). The SR multi-frame reconstruction algorithm is presented in Section III. In Section IV, we present the reconstruction results with the proposed algorithm and provide a comparison with other reconstruction algorithms. Finally, a conclusion is provided in Section V.

II. Forward Model for Heterogenous Hyperspectral Data Fusion

A. Observation Model

This section presents a new observation model of IFS instrument for spectral data fusion. It considers a series of components that modify and degrade the observed 3D input image (HS image) resulting in a set of blurred, truncated, and aliased 2D multi-frame measurements.

The original discretized input image is denoted $\boldsymbol{x}[i,j,l]$, with two spatial dimensions $(i,j) \in [1,\dots,I] \times [1,\dots,J]$ denoting the pixel index, and one spectral dimension $l \in [1,\dots,L]$. It is supposed uniformly sampled with spatial steps (T_i, T_j), and spectral step T_l.

1) Spatial Filtering: Because of the diffraction phenomenon [6], the observed 3D input is spatially blurred by the response of the optical system, also known as the point spread function (PSF). The PSF, denoted $\boldsymbol{h}$, is spectrally non-invariant, with an increasing blur as the wavelength increases. We suppose that the monochromatic PSF is known from simulations [25], calibration, or previous data processing steps. The PSF is assumed to be spatially stationary at all wavelengths. Thus, the spatial filtering is carried out by a 2D spatial convolution between the 3D input image and a discrete wavelength-dependent PSF, sampled with the same sampling step of the input, (T_i, T_j), writing

$$\boldsymbol{x}_{\text{opt}}[i,j,l] = \sum_{i',j'} \boldsymbol{x}[i',j',l]\boldsymbol{h}[i-i',j-j',l]. \tag{1}$$

We will see in the next section that the model includes spatially truncated observation, since the field of view of the IFS instrument is smaller than that of the 3D input image. Consequently, the spatial convolution is calculated using the spatial discrete Fourier transform for fast computation [26] without introducing periodic patterns to the blurred image.

2) Spatio-Spectral Field of View: We consider the spectral data fusion problem where the diffracted 3D image $\hat{\boldsymbol{x}}_{\text{opt}}$ is observed with (1) various spatial and spectral fields of view and (2) various pointings of the instrument.

First, the observations are grouped by spectral channels $c \in [1,\dots,C]$ with distinct physical properties. Each channel can possess different FOV, spectral range, and sampling step size. In addition, the IFS observes simultaneously the rectangular FOV of each channel through several slits in parallel. The number and size of the slits depend on the selected channel c. The spectral selection into channels and the spatial selection into slits with various widths and lengths result from a multiplication between $\boldsymbol{x}_{\text{opt}}$ and the channel windows $\boldsymbol{w}_c$ that writes

$$\boldsymbol{w}_c[i,j,l] \neq 0, \quad \forall (i,j,l) \in (\mathcal{I}_c, \mathcal{J}_c, \mathcal{L}_c), \tag{2}$$

with $(\mathcal{I}_c, \mathcal{J}_c, \mathcal{L}_c)$ a rectangular subset of $[1,\dots,I] \times [1,\dots,J] \times [1,\dots,L]$, and 0 otherwise. This hypothesis implies that all window sizes $(\Delta_{i,c}, \Delta_{j,c})$ are multiple of the step size of the 3D input image $\boldsymbol{x}$: $(\Delta_{i,c}, \Delta_{j,c}) = (n_c T_i, m_c T_j)$, with $(n_c, m_c) \in \mathbb{N}^2$. This is an approximation, minored if the steps are small.

Second, like in Multi-Frame Super-Resolution, observations can have different pointings (spatial shifts or dithering), indexed by p. These pointings can be shared between channels. We also consider that the pointing positions $(\Delta_{i,p}, \Delta_{j,p})$ are multiple of the sampling steps of $\boldsymbol{x}$: $(\Delta_{i,p}, \Delta_{j,p}) = (i_p T_i, j_p T_j)$, with $(i_p, j_p) \in \mathbb{N}^2$.

Finally, the spatio-spectral field of view for a particular pointing writes

$$\boldsymbol{x}_{c,p}[i,j,l] = \boldsymbol{x}[i,j,l] \times \boldsymbol{w}_c[i - i_p, j - j_p, l]. \quad (3)$$

3) Spectral Blurring: The spatio-spectral cubes $\boldsymbol{x}_{c,p}[i,j,l]$ are projected onto 2D detectors, through diffraction gratings for instance. For a monochromatic punctual source entering the grating at the wavelength $\lambda = lT_l$ from the particular channel c and the pointing p, the spectral response writes [7]

$$h_{c,j,p}(l',l) \propto \text{sinc}^2\left(\pi W\left(\frac{l'T_{l'} - q_{j,p}}{lT_l} - 1\right)\right), \quad (4)$$

where $\lambda' = l'T_{l'}$ is the spatial position on the detector (in wavelength unit) with a sampling step $T_{l'}$ and $q_{j,p} \in [-\Delta_{j,c}/2, \Delta_{j,c}/2]$ is the *relative* spatial position of the input source [1] determined by the spatial position j and the pointing p.

This spectral response is independent of the other spatial position indexed by i. Moreover, several particularities of the spectral response or, more generally the dispersion system, are inferred from Eq. (4). First, as illustrated in Fig. 1, the spatial position on the detector $\lambda' = l'T_{l'}$ of the spectral response depends on the wavelength input $\lambda = lT_l$. Second, the spectral response is *not stationary* and becomes broader with the increase of the wavelength. Finally, the relative spatial position $q_{j,p}$ alters the spatial position of the spectral response on the detector by shifting its maximum.

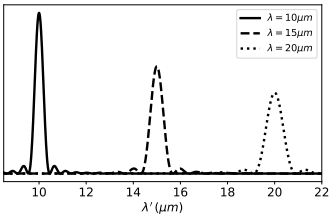

Fig. 1. The spatial position ($\lambda' = l'T_l'$) of the response on the detector depends on the input wavelength ($\lambda = lT_l$)

Eq. (4) depends also from the parameter W. It defines the width of the spectral response, which controls the spectral resolution. Assuming that the instrument is calibrated with a known spectral resolution $R = \lambda/\Delta\lambda$, with $\Delta\lambda$ the full width at half maximum (FWHM), basic calculus leads to $W \approx 2.8R/\pi$.

Finally, the grating is a non-stationary linear system. After discretization of the response, all individual sources $\boldsymbol{x}_{c,p}[i,j,l]$ contribute on the detector resulting in an output $\boldsymbol{g}_{c,p}$ of the dispersing system that writes

$$\boldsymbol{g}_{c,p}[i,j,l'] = \sum_{l \in \mathcal{L}_c} \boldsymbol{x}_{c,p}[i,j,l] \boldsymbol{h}_{c,j,p}[l',l] \quad (5)$$

[1] determined by the absolute position j and the pointing p.

with $l' \in \mathcal{L}'_c$ the wavelength index sampled on the detector and $\boldsymbol{h}_{c,j,p}[l',l]$ obtained from Eq. 4. Nevertheless, other models or calibrated measures than Eq. 4 may be used.

The model in Eq. (5) is not a convolution since it does not impose stationarity. Consequently, homogeneous spectral sampling is not required and can vary across the channels c. The spectral resolution of the output is therefore fixed by the spectral response and the sampled wavelength l'.

4) Detector Integration: The 3D spatially and spectrally blurred cube $\boldsymbol{g}_{c,p}[i,j,l']$ depends on the spatial index j whereas detectors are 2D. Since the system is linear, all the contribution of sources within the spatial window $\mathcal{J}_{c,p}$, determined by the channel c and pointing p, are summed on the detector. Consequently, without dithering and super-resolution, the j-width of the window $\boldsymbol{w}_c$ fix the spatial resolution along the j-axis of the measurements.

Moreover, the spatial sampling step T_i along the i-axis of the object $\boldsymbol{g}$ is different and smaller than the sampling step of the detector. Therefore, for all pointings p, we consider that the spatial sampling step $T_{i'}$ of the detectors for each channel c is a multiple $d_c \in \mathbb{N}$ of T_i with $T_{i'} = d_c T_i$, as in the classical image Super-Resolution [10]. Consequently, the 2D measurement $\boldsymbol{y}_{c,p}$ for a channel c and a pointing p writes

$$\boldsymbol{y}_{c,p}[i',l'] = \sum_{i=i'd_c}^{(i'+1)d_c} \sum_{j \in \mathcal{J}_{c,p}} \boldsymbol{g}_{c,p}[i,j,l'], \text{ with } i \in \mathcal{I}_{c,p}, \quad (6)$$

where i' and l' are the spatial and spectral indexes on the 2D detector, respectively. In practice, the summation along the i-axis is computed as a convolution between $\boldsymbol{g}$ and a square impulse response of size d_c, followed by subsampling every d_c elements.

To conclude, we developed a non-stationary but linear forward model involving relatively complex components that writes

$$\boldsymbol{y}_{c,p}[i',l'] = \sum_{i,j} \sum_{l \in \mathcal{L}_c} \left(\boldsymbol{x}[i,j,l] \underset{i,j}{*} \boldsymbol{h}[i,j,l]\right) \boldsymbol{w}_c[i - i_p, j - j_p, l] \times \boldsymbol{h}_{c,j,p}[l',l], \quad (7)$$

and accounts for several effects:

- 2D spatial convolutions with spectrally varying PSF described in Eq. (1) to model the optics,
- spatio-spectral windowing defined in Eq. (3) that models different spatial pointing, and different spatio-spectral selections,
- spectral blurring with a non-stationary response described in Eq. (5),
- and spatial and spectral sampling with specific steps for each detector which are larger than the sampling steps of the 3D input, described in Eq. (6).

The next section presents the combination of this observation model with a subspace representation of the 3D input image.

B. LMM forward model

1) Linear Mixing Model: Without additional information, the reconstruction of $\boldsymbol{x}$ corresponds to the estimation of

each voxel $\boldsymbol{x}[i,j,l]$ from the set of measurements $\{\boldsymbol{y}_{c,p}\}$ for all channels c and all pointings p. However, the spectral information contained in the 3D input images can be complex, with spectral rays, non-monochromatic spectral features and continuum. Moreover, this spectral information is generally highly correlated between spatial pixels over the whole measured spectral range. Thererfore, dimension reduction methods such as Principal Component Analysis (PCA) [16] or Non-negative Matrix Factorization (NMF) [27] can be very efficient on 3D images with high spectral resolution such as HS images.

Here we propose to write the unknown 3D image $\boldsymbol{x}$ using a Linear Mixing Model writing

$$\boldsymbol{x}[i,j,l] = \sum_{m=1}^{M} \boldsymbol{a}_m[i,j] \times \boldsymbol{s}_m[l] \tag{8}$$

where the spectral distribution at each spatial position (i,j) is a linear combination of M spectral components $\boldsymbol{s}_m$, known *a priori* or learned from the measurements, and unknown proportions $\boldsymbol{a}_m$. For our purposes, this is a subspace approximation as the number of spectral components M is much lower than the number of spectral bands L, as observed with dimension reduction methods[2]. For earth observation with segmentation problems, the spectral components $\boldsymbol{s}_m$ are pure spectra called end-members, and the $\boldsymbol{a}_m$ coefficients are called abundances [24]. In that case, additional constraints are usually imposed on $\boldsymbol{a}_m$ such as the non-negativity and sum-to-one constraints. This is not our case since we are only interested in the subspace approximation to reconstruct the original unknown 3D image $\boldsymbol{x}$, and not in the physical meaning of the spectral components $\boldsymbol{s}_m$.

The linear mixing model preserves the spatial and spectral distributions of the 3D input image and has many advantages

- The subspace approximation significantly reduces the number of unknowns that we want to estimate.
- As a consequence it is expected to increase the Signal-to-Noise (SNR) ratio on the reconstructed object.
- The reconstruction problem is limited to the estimation of the mixing coefficients $\boldsymbol{a}_m$, which requires only a spatial regularization to enhance the spatial resolution of the estimated 3D image.
- As the reconstruction of $\boldsymbol{x}$ is a linear combination of the estimated $\boldsymbol{a}_m$ and the known $\boldsymbol{s}_m$, the final spectral resolution of the reconstructed object is the spectral resolution of the spectral components $\mathbf{s}_m$,
- the spectral information is fully given regardless of the channel characteristics, while the spatio-spectral reconstruction of $\boldsymbol{x}$ directly from the measurements, without considering the mixing model, cannot exploit the complete spectral information at all spatial positions since the observation model (see section II-A2) considers different FOV depending on the channel.
- The estimated unknowns $\boldsymbol{a}_m$ depends solely on the spatial information. Hence, all spectral related terms (that depends on l and l') can be pre-computed.

[2]If $M \gg L$, the reconstruction problem with an overcomplete dictionary is considered, leading to variable selection methods, often done with sparsity, outside the scope of this work.

2) Final Forward Model: By combining the linear mixing model in Eq. (8) with the observation model in Eq. (7) we obtain

$$\boldsymbol{y}_{c,p}[i',l'] = \sum_{i,j} \sum_{l\in\mathcal{L}_c} \left(\left[\sum_{m=1}^{M} \boldsymbol{a}_m[i,j]\boldsymbol{s}_m[l] \right] \underset{i,j}{*} \boldsymbol{h}[i,j,l] \right) \boldsymbol{w}_c[i-i_p, j-j_p, l] \times \boldsymbol{h}_{c,j,p}[l',l]. \tag{9}$$

The above equation can be directly used to compute the forward output. However, since we want to estimate the mixing coefficients $\boldsymbol{a}_m$ and not the full 3D input image $\boldsymbol{x}$, the known spectral components $\boldsymbol{s}_m$ can be included in the observation model. Consequently, a new spectral dependent forward model is formulated that directly links the mixing coefficients to the measurements. For that purpose, all spectral operations related to l and l' can be combined and pre-computed.

First a spatial PSF cube *that depends on* m is computed for each spectral component with $\boldsymbol{h}_m[i,j,l] = \boldsymbol{s}_m[l]\boldsymbol{h}[i,j,l]$. The model then writes

$$\boldsymbol{y}_{c,p}[i',l'] = \sum_{i,j} \sum_{l\in\mathcal{L}_c} \left(\sum_{m=1}^{M} \boldsymbol{a}_m[i,j] \underset{i,j}{*} \boldsymbol{h}_m[i,j,l] \right) \boldsymbol{w}_c[i-i_p, j-j_p, l] \times \boldsymbol{h}_{c,j,p}[l',l]. \tag{10}$$

Second, the spectral blurring of $\boldsymbol{s}_m$ introduced by the spectral response $\boldsymbol{h}_{c,j,p}$ in Eq. (4) can be pre-computed with

$$\boldsymbol{h}_{m,c,j,p}[i,j,l'] = \sum_{l\in\mathcal{L}_c} \boldsymbol{s}_m[l]\boldsymbol{h}[i,j,l]\boldsymbol{w}_c[l]\boldsymbol{h}_{c,j,p}[l',l] \tag{11}$$

where $\boldsymbol{h}_{m,c,j,p}[i,j,l']$ is a spatio-spectral PSF cube that depends on the spectral template number m, the spectral window $\mathcal{L}_c$, and relative position j within the spatial window $\mathcal{J}_{c,p}$ (as described by Eq. (4)). Finally, the forward model writes

$$\boldsymbol{y}_{c,p}[i',l'] = \sum_{i} \sum_{j\in\mathcal{J}_{c,p}} \boldsymbol{w}_c[i-i_p, j-j_p] \left(\sum_{m=1}^{M} \boldsymbol{a}_m[i,j] \underset{i,j}{*} \boldsymbol{h}_{m,c,j,p}[i,j,l'] \right). \tag{12}$$

Compared to Eq. (9), the final forward model is relatively simplified with the following steps:

- First, the 2D mixing coefficients $\boldsymbol{a}_m$ are convoluted by a collection of 2D+λ PSF $\boldsymbol{h}_{m,c,j,p}$ that depends on the spectral component number m, the channel c, and the relative spatial position within the channel (j,p).
- After summation on m, the cube is spatially windowed for each pointing p.
- Then, the high-resolution window is spatially detector integrated (subsampled), resulting in 2D measurements $\boldsymbol{y}_{c,p}$ with a low spatial resolution.

3) Matrix Formulation: The model in Eq. (12) is linear and represents the overall multi-frame 2D measurements $\boldsymbol{y}_{c,p}$ in terms of the unknown mixing coefficients $\boldsymbol{a}$

$$\boldsymbol{y}_{c,p} = \boldsymbol{H}_{c,p}\boldsymbol{a} = \boldsymbol{\Sigma}_{i,j}\boldsymbol{W}_c\boldsymbol{\Sigma}_m\boldsymbol{C}_{m,c,j,p}\boldsymbol{a} \tag{13}$$

where $\boldsymbol{C}$ is a convolution operator, $\boldsymbol{\Sigma}_m$ a summation on the spectral template number m, $\boldsymbol{W}_c$ a windowing or raw selection and $\boldsymbol{\Sigma}_{i,j}$ a sum on i,j to model detector integration.

Consequently, the adjoint operator writes

$$\boldsymbol{e}_{c,p} = \boldsymbol{H}_{c,p}^t \boldsymbol{y}_{c,p} = \boldsymbol{C}_{m,c,j,p}^t \boldsymbol{\Sigma}_m^t \boldsymbol{W}_c^t \boldsymbol{\Sigma}_{i,j}^t \boldsymbol{y}_{c,p} \quad (14)$$

where $\boldsymbol{\Sigma}^t$ is a duplication operator, $\boldsymbol{W}_c^t$ a zero filling operator and $\boldsymbol{C}_{m,c,j,p}^t$ a convolution with flipped response.

The overall measurements writes

$$\boldsymbol{y} = \boldsymbol{H}\boldsymbol{a} = [\boldsymbol{H}_{0,0}^t, \ldots, \boldsymbol{H}_{C,P}^t]^t \boldsymbol{a} \quad (15)$$

and the full-adjoint operator writes

$$\boldsymbol{e} = \sum_{c,p} \boldsymbol{H}_{c,p}^t \boldsymbol{y}_{c,p} = \boldsymbol{H}^t \boldsymbol{y} \quad (16)$$

which is the sum of all retro-propagated measurements.

The next section describes the proposed reconstruction formalized as an inverse problem approach with efficient Quadratic Majorize-Minimize algorithm [22], [28].

III. Inverse problem

Our proposed new forward model combines multiple observations with a full complex linear model $\boldsymbol{y} = \boldsymbol{H}\boldsymbol{a}$. The operator $\boldsymbol{H}$ takes into account (1) spectral-dependent spatial blurring, (2) multiple channel observations with different fields of view, (3) spectral blurring, and (4) heterogeneous spatial and spectral samplings. Therefore, the reconstruction of the mixing coefficient $\boldsymbol{a}$ is an ill-posed inverse problem that includes data fusion, deconvolution, and multi-frame super-resolution steps.

A. Proposed reconstruction

We propose a new multi-frame SR algorithm that relies on the complete forward model in Eq. (12), with a reconstruction solution defined as the minimizer of an objective function combining a data fidelity term and a regularization term expressed as

$$\hat{\boldsymbol{a}} = \arg\min_{\boldsymbol{a}} \Big(\|\boldsymbol{y} - \boldsymbol{H}\boldsymbol{a}\|^2 + R(\boldsymbol{a}) \Big). \quad (17)$$

Many regularization methods and algorithms have been proposed in the literature. For instance, l_2 regularization [23] is the seminal approach with fast algorithms but fails to preserve the high gradient values of the solution. The Total Variation (TV) regularization [12] or dictionary-based approaches with sparsity constraints [29] have been broadly used but can introduce cartoon-like effects and provide relatively slow algorithms. More recently, prior learning from data with machine learning approaches [30] have been widely explored but require a lot of measurements to be competitive.

In this work, the major degradation effects of the forward model are the spectral-dependent spatial and spectral blurring. However, by choosing a linear mixing model with known spectral components $\boldsymbol{s}$, our reconstruction algorithm does not require spectral regularization. On the other hand, the spatial blurring is significant, especially at long wavelengths. Therefore, we propose a convex spatial regularization for edge-preserving. The objective function, denoted $J(\boldsymbol{a})$, writes

$$J(\boldsymbol{a}) = \|\boldsymbol{y} - \boldsymbol{H}\boldsymbol{a}\|^2 + \mu \sum_{c \in \mathcal{C}} \phi_c(\boldsymbol{v}_c^t \boldsymbol{a}) \quad (18)$$

where $\boldsymbol{v}_c$ are first order differences in the two spatial dimensions, μ is the spatial regularization parameter, and ϕ_c is a strictly differentiable convex potential. However, an explicit form of the minimizer $\hat{\boldsymbol{a}}$ of $J(\boldsymbol{a})$ is not available and cannot be directly calculated. In addition, the forward model is already computationally burden. Therefore, we must rely on highly effective optimization algorithms, as described in section III-C.

B. Half-Quadratic Algorithm

The objective function $J(\boldsymbol{a})$ is an instance of the more general criterion [21], [31] with:

$$J(\boldsymbol{a}) = \sum_q \mu_q \Psi_q(\boldsymbol{\mathcal{V}}_q \boldsymbol{a}_q - \boldsymbol{\omega}_q) \quad (19)$$

where $\boldsymbol{a}$ is the unknown, $\boldsymbol{\mathcal{V}}_q$ is a linear operator, $\boldsymbol{\omega}_q$ is a data fixed vector, μ_q are scalar hyper-parameters, and $\Psi_q(\boldsymbol{u}) = \sum_c \phi_q(u_c)$.

In addition, we suppose the following assumptions for the scalar function ϕ [22]:

1) $\mathcal{C}^1$, even, coercive,
2) $\phi(\sqrt{\cdot})$ is concave on $\mathbb{R}^+$,
3) and $0 < \dot{\phi}(u)/u < +\infty$, $\forall u \in \mathbb{R}$.

This objective function structure is chosen to allow efficient algorithms that use majorization with quadratic surrogate functions which write Q [32]

$$Q\left(\boldsymbol{a}, \boldsymbol{a}^k\right) = J\left(\boldsymbol{a}^k\right) + \nabla J\left(\boldsymbol{a}^k\right)^t \left(\boldsymbol{a} - \boldsymbol{a}^k\right) + \frac{1}{2}\left(\boldsymbol{a} - \boldsymbol{a}^k\right) \boldsymbol{A}^{(k)} \left(\boldsymbol{a} - \boldsymbol{a}^k\right) \quad (20)$$

where

$$\boldsymbol{A}^{(k)} = \sum_q \mu_q \boldsymbol{\mathcal{V}}_q^T \operatorname{diag}(\boldsymbol{b}_q^k) \boldsymbol{\mathcal{V}}_q$$

and

$$\boldsymbol{b}_q^k = \frac{\dot{\phi}(\boldsymbol{\mathcal{V}}_q \boldsymbol{x}^k - \boldsymbol{\omega}_q)}{\boldsymbol{\mathcal{V}}_q \boldsymbol{x}^k - \boldsymbol{\omega}_q}. \quad (21)$$

Lemma 3.1: [32] Let J be the objective function defined in Eq. (19) and $\boldsymbol{a}^k \in \mathbb{R}^N$. If the assumption holds, then the quadratic surrogate function Q in (20) is a tangent majorant for J at $\boldsymbol{a}^k$, for all $\boldsymbol{a} \in \mathbb{R}^N$,

$$\begin{cases} Q(\boldsymbol{a}, \boldsymbol{a}^k) \geq J(\boldsymbol{a}), \\ Q(\boldsymbol{a}^k, \boldsymbol{a}^k) = J(\boldsymbol{a}^k). \end{cases} \quad (22)$$

The proposed criterion in Eq. (18) is an instance of Eq. (19) with $q = \{1, 2\}$, $\mu_1 = 1$, $\Psi_1(\cdot) = \|\cdot\|^2$, $\boldsymbol{\omega}_1 = \boldsymbol{y}$, $\boldsymbol{\mathcal{V}}_1 = \boldsymbol{H}$, $\boldsymbol{\mathcal{V}}_2 = \boldsymbol{V} = [\boldsymbol{v}_1, \ldots, \boldsymbol{v}_{\mathcal{C}}]^t$. In previous work [33], we considered the half quadratic (HQ) strategy proposed by Geman and Reynolds (GR) [31] that defined an augmented objective function $J^*(\boldsymbol{a}, \boldsymbol{b})$, by using the quadratic surrogate function on all space $\mathbb{R}^N$ and the auxiliary variable $\boldsymbol{b}$ as

$$J^*(\boldsymbol{a}, \boldsymbol{b}) = \|\boldsymbol{y} - \boldsymbol{H}\boldsymbol{a}\|^2 + \frac{\mu}{2} \sum_{c \in \mathcal{C}} b_c (\boldsymbol{d}_c^t \boldsymbol{a})^2 + \psi(b_c) \quad (23)$$

where the function ψ is related to ϕ through convex duality.

The augmented objective function $J^*(\boldsymbol{a}, \boldsymbol{b})$ shares the same minimizer $J(\boldsymbol{a})$ with

$$\min_{\boldsymbol{b}} J^*(\boldsymbol{a}, \boldsymbol{b}) = J(\boldsymbol{a}).$$

The minimization of $J^*(\boldsymbol{a}, \boldsymbol{b})$ is quadratic with respect to (w.r.t) $\boldsymbol{a}$, and independent and explicit for each b_c [21]. HQ algorithm relies therefore on a two stages alternating the minimization process until convergence

$$\begin{cases} \boldsymbol{a}^k = \arg\min_{\boldsymbol{a}} J^*(\boldsymbol{a}, \boldsymbol{b}^{k-1}), \\ \boldsymbol{b}^k = \arg\min_{\boldsymbol{b}} J^*(\boldsymbol{a}^{k-1}, \boldsymbol{b}). \end{cases} \tag{24}$$

However the minimization w.r.t $\boldsymbol{a}$ involves solving the following linear system

$$(\boldsymbol{H}^t\boldsymbol{H} + \mu\boldsymbol{V}^t \operatorname{diag}(\boldsymbol{b})\boldsymbol{V})\boldsymbol{a} = \boldsymbol{H}^t\boldsymbol{y} \tag{25}$$

which cannot be explicitly obtained and must be approximated iteratively. The conjugate gradient optimization algorithms are wildly used, ensuring a convergence towards the solution [32]. However, in our case, the computational cost remains important since our forward model is computationally burden. We therefore choose to adopt recent and efficient algorithms based on Majorize-Minimize step strategy and subspace optimization [22], [34].

C. Subspace Optimization With Majorize-Minimize Step

Since the criterion in Eq. (18) is differentiable (and convex if ϕ is convex), the optimization can be done with Non-Linear Conjugate Gradient [35], or more efficiently with subspace optimization methods. In the latter case, the iterative algorithm writes:

$$\boldsymbol{a}^{(k+1)} = \boldsymbol{a}^{(k)} + \alpha^{(k)}\boldsymbol{g}^{(k)} + \sum_{z=1}^{Z} \beta^{(k,z)}\boldsymbol{d}^{(k-z)} \tag{26}$$

where $\boldsymbol{g}^{(k)} = \nabla J(\boldsymbol{a}^{(k)})$ is the gradient of $J(\boldsymbol{a}^{(k)})$ at the iteration k, $\boldsymbol{d}^{(k-z)}$ are the previous descent directions, and $\alpha^{(k)}$ and $\beta^{(k,z)}$ are scalars.

We particularly rely on the Majorize-Minimize Memory Gradient (3MG) algorithm [22] that exploits the structure of the criterion in Eq (18) to compute both the steps α and the conjugacy parameter $\beta^{(z)}$ via the Quadratic Majorize-Minimize strategy. Therefore, Eq. (26) can be rewritten as

$$\boldsymbol{a}^{(k+1)} = \boldsymbol{a}^{(k)} + \boldsymbol{D}^{(k)}\boldsymbol{\alpha}^{(k)} \tag{27}$$

where $\boldsymbol{D}^{(k)}$ is the subspace of dimension Z and $\boldsymbol{\alpha}^{(k)}$ a vector of steps of size Z. Therefore, contrary to the traditional line search strategy, finding the steps can be done with the Quadratic Majorize-Minimize strategy in this subspace leading to an explicit formula of $\boldsymbol{\alpha}^{(k)}$ with

$$\boldsymbol{\alpha}^{(k)} = -{\boldsymbol{U}^{(k)}}^{-1}\nabla J^{(k)}\left(\boldsymbol{a}^{(k)}\right) \tag{28}$$

with $\boldsymbol{U}^{(k)} = {\boldsymbol{D}^{(k)}}^t\boldsymbol{A}^{(k)}\boldsymbol{D}^{(k)}$ a $Z \times Z$ matrix. In our experience, we choose $Z = 2$, that is a subspace of size 2 where search direction consists of the gradient and the previous search $\boldsymbol{D}^{(k-1)}\boldsymbol{\alpha}^{(k-1)}$. Note that this strategy leads to an efficient algorithm with guaranteed convergence, and we refer to [22] for more details.

IV. Experimental Results

This section tests the proposed reconstruction algorithm on two synthetic 3D spatio-spectral images with various spatial and spectral distributions. The developed forward model is general but primarily adapted for the Medium-Resolution Spectrometer of the Mid Infrared Instrument (MIRI/MRS) onboard the James Webb Space Telescope (JWST), measuring in the infrared spectral range, from 4.9 and 28.3 μm [36].

We compare the proposed algorithm to the state-of-art, which is the shift-and-add (*S&A*) reconstruction algorithm [37], [8] followed by a TV regularization. First, the *S&A* method shifts the overall measurements $\boldsymbol{y}_{c,p}[i', l']$ from all channels c and pointings p in order to align them (after a pre-processing step of the raw data). The results are then co-added, resulting in a reconstructed hyperspectral image with enhanced spatial resolution. This method corresponds to minimizing a least square criterion with

$$J(\boldsymbol{x}) = \|\boldsymbol{y} - \boldsymbol{S}\boldsymbol{x}\|^2 \tag{29}$$

with $\boldsymbol{y}^t = [\boldsymbol{y}^t_{0,0}, \ldots, \boldsymbol{y}^t_{C,P}]$ and $\boldsymbol{S}^t = [\boldsymbol{S}^t_{0,0}, \ldots, \boldsymbol{S}^t_{C,P}]$. $\boldsymbol{S}_{c,p}$ is a sampling and summation matrix that models detector sampling but neglect blurring. The solution then writes

$$\boldsymbol{x}_{S\&A} = (\boldsymbol{S}^t\boldsymbol{S})^{-1}\sum_{c,p}\boldsymbol{S}^t_{c,p}\boldsymbol{y}_{c,p} \tag{30}$$

where $\boldsymbol{S}^t_{c,p}$ is an upsampling matrix, and $(\boldsymbol{S}^t\boldsymbol{S})^{-1}$ is a diagonal normalization matrix that counts the number of times a pixel is measured.

Since the *S&A* algorithm does not account for the blurring, it is usually followed by a deconvolution step. In this work, we chose a TV regularization for spatial deconvolution at each wavelength l', implemented with the primal-dual Chambolle-Pock algorithm [38] writing

$$\hat{\boldsymbol{x}}^{l'}_{S\&A} = \arg\min_{\boldsymbol{x}}\left(\|\boldsymbol{y} - \boldsymbol{H}^{l'}\boldsymbol{x}^{l'}\|_2^2 + \mu|\nabla\boldsymbol{x}^{l'}|_1\right) \tag{31}$$

where $\boldsymbol{H}^{l'}$ is a spatial convolution operator for the wavelength l' and $\nabla\boldsymbol{x}^{l'}$ is the first-order difference of the spatial image for the same wavelength. This method does not allow data fusion since the spatial information is treated separately for every wavelength.

Moreover, to highlight the importance of the edge-preserving regularization choice (see section III-A), especially for 3D input images with sharp edges, our algorithm is also compared to the classic l_2 regularization [23]

$$\hat{\boldsymbol{a}}_{\mathrm{q}} = \arg\min_{\boldsymbol{a}}\left(\|\boldsymbol{y} - \boldsymbol{H}\boldsymbol{a}\|^2 + \mu\|\boldsymbol{V}\boldsymbol{a}\|^2\right) \tag{32}$$

solved via the conjugate-gradient optimization algorithm [39].

A. Setup of the experiment

We denote Obj_1 the first 3D input image, representing a synthetic object for which the results are easily interpretable. Obj_1 lives in a low-dimensional space, and expressed as a linear combination of $M = 3$ spectral components $\mathbf{s}_m$ computed from astrophysical measurements [40]; weighted by mixing coefficients $\boldsymbol{a}_m$ with sharp edges (see figure 3).

The second 3D input image, *Obj*$_2$, represents an astrophysical simulation of the photodissociation region located in the "*Orion bar*" [41]. It is made of $M = 4$ complex spectral distributions, containing sharp spectral lines and continuum emission, each weighted by their corresponding mixing coefficient a_m which presents structures in a wide range of spatial scales (see figure 4).

Both input images are represented on a 3D cartesian grid with $I \times J$ = 120×120 pixels with a spatial sampling step of $T_i = T_j = 0.1$ arcseconds. The spectral dimension for both input images measures the infrared range from $4.85\,\mu$m to $28.5\,\mu$m. *Obj*$_1$ counts $L = 3500$ wavelengths uniformly sampled with a step $T_l = 6.7\,10^{-3}\,\mu$m, whereas, *Obj*$_2$ counts $L = 3551$ wavelengths non-uniformly sampled with a step T_l varying from $2.4\,10^{-3}$ to $1.4\,10^{-2}\,\mu$m.

The spectral dimension is divided by the HS instrument into four distinct spectral channels, with different spectral range, FOV, slit width and number (see table I). The optical component of the HS instrument is limited by the diffraction [6] with a PSF assumed known. The analytic form of the PSF for a monochromatic wavelength λ can be theoretically obtained from the Fourier transform of the aperture function of the telescope. The PSF width depends on the wavelength, and its FWHM is $\simeq \lambda/D$ (radians), with D referring to the diameter of the telescope aperture. However, for the JWST, there is no exact analytical description of the aperture function. Thus, the PSF is numerically computed using the WebbPSF [25] package, developed by the Space Telescope Science Institute (STScI). Fig. IV-A shows three monochromatic PSF at 5, 15, and $25\,\mu$m in logarithmic scales. It highlights the importance of considering a wavelength-dependent PSF in our model, especially since the FWHM of the PSF increases by a factor of 5 between the shortest and longest wavelength.

To allow multi-frame measurements, the forward model considers multiple observations of the same 3D input image, with a dithering pattern of 8 pointing directions. For a particular pointing, the light inside each spatio-spectral selection $\boldsymbol{x}_c$ is dispersed and projected onto 2D detectors with different spectral resolution R, and different spatial and spectral step sizes depending on the channel. The spatial step size of the measurements $T_{i'}$ is fixed by the spatial sampling of the detector. Given the large size of the MRS detectors, we consider in this work that the spectral step size of the measurements is $T_{l'} = 4 \times T_{l'}^{\text{MRS}}$ and the spectral resolution is $R = R^{\text{MRS}}/4$, in order to reduce the computational cost of the problem, where $T_{l'}^{\text{MRS}}$ and R^{MRS} are the spectral sampling of the detector and the spectral resolution of the actual MRS instrument, respectively, provided in [36]. The values of $T_{i'}$, $T_{l'}$, and R, along with the dimension in pixels of the measurements (I', L') are given in Table I. The 2D measurements are finally corrupted with an additive zero-mean white Gaussian noise and with SNR = 30 dB.

The algorithms are implemented in Python with the Numpy library and Q-MM [3]toolbox [28] for Quadratic Majorization-Minimization, with a single CPU at 5GHz with 32 GB of memory.

[3]https://github.com/forieux/qmm/

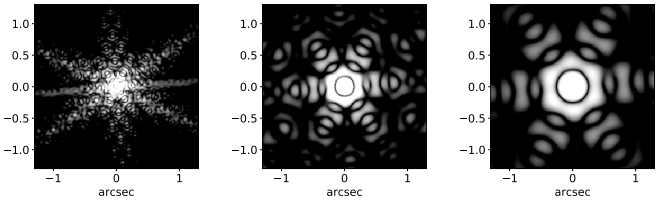

(a) $\lambda = 5\,\mu$m (b) $\lambda = 15\,\mu$m (c) $\lambda = 25\,\mu$m

Fig. 2. PSF at different wavelengths of JWST/MIRI (logarithmic scale) simulated with the WebbPSF package [25]

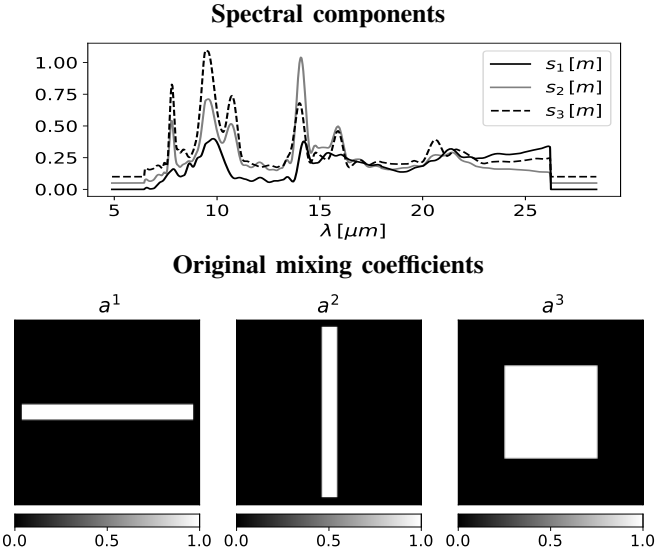

Fig. 3. Spectral components and mixing coefficients for Obj_1

B. Estimation results for $\hat{\boldsymbol{a}}_m$

The estimation of the mixing coefficients $\hat{\boldsymbol{a}}_m$ depends on the overall blurred, sampled, and noisy measurements $\boldsymbol{y}$. Fig. 5 shows the reconstruction of the mixing coefficients for Obj_1 and Obj_2. The red frames in Fig. 5 represent the largest observed FOV, corresponding to the *Channel 4* (see Tab. I). We are interested in reconstructing $\hat{\boldsymbol{a}}_m$ inside this FOV even if for the other channels (or wavelengths), no measurements has been made. We test our reconstruction algorithm with a sufficient number of iterations (see Table II) to ensure convergence towards the solution $\hat{\boldsymbol{a}}_m$. The reconstruction of $\boldsymbol{a}_m$ for *Obj*$_2$ is computationally more expensive than that for *Obj*$_1$, since *Obj*$_2$ has one more spectral component.

Our proposed algorithm is based on minimizing the regularized objective function in Eq. (18) with a convex regularization function ϕ for edge-preserving. We particularly focus on the Huber potential function [21] with

$$\phi(\delta, T) = \begin{cases} \delta^2, & \text{if } |\delta| \leq T. \\ 2T|\delta| - T^2 & \text{otherwise, } T \in \mathbb{R}^+. \end{cases} \tag{33}$$

The Huber function is continuously differentiable with a quadratic form below a fixed threshold T to promote smoothness to the solution, and a linear form above T to preserve the high gradient values. Consequently, two regularization parameters μ and T must be tuned to ensure the best recon-

Ch.	Spectral range (μm)	FOV (pixels)	Slit width (arcsec)	Slit number	$T_{i'}$ (arcsec)	$T_{l'}$ (μm)	I' pixels	L' pixels	R
1	4.9 – 7.7	34×42	$2 \times T_j$	21	$2 \times T_i$	$4\,10^{-3}$	17	750	867
2	7.4 – 11.7	42×51	$3 \times T_j$	17	$2 \times T_i$	$6\,10^{-3}$	21	750	760
3	11.5 – 18.1	57×64	$4 \times T_j$	16	$3 \times T_i$	$9\,10^{-3}$	19	750	596
4	17.7 – 28.5	72×72	$5 \times T_j$	12	$3 \times T_i$	$1.6\,10^{-2}$	24	750	410

TABLE I
CHARACTERISTICS SPECIFIC TO THE FOUR SPECTRAL CHANNELS OF THE IFS INSTRUMENT CONSIDERED IN THIS WORK.

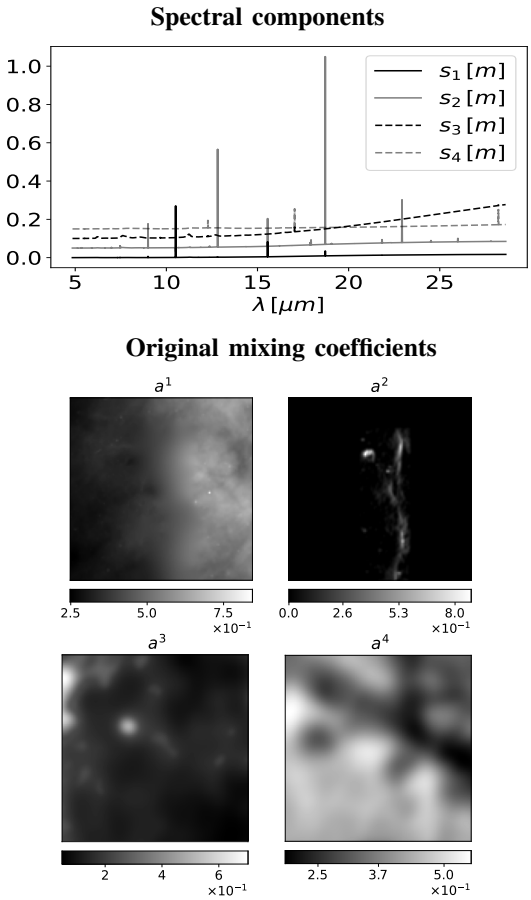

Fig. 4. Spectral components and mixing coefficients for Obj_2

	Iterations	Runtime [s] per iteration	μ	T
Obj_1	455	7.8	18	0.025
Obj_2	633	10.6	0.005 ($m \neq 2$) 0.0005 ($m = 2$)	1.5 ($m \neq 2$) 0.001 ($m = 2$)

TABLE II
ITERATION NUMBERS AND HYPERPARAMETER VALUES FOR BOTH INPUT OBJECTS

struction. Their values are reported in Table II. In practise we have minimized the normalised least square error between the original $\boldsymbol{a}_m$ mixing coefficient and the estimated ones $\hat{\boldsymbol{a}}_m$ for both objects

$$\text{Error}(\mu, T) = \|\boldsymbol{a}_m - \hat{\boldsymbol{a}}_m(\mu, T)\|_2 / \|\boldsymbol{a}_m\|_2. \qquad (34)$$

The spatial distribution differs between $\boldsymbol{a}_m$ for Obj_2, particularly between $\boldsymbol{a}_{m=2}$ which contains sharp edges and $\boldsymbol{a}_{m\neq 2}$ which are smoother. Therefore, we have used one set of parameters (μ, T) for $m = 2$, and an other one for $m \neq 2$ (see Table II).

The comparison between figures 3-4 and figure 5 shows that the reconstructed mixing coefficients $\hat{\boldsymbol{a}}_m$ for both objects are unmixed and deconvoluted while preventing noise amplification without excessive penalization of sharp edges. The normalized least square error are as small as 0.039% and 0.327%, for Obj_1 and Obj_2, respectively.

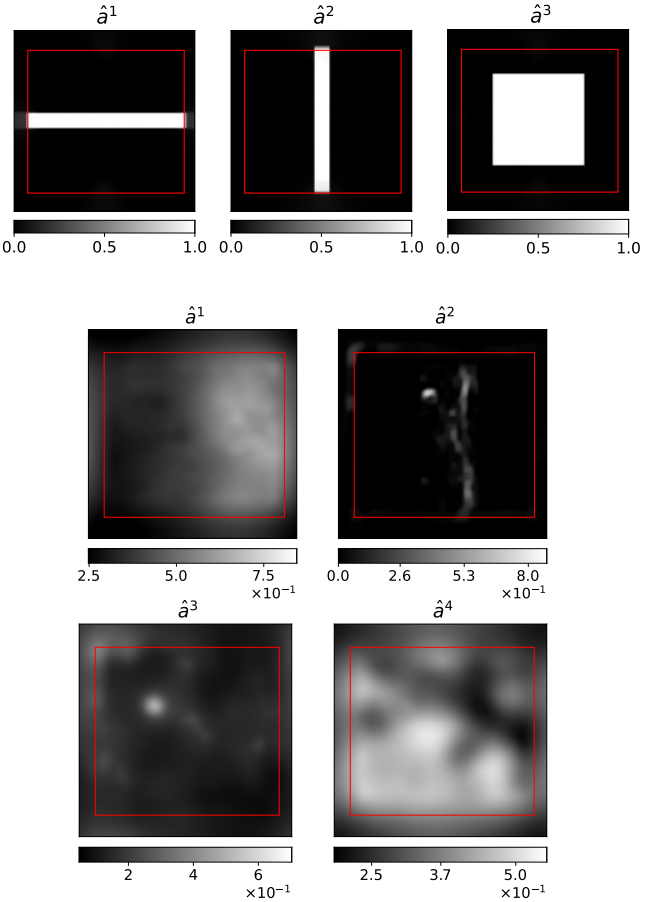

Fig. 5. Estimated mixing coefficients $\hat{\boldsymbol{a}}_m$ for Obj_1 (top) and Obj_2 (bottom)

C. Hyperspectral Reconstruction

In this section, we compare the original and the reconstructed 3D images with the proposed and state-of-the-art

algorithms. The reconstructed HS image are obtained from the estimated mixing coefficients $\hat{\boldsymbol{a}}_m$ using Eq. (8). In addition to the l_2 reconstruction, the proposed results are compared to the "Shift and Add" algorithm (*S&A*) Eq. (30) followed by a TV deconvolution using Eq. (31).

We first showcase in Fig. 6 the spectral distribution at the center of the FOV of the original and the reconstructed images computed with the *S&A* and the proposed algorithms. Qualitatively the spectral distribution of the reconstructed image with the proposed algorithm matches the original spectral distribution over the whole measured range. On the other hand, the *S&A* algorithm fails to fully reconstruct the spectral distribution, particularly the spectral lines in Obj_2, which appears broader and less intense than the original ones. Such results are expected since the *S&A* algorithm does not consider the spectral blurring initially introduced by the wavelength dispersion system.

Fig. 9 illustrates the spatial distribution of the reconstructed 3D image of Obj_1 for three monochromatic images at $\lambda = 6.5$, 14 and 21 μm, respectively, belonging to channels 1, 3, and 4. The loss of spatial information caused by the detector integration is compensated in the multi-frame SR reconstruction using the *S&A* algorithm. However, since this method does not consider spectral variations of the PSF, the reconstructed images are blurred, especially at long wavelengths. We proceed by applying a TV deconvolution for each monochromatic image. This added step allows better preservation of sharp edges and smaller errors but fails to restore spatial details at small scale since the regularization is applied separately for each monochromatic image and does not account for the correlations between spectral bands. On the other hand, the proposed algorithm shows a good performance with smaller error values for all monochromatic images. The improvement of spatial resolution is striking, and the spatial dynamic range appears fully reconstructed. Moreover, the edges in the image are well preserved, whereas the l_2 approach introduces smoothing and ringing artifacts.

Fig. 10 shows the spatial distribution of the reconstructed HS image for Obj_2, for three monochromatic images at $\lambda = 6.5$ μm which belongs to a continuum, and at $\lambda = 17$ and 18.7 μm corresponding to two different spectral lines. As mentioned earlier, the reconstructed spectral lines with the *S&A* algorithm are spectrally broaden because the spectral response in not taken into account. Hence, for a fair comparison between the algorithms, we have spectrally integrated the reconstructed HS image with the *S&A* algorithm over the broad reconstructed spectral line, then we proceed with the TV deconvolution for the integrated images. Our proposed algorithm shows the best qualitative reconstructions with the lowest errors for all monochromatic images. The l_2 approach gives good results with comparable errors for the smooth images but fails to preserve the sharp edges, particularly at $\lambda = 18.7$ μm as illustrated in Fig. 7. Analogously to Obj_1, the *S&A* and TV algorithms fail to fully reconstruct small-scale spatial details.

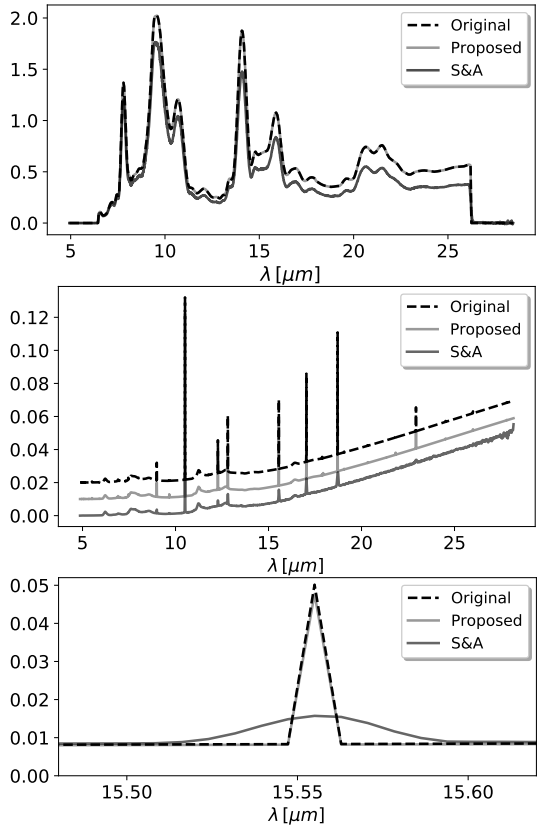

Fig. 6. Spectral distribution of the reconstructed HS image with the proposed and *S&A* algorithms, at the central spatial position (60,60) for Obj_1 (Top), Obj_2 (Middle: note that the three spectral distributions are shifted for clarity). The bottom panel presents a zoom on a spectral line for Obj_2 .

Fig. 7. Zoom on sharp edges for Obj_2 at 18.7μm: [Left] Original, [center] proposed, [right] l_2 approach.

D. Quality Metrics

To better evaluate the spatial and spectral performances of the reconstruction algorithms, we use three quantitative measurements:

1) the Spectral Angular Mapper (SAM) [42] measuring the spectral distortion, in radians, of the m^{th} pixel

$$\text{SAM}(m) = \arccos\left(\frac{< \boldsymbol{x}_m, \hat{\boldsymbol{x}}_m >}{\|\boldsymbol{x}_m\|_2 \|\hat{\boldsymbol{x}}_i\|_m}\right). \qquad (35)$$

where $\boldsymbol{x}_m$ and $\hat{\boldsymbol{x}}_m$ are the spectral vector of the m^{th} spatial location ($m \in [0, \ldots, I] \times [0, \ldots, J]$) of the original and reconstructed 3D images, respectively. The further the SAM value is from 0, the greater the spectral distortion.

2) the peak signal-to-noise ratio (PSNR)

$$\text{PSNR}(l) = 10 \log_{10}\left(\frac{\max(\boldsymbol{x})^l}{\|\boldsymbol{x}^l - \hat{\boldsymbol{x}}^l\|^2}\right). \qquad (36)$$

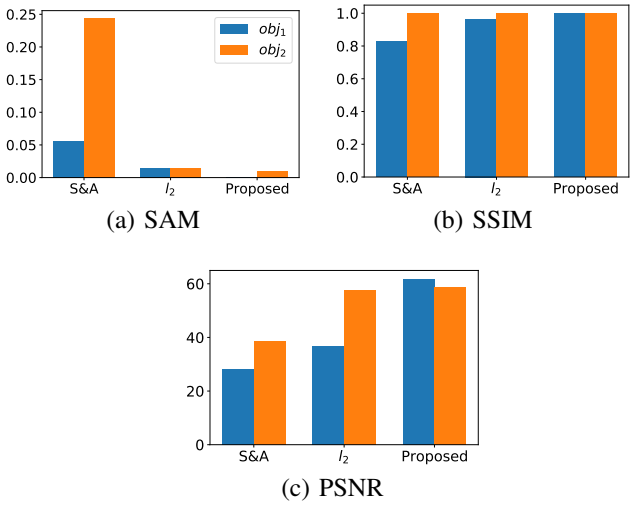

(a) SAM (b) SSIM

(c) PSNR

Fig. 8. Global SAM(a), SSIM(b), and PSNR(c) for obj_1 and obj_2

PSNR(l) denotes the PSNR of the spatial image at the l^{th} spectral band of $\boldsymbol{x}$ and $\hat{\boldsymbol{x}}$.

3) the Structural Similarity Index (SSIM) [43], computed for each l^{th} spectral band, whose value varies between 0 and 1. The higher the value, the better the similarity.

The global SAM is computed by averaging over the whole image, while the global PSNR and SSIM are computed by averaging all spectral bands.

We illustrate in Fig. 8, the average SAM, SSIM, and PSNR for Obj_1 and Obj_2. The proposed algorithm shows the best spectral reconstruction with the lowest distortion for both objects. The spectral distortion is very high for Obj_2 and the *S&A* algorithm, due to the presence of sharp spectral lines which are hardly recovered by this algorithm. Moreover, our algorithm shows the best similarity index, especially for Obj_1. Overall, the proposed algorithm shows the best spatio-spectral reconstruction for both scenes, with the highest average PSNR values.

V. Conclusion

We present in this work a new model for hyperspectral data fusion based on low-rank approximation and a new efficient Super-Resolution algorithm for hyperspetral reconstruction based on Quadratic Majorization-Minimization optimization algorithm.

The first contribution is to develop an explicit forward model based on IFS instruments. This model takes as input a high spatio-spectral resolution image, approximated on a low-rank subspace, and acquire a set of 2D measurements with a high spectral resolution, projected onto different detectors with different characteristics. The complex forward model takes into account (1) different observations of the same scene with sub-pixel shifts, (2) wavelength-dependent spatial and spectral PSFs, (3) different spectral channels and IFUs, observing the input with different spectral ranges and different numbers of slits of different sizes, and finally (4) heterogeneous spatio-spectral samplings.

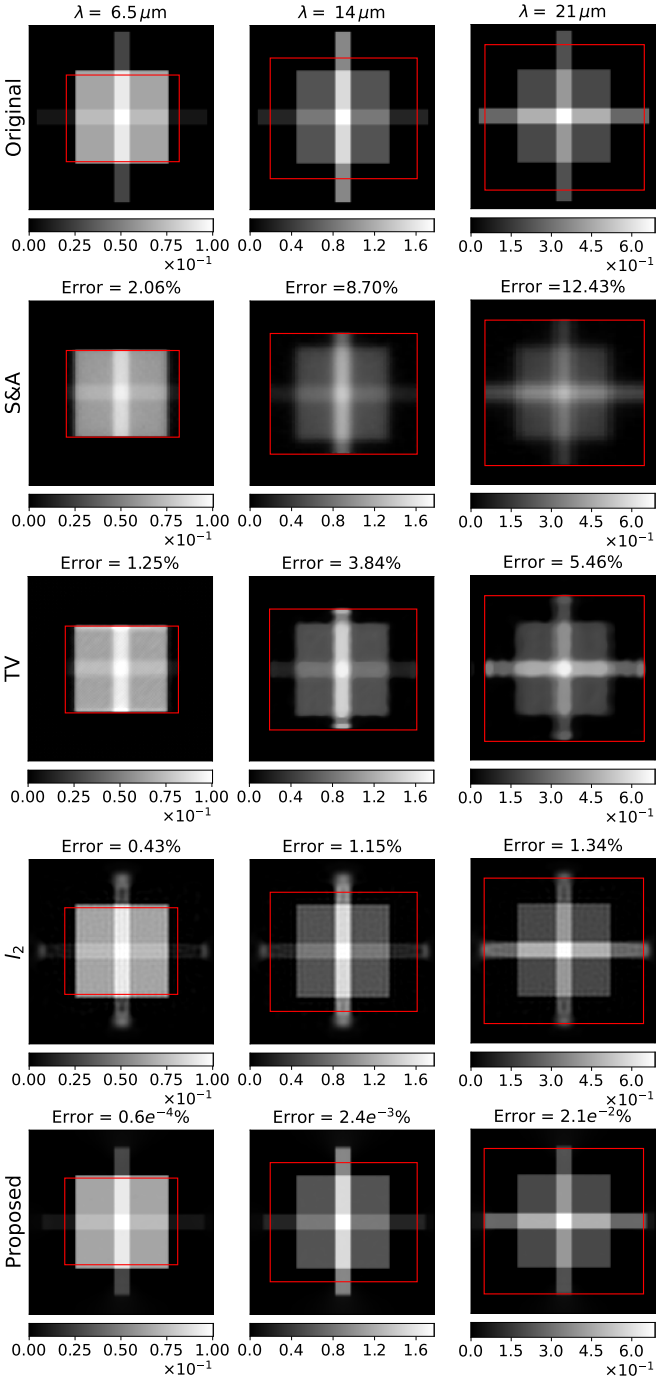

Fig. 9. Spatial reconstruction for Obj_1: [1st row] Original images at 6.5, 14, and 21 μm. [2nd row] *S&A*. [3rd row] TV restoration. [4th row] Reconstruction with l_2. [5th row] proposed.

The second contribution is a fusion of the multi-frame blurred and sampled 2D measurements, acquired from different spectral channels, in order to restore the single HSI observed input. The algorithm is based on the regularized least square approach with convex edge-preserving regularization, and solved via the iterative Majorize-Minimize Memory Gradient (3MG) [22] optimization algorithm, with freely provided

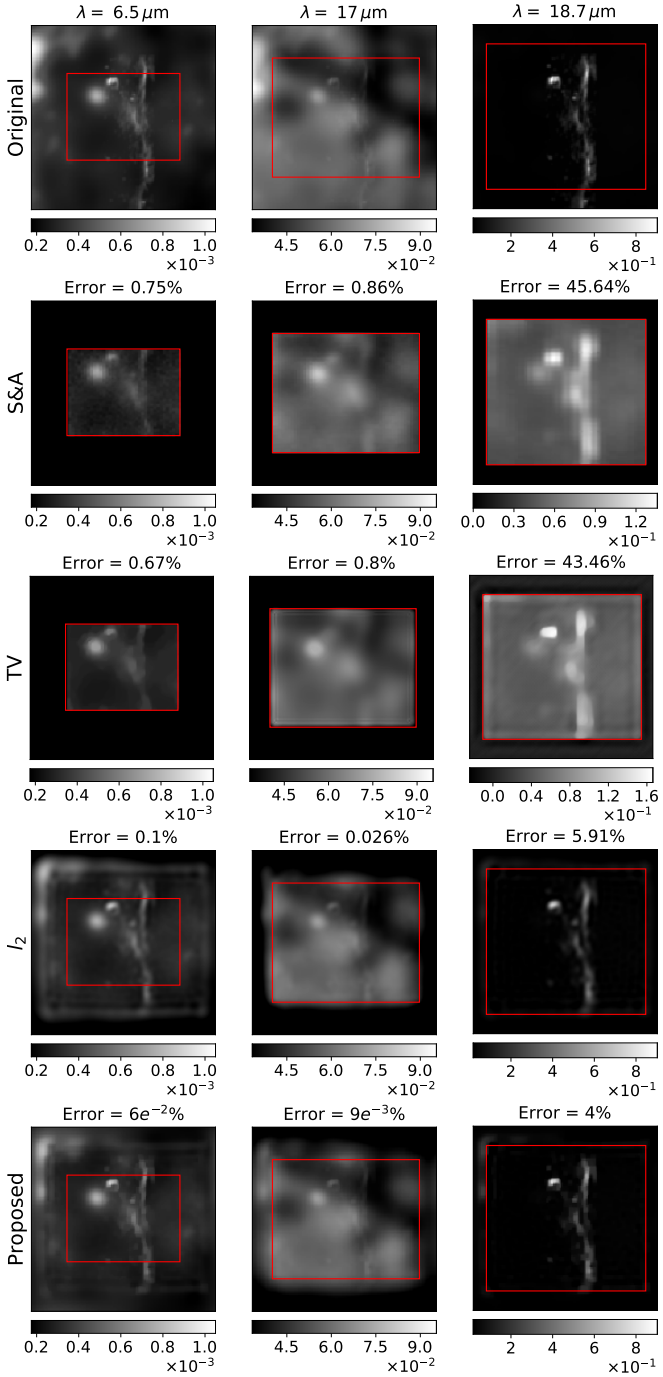

Fig. 10. Spatial reconstruction for Obj_2: [1st row] Original images at 6.5, 17, and 18.7 μm. [2nd row] Reconstruction with *S&A*. [3rd row] TV restoration. [4th row] l_2 approach. [5th row] proposed.

code[4].

Our method allows joint spectral unmixing and spatial and spectral enhancements. The spectral components, known *a priori*, serve as a spectral regularization to our approach and prevent spectral distortion, whereas the multi-frame observations and the enforced spatial regularization allow restoring the original spatial distribution without excessive penalization of high gradient values.

Our work is validated with relative error below 1% over the whole reconstructed HS images for an SNR = $30\,$dB. Our algorithm outperformed qualitatively and quantitatively the l_2 approach, as well as the standard *S&A* and TV deconvolution algorithms.

Several perspectives can be considered. First, the spatial and spectral resolutions of the reconstructed 3D image can be enhanced by performing a fusion between the IFS measurements with high spectral but low spatial resolution, considered in this work, and multispectral measurements with high spatial but low spectral resolution, observing the same scene. The fusion problem can be solved in the inverse problem framework [1]. In addition, the spectral components of the LMM are, in many applications, not provided *a priori* and must be extracted or learned directly from the measurements along with the mixing coefficients [44]. In a wider perspective, we also would like to estimate the hyperparameters jointly with the 3D input image instead of being fixed by hand. The problem can be formulated in the Bayesian framework where the solution is deduced from *a posteriori* law for the unknown hyperparameters and the 3D input image [45].

[4] http://github.com/forieux/qmm

References

[1] C. Guilloteau, T. Oberlin, O. Berné, and N. Dobigeon, "Hyperspectral and multispectral image fusion under spectrally varying spatial blurs – application to high dimensional infrared astronomical imaging," *IEEE Transactions on Computational Imaging*, vol. 6, pp. 1362–1374, 2020.

[2] J. G. Dwight and T. S. Tkaczyk, "Lenslet array tunable snapshot imaging spectrometer (latis) for hyperspectral fluorescence microscopy," *Biomed. Opt. Express*, vol. 8, no. 3, pp. 1950–1964, Mar 2017. [Online]. Available: http://www.osapublishing.org/boe/abstract.cfm?URI=boe-s8-s3-s1950

[3] M. Shimoni, R. Haelterman, and C. Perneel, "Hypersectral imaging for military and security applications: Combining myriad processing and sensing techniques," *IEEE Geoscience and Remote Sensing Magazine*, vol. 7, no. 2, pp. 101–117, 2019.

[4] G. Lu and B. Fei, "Medical hyperspectral imaging: a review," *Journal of Biomedical Optics*, vol. 19, no. 1, pp. 1 – 24, 2014. [Online]. Available: https://doi.org/10.1117/1.JBO.19.1.010901

[5] S. Vives, E. Prieto, Y. Salaun, and P. Godefroy, "New technological developments in integral field spectroscopy," in *Advanced Optical and Mechanical Technologies in Telescopes and Instrumentation*, E. Atad-Ettedgui and D. Lemke, Eds., vol. 7018, International Society for Optics and Photonics. SPIE, 2008, pp. 959 – 968. [Online]. Available: https://doi.org/10.1117/12.789576

[6] J. W. Goodman, *Introduction to Fourier Optics McGraw-Hill Series in Electrical and Computer Engineering*, 1996, vol. 8, no. 5. [Online]. Available: http://stacks.iop.org/1355-s5111/8/i=5/a=014?key=crossref.ad20ea108e8f625cb0486bf680f74198

[7] J.-P. Pérez, *Optique - Fondements et applications*. Paris, France:Dunod, 2004.

[8] A. S. Fruchter and R. N. Hook, "Drizzle: A method for the linear reconstruction of undersampled images," *Publications of the Astronomical Society of the Pacific*, vol. 114, no. 792, pp. 144–152, feb 2002. [Online]. Available: https://doi.org/10.1086%2F338393

[9] R. Hook and A. Fruchter, "Dithering, sampling and image reconstruction," vol. 216, p. 521, 01 2000.

[10] Sung Cheol Park, Min Kyu Park, and Moon Gi Kang, "Super-resolution image reconstruction: a technical overview," *IEEE Signal Processing Magazine*, vol. 20, no. 3, pp. 21–36, May 2003.

[11] M. Elad and Y. Hel-Or, "A fast super-resolution reconstruction algorithm for pure translation motion and common space-invariant blur," *IEEE Transactions on Image Processing*, vol. 10, pp. 1187–1193, 01 2001.

[12] L. I. Rudin, S. Osher, and E. Fatemi, "Nonlinear total variation based noise removal algorithms," *Physica D: Nonlinear Phenomena*, vol. 60, no. 1, pp. 259–268, 1992. [Online]. Available: https://www.sciencedirect.com/science/article/pii/016727899290242F

[13] T. Akgun, Y. Altunbasak, and R. M. Mersereau, "Super-resolution reconstruction of hyperspectral images," *IEEE Transactions on Image Processing*, vol. 14, no. 11, pp. 1860–1875, 2005.

[14] H. Zhang, L. Zhang, and H. Shen, "A super-resolution reconstruction algorithm for hyperspectral images," *Signal Processing*, vol. 92, no. 9, pp. 2082 – 2096, 2012. [Online]. Available: http://www.sciencedirect.com/science/article/pii/S0165168412000345

[15] H. Stark and P. Oskoui, "High-resolution image recovery from image-plane arrays, using convex projections," *J. Opt. Soc. Am. A*, vol. 6, no. 11, pp. 1715–1726, Nov 1989. [Online]. Available: http://josaa.osa.org/abstract.cfm?URI=josaa-s6-s11-s1715

[16] I. T. Jolliffe and J. Cadima, "Principal component analysis: a review and recent developments," *Philosophical Transactions of the Royal Society A: Mathematical, Physical and Engineering Sciences*, vol. 374, 2016.

[17] R. Schultz and R. Stevenson, "Extraction of high-resolution frames from video sequences," *IEEE transactions on image processing : a publication of the IEEE Signal Processing Society*, vol. 5, pp. 996–1011, 02 1996.

[18] G. Vivone, L. Alparone, J. Chanussot, M. Dalla Mura, A. Garzelli, G. Licciardi, R. Restaino, and L. Wald, "A critical comparison among pansharpening algorithms," vol. 53, 07 2014.

[19] Q. Wei, J. Bioucas-Dias, N. Dobigeon, and J. Tourneret, "Hyperspectral and multispectral image fusion based on a sparse representation," *IEEE Transactions on Geoscience and Remote Sensing*, vol. 53, no. 7, pp. 3658–3668, 2015.

[20] M. Simões, J. M. Bioucas-Dias, L. B. Almeida, and J. Chanussot, "A convex formulation for hyperspectral image superresolution via subspace-based regularization," *CoRR*, vol. abs/1411.4005, 2014. [Online]. Available: http://arxiv.org/abs/1411.4005

[21] J. Idier, "Convex half-quadratic criteria and interacting auxiliary variables for image restoration," *IEEE Transactions on Image Processing*, vol. 10, no. 7, pp. 1001–1009, July 2001.

[22] E. Chouzenoux, J. Idier, and S. Moussaoui, "A majorize–minimize strategy for subspace optimization applied to image restoration," *IEEE Transactions on Image Processing*, vol. 20, no. 6, pp. 1517–1528, 2011.

[23] A. N. Tikhonov, A. Goncharsky, V. V. Stepanov, and A. G. Yagola, *Numerical Methods for the Solution of Ill-Posed Problems*, ser. Mathematics and Its Applications. Springer Netherlands, 1995. [Online]. Available: https://www.springer.com/gp/book/9780792335832

[24] J. Adams, M. Smith, and P. Johnson, "Spectral mixture modeling: A new analysis of rock and soil types at the viking lander 1 site," *Journal of Geophysical Research*, vol. 91, pp. 8098–8112, 1986.

[25] M. D. Perrin, R. Soummer, E. M. Elliott, M. D. Lallo, and A. Sivaramakrishnan, "Simulating point spread functions for the James Webb Space Telescope with WebbPSF," in *Space Telescopes and Instrumentation 2012: Optical, Infrared, and Millimeter Wave*, M. C. Clampin, G. G. Fazio, H. A. MacEwen, and J. M. O. Jr., Eds., vol. 8442, International Society for Optics and Photonics. SPIE, 2012, pp. 1193 – 1203. [Online]. Available: https://doi.org/10.1117/12.925230

[26] B. Hunt, "A matrix theory proof of the discrete convolution theorem," *IEEE Transactions on Audio and Electroacoustics*, vol. 19, no. 4, pp. 285–288, 1971.

[27] D. D. Lee and H. S. Seung, "Learning the parts of objects by nonnegative matrix factorization," *Nature*, vol. 401, pp. 788–791, 1999.

[28] F. Orieux and R. Abirizk, "Q-mm: The quadratic majorize-minimize python toolbox." [Online]. Available: https://github.com/forieux/qmm

[29] Y. Zhao, J. Yang, Q. Zhang, L. Song, Y. Cheng, and Q. Pan, "Hyperspectral imagery super-resolution by sparse representation and spectral regularization," *EURASIP Journal on Advances in Signal Processing*, vol. 2011, no. 1, pp. 1–10, 2011.

[30] T. Zhang, Y. Fu, L. Wang, and H. Huang, "Hyperspectral image reconstruction using deep external and internal learning," in *2019 IEEE/CVF International Conference on Computer Vision (ICCV)*, 2019, pp. 8558–8567.

[31] D. Geman and G. Reynolds, "Constrained restoration and the recovery of discontinuities," *IEEE Transactions on Pattern Analysis and Machine Intelligence*, vol. 14, no. 3, pp. 367–383, 1992.

[32] M. Allain, J. Idier, and Y. Goussard, "On global and local convergence of half-quadratic algorithms," *IEEE Transactions on Image Processing*, vol. 15, no. 5, pp. 1130–1142, 2006.

[33] R. Abi-rizk, F. Orieux, and A. Abergel, "Non-stationary hyperspectral forward model and high-resolution," in *2020 IEEE International Conference on Image Processing (ICIP)*, 2020, pp. 2975–2979.

[34] C. Labat and J. Idier, "Doi 10.1007/s10957-007-9306-x convergence of conjugate gradient methods with a closed-form stepsize formula," *Journal of Optimization Theory and Applications*, vol. 136, pp. 43–60, 01 2008.

[35] J. Nocedal, "Conjugate gradient methods and nonlinear optimization," *Linear and nonlinear conjugate gradient-related methods*, pp. 9–23, 1996.

[36] M. Wells, J. W. Pel, A. Glasse, G. Wright, G. Kroes, R. Azzollini, S. Beard, B. Brandl, A. Gallie, V. C. Geers, A. M. Glauser, P. Hastings, T. Henning, R. Jager, K. Justtanont, B. Kruizinga, F. Lahuis, D. Lee, I. Martinez Delgado, and D. Wright, "The mid-infrared instrument for the james webb space telescope, vi: The medium resolution spectrometer," *Publications of the Astronomical Society of the Pacific*, vol. 127, pp. 646–664, 07 2015.

[37] S. Farsiu, D. Robinson, M. Elad, and P. Milanfar, "Robust shift and add approach to superresolution," in *Applications of Digital Image Processing XXVI*, A. G. Tescher, Ed., vol. 5203, International Society for Optics and Photonics. SPIE, 2003, pp. 121 – 130. [Online]. Available: https://doi.org/10.1117/12.507194

[38] A. Chambolle and T. Pock, "A first-order primal-dual algorithm for convex problems with applications to imaging," *Journal of Mathematical Imaging and Vision*, vol. 40, 05 2011.

[39] J. R. Shewchuk *et al.*, "An introduction to the conjugate gradient method without the agonizing pain," 1994.

[40] O. Berné, C. Joblin, Y. Deville, J. D. Smith, M. Rapacioli, J. P. Bernard, J. Thomas, W. Reach, and A. Abergel, "Analysis of the emission of very small dust particles from Spitzer spectro-imagery data using blind signal separation methods," *Astronomy and Astrophysics - A&A*, vol. 469, pp. 575–586, July 2007, 14 pages, 11 figures, to appear in A&A. [Online]. Available: https://hal.archives-souvertes.fr/hal-s00287344

[41] C. Guilloteau, T. Oberlin, O. Berné, E. Habart, and N. Dobigeon, "Simulated jwst data sets for multispectral and hyperspectral image fusion," *The Astronomical Journal*, vol. 160, no. 1, p. 28, Jun 2020. [Online]. Available: http://dx.doi.org/10.3847/1538-s3881/ab9301

[42] Chein-I Chang, "An information-theoretic approach to spectral variability, similarity, and discrimination for hyperspectral image analysis," *IEEE Transactions on Information Theory*, vol. 46, no. 5, pp. 1927–1932, 2000.

[43] Zhou Wang, A. C. Bovik, H. R. Sheikh, and E. P. Simoncelli, "Image quality assessment: from error visibility to structural similarity," *IEEE Transactions on Image Processing*, vol. 13, no. 4, pp. 600–612, 2004.

[44] S. Henrot, C. Soussen, M. Dossot, and D. Brie, "Does deblurring improve geometrical hyperspectral unmixing?" *IEEE Transactions on Image Processing*, vol. 23, no. 3, pp. 1169–1180, 2014.

[45] N. Dobigeon, S. Moussaoui, M. Coulon, J.-Y. Tourneret, and A. O. Hero, "Joint bayesian endmember extraction and linear unmixing for hyperspectral imagery," *IEEE Transactions on Signal Processing*, vol. 57, no. 11, pp. 4355–4368, 2009.

Ralph Abi Rizk is a Ph.D student at Laboratoire signaux et systèmes (Université Paris-Saclay, CNRS, CentraleSupélec), France. His research interests include image and signal processing, particularly inverse problem approaches, hyperspectral image reconstruction, and data fusion for astrophysics applications.

François Orieux is Assistant Professor at the Université Paris-Saclay in the Laboratoire des Signaux et Systèmes, Groupe Problèmes Inverses (Université Paris-Saclay, CNRS, CentraleSupélec), France. He is also an associate researcher with the Institut d'Astrophysique Spatiale (Univ. Paris- Saclay, CNRS). He received his Ph.D. degree in signal processing at Université Paris-Sud, Orsay, France. His research focuses on Bayesian methodological approaches for ill-posed inverse problems resolution with examples of applications in astrophysics or biological microscopy.

Alain Abergel is professor of Physics and Astrophysics at the Paris-Saclay University. He is astrophysicist of the interstellar medium at the Institut d'Astrophysique Spatiale (Paris-Saclay University, CNRS), and is involved in the scientific exploitation of several space missions for astrophysics (ISO, Spitzer, Herschel, Planck, JWST, . . .).

5.3 Comparison between 3D reconstructions directly from measurements and via mixture coefficient estimation

We have developed in this thesis two different forward models for the same IFS instrument but with different linear models for the 2D+λ input image. In Chapter 4, the developed forward model was used to reconstruct the spatial and spectral distribution of $\boldsymbol{x}$ directly from the measurements $\boldsymbol{y}$. We refer to this reconstruction in this section as the spatio-spectral reconstruction. In this Chapter, we choose the LMM model for $\boldsymbol{x}$ with known spectral components $\mathbf{s}$, and developed a spectral-dependent forward model used to estimate the mixing coefficients $\boldsymbol{a}$. Consequently, the full reconstructed 3D image $\hat{\boldsymbol{x}}$ results from $\sum_{m=1}^{M} \hat{\boldsymbol{a}}_m \mathbf{s}_m$. We refer to this reconstruction as the LMM reconstruction. The spatio-spectral and LMM reconstructions are based on minimizing a regularized objective function for edge-preserving, but are solved with different algorithms. For the spatio-spectral reconstruction, we used the fast half-quadratic approaches based on Geman and Reynolds formulation [Geman 1992], and for the LMM reconstruction, we used the Majorize-Minimize Memory Gradient algorithm [Chouzenoux 2011].

This section compares the reconstructed spatial and spectral distributions for Obj_1 with the two proposed reconstructed algorithms and analyzes the produced results.

Spatial distribution: Comparison between the original and the reconstructed images are shown at 6.5, 14, and 21 μm in Fig. 5.1. Overall, both algorithms show a good spatial reconstruction with relatively small errors. The spatial dynamic for both reconstructions is fully restored, and the spatial resolution is improved while preserving the edges. However, the spatial distributions with the LMM reconstruction have smaller errors than with the spatio-spectral reconstruction for all wavelengths. Firstly, the subspace approximation of the 2D+λ input reduces the number of unknowns that we estimate, leading to an increase in the signal-to-noise ratio (SNR) on the reconstructed 2D+λ image. In addition, the LMM reconstruction only requires a spatial reconstruction to enhance the spatial resolution of the reconstructed mixing coefficients $\hat{\boldsymbol{a}}$, whereas the spatio-spectral reconstruction is done at every wavelength yielding to larger errors in the reconstructed spatial distribution, especially at longer wavelengths where the blurring is more significant.
To better showcase the performance of the two reconstruction algorithms, we show in Fig. 5.2 a plot of the spatial distribution at the central row of the reconstructed Obj_1, at 6.5, 9, 14, and 21 μm. We can see that both of the proposed algorithms perfectly reconstruct the spatial distribution, particularly around edges, except for at 21 μm where the LMM reconstruction allows a better performance around the edges. Finally, as mentioned in paragraph IV-B of section 5.2, the FOV of the estimated $\hat{\boldsymbol{a}}$ corresponds to the largest FOV observed by the IFS despite the spectral channel. Consequently, the reconstructed $\hat{\boldsymbol{x}}$ with the LMM have the same FOV at

all wavelengths. This is not the case for the reconstructed $\hat{\boldsymbol{x}}$ with the spatio-spectral reconstruction, since the corresponding FOV changes according to the channel (as shown in the middle panel of Fig. 5.2).

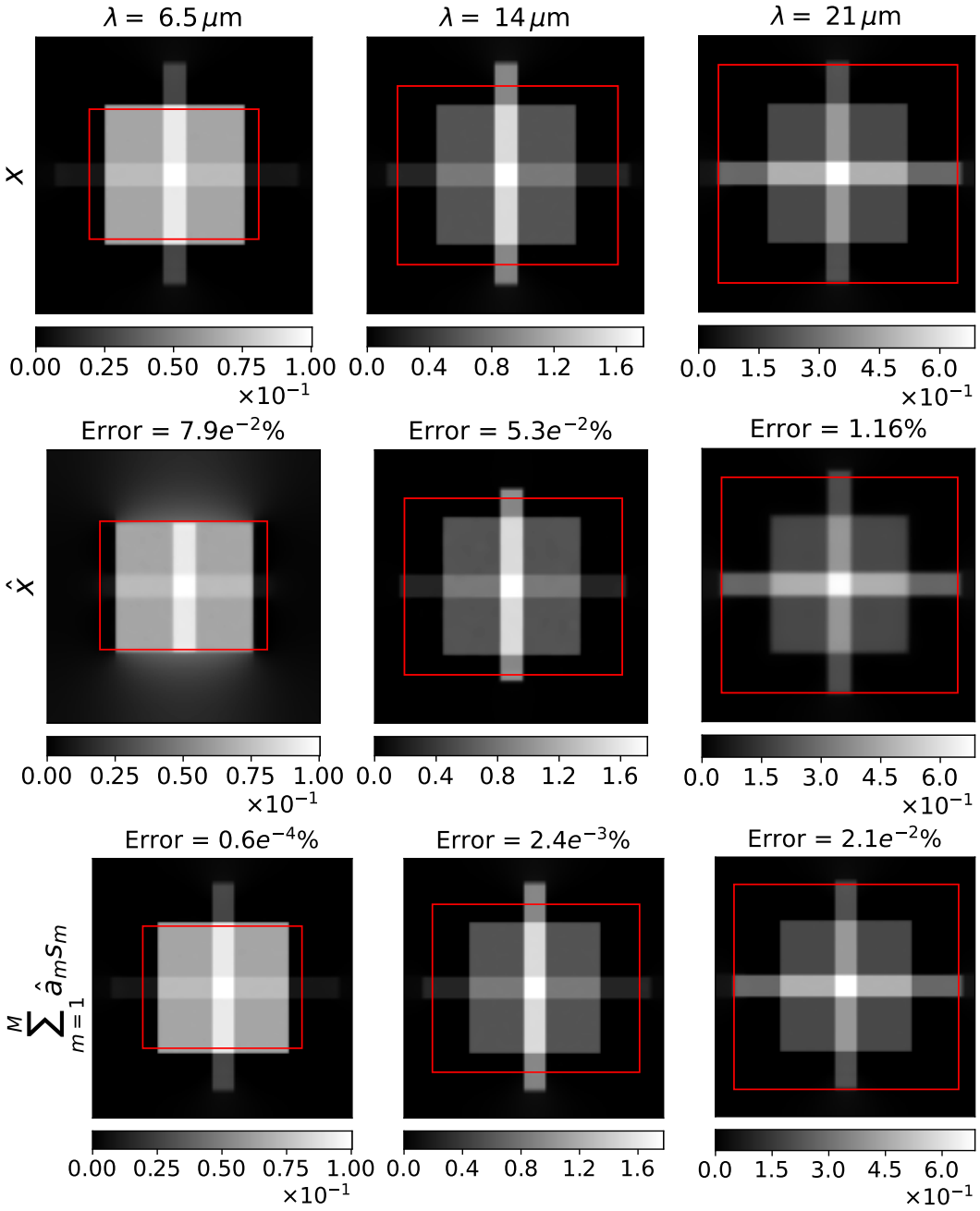

Figure 5.1: Spatial reconstruction for Obj_1 at 30dB: [1st row] Original images $\boldsymbol{x}$ at 6.5, 14 and 21 μm. [2nd row] Spatio-spectral reconstruction of $\boldsymbol{x}$ with spatial and spectral regularization for edge-preserving. [3rd row] Reconstruction of $\boldsymbol{x}$ as a linear combination of the estimated $\boldsymbol{a}$ and the known $\mathbf{s}$.

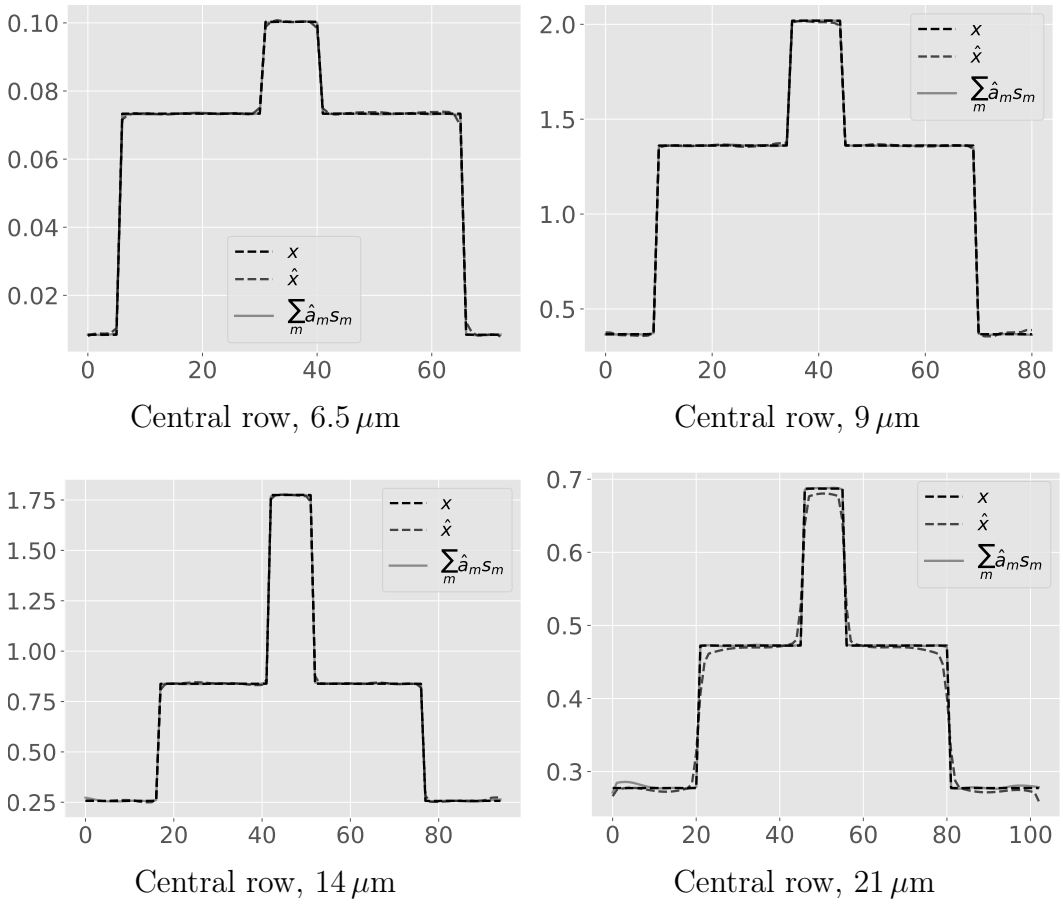

Figure 5.2: Spatial reconstructions of the central row for obj_1 at λ = 6.5, 9, 14, and 21 μm, with the spatio-spectral reconstruction algorithm and the reconstruction as a linear combination of the estimated $\boldsymbol{a}$ and the known $\mathbf{s}$.

Spectral distribution: We display in Fig. 5.3 the spectral distributions of the original $\boldsymbol{x}$, the reconstructed $\hat{\boldsymbol{x}}$ with the spatio-spectral reconstruction and the LMM reconstruction. In Fig. 5.3 (Top panel: left), the spectral distribution of the reconstructed $\hat{\boldsymbol{x}}$ with both algorithms fits the original spectral distribution over the whole measured range (from 4.75 to 28.5 μm) because the spatial position corresponds to a smooth region. In Fig. 5.3 (Top panel: right), the spatial position is chosen in a region with a high gradient. The spectral distribution of the spatio-spectral reconstruction fits perfectly the original spectral distribution at small wavelengths but fails to perfectly match the original distribution at long wavelengths because the spectral distribution are highly mixed within a spatial location; however, the layout of the spectral distribution and the edges are preserved.
The two spatial locations in the top panel of Fig. 5.3 are observed by all spectral channels. In the bottom panel, we compare the spectral distribution for a spatial

location observed only with channel 4[2]. Of course, the spatio-spectral reconstruction does not provide spectral information outside the spectral range of Channel 4. In contrast, the spectral distribution with the LMM reconstruction is entirely given regardless of the spatial position and the observed spectral channels since the spectral components $\mathbf{s}$ are known and covers the whole measured spectral range.

To quantify the spatial and spectral performances of the reconstructed algorithms, we use the averaged SAM, PSNR, and SSIM, detailed in paragraph IV-D of section 5.2. The values of these quality metrics are reported in Table 5.1. First, both reconstruction algorithms show a good spectral distribution with SAM values very close to 0. The LMM reconstruction shows the lowest SAM value, which is expected since the spectral resolution of $\hat{\boldsymbol{x}}$ is imposed by the known $\mathbf{s}$. Moreover, the LMM reconstruction have the best SSIM values since it provides a better spatial quality than the spatio-spectral reconstruction. Overall, the LMM reconstruction shows the best spatio-spectral reconstruction for Obj_1, with the highest PSNR value.

	$\hat{\boldsymbol{x}}$	$\sum_m \hat{\boldsymbol{a}}_m \boldsymbol{s}_m$
PSNR	45.5	61.5
SSIM	0.97	0.99
SAM	$1e^{-2}$	$5e^{-4}$

Table 5.1: Global PSNR, SSIM and SAM for the reconstructed obj_1 with the spatio-spectral reconstruction algorithm of $\boldsymbol{x}$ and the reconstruction algorithm of $\boldsymbol{x}$ as a linear combination of the estimated $\boldsymbol{a}$ and the known $\mathbf{s}$.

5.4 Conclusion

We present a new forward model for the IFS instrument of JWST/MIRI that is based on the low-rank approximation of the 2D+λ input image, with known spectral components $\mathbf{s}$. This new forward model was used for the reconstruction of the unknown mixing coefficients $\boldsymbol{a}$ using the Quadratic Majorize-Minimize (Q-MM)[3] optimization algorithms [Chouzenoux 2011]. This work is the subject of a publication submitted in "IEEE Transactions on Computational Imaging" and explicitly integrated into the first section of this chapter.

In the second section of this chapter, we use 2D+λ synthetic image to validate the performance of the spatio-spectral reconstruction algorithm proposed in Chapter 4 used to reconstruct $\boldsymbol{x}$ directly from the measurements $\boldsymbol{y}$ and the LMM reconstruction algorithm, where the reconstructed $\hat{\boldsymbol{x}}$ results from $\sum_{m=1}^{M} \hat{\boldsymbol{a}}_m \boldsymbol{s}_m$. Both reconstruction algorithms significantly enhance the spatial and spectral resolutions of $\hat{\boldsymbol{x}}$, but the LMM reconstruction algorithm shows overall a better spatio-spectral

[2]see the channel description in Table 1 from the previous section

[3]code available online at `http://github.com/forieux/qmm`

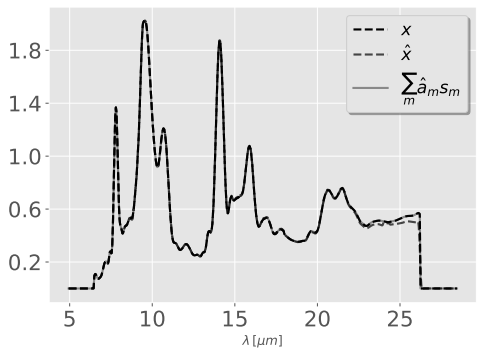

(a) Pixel (60,60)

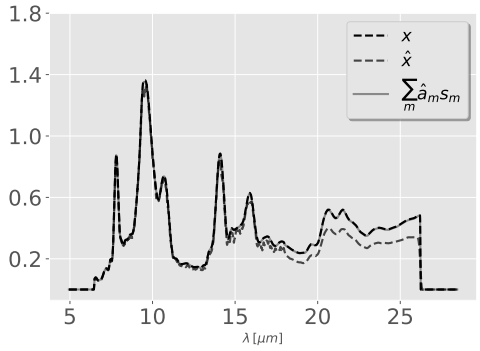

(b) Pixel (55,30)

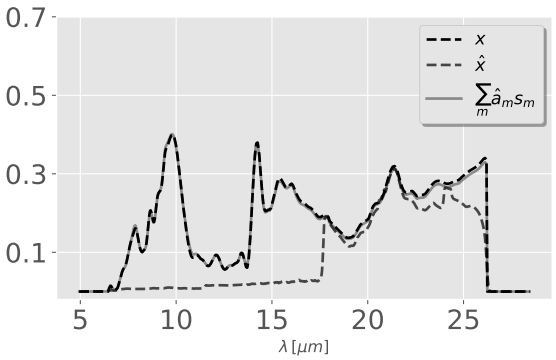

(c) Pixel (60,9)

Figure 5.3: Comparison of the spectral reconstruction for obj_1 with the spatio-spectral reconstruction algorithm of $\boldsymbol{x}$ and the reconstruction algorithm of $\boldsymbol{x}$ as a linear combination of the estimated $\boldsymbol{a}$ and the known $\mathbf{s}$ for a spatial position located in a smooth region (Top panel: left), a spatial position located in a region presenting high gradients (Top panel: right), and a spatial position observed only with the spectral channel 4 (Bottom panel).

reconstruction and provide the best qualitative results with a normalized least square error less than $2.1\,10^{-2}\,\%$. In addition, the spectral information with the LMM reconstruction is entirely given regardless of the characteristics of the channels. In contrast, the spatio-spectral reconstruction directly from the measurements $\boldsymbol{y}$ does not provide a full spectral reconstruction, particularly for spatial locations not observed by all spectral channels. However, the spectral components $\mathbf{s}$ are, in many cases, not provided *a priori* and must be estimated before or jointly with the estimation of the mixing coefficients.

Chapter 6

General Conclusion

6.1 Summary of the contributions

This thesis deals with reconstructing a discrete 2D+λ image (hyperspectral image) with a high spatial and spectral resolutions from a set of blurred, truncated, and aliased 2D measurements using inverse problem approaches. The measurements are acquired from an HS imaging system based on Integral Field Spectrometers (IFS). In particular, we are interested in the Mid-Resolution Spectrometer of the Mid-Infrared Instrument (MIRI) onboard the James Webb Space Telescope (JWST). The telescope and the instrument involve complex components that spatially and spectrally modify and degrades the measurements. In Chapter 3 we have studied the characteristics and identify the responses of these components, which is a crucial step to build the forward model to be used for the reconstruction process.

First, the JWST incorporates an all-reflective system that focuses the light of the 2D+λ input image on a focal plane. Because of the diffraction, the response of the optical system (or spatial PSF) introduces a spatial blurring to the focused sky images that depend on the wavelength. However, accurate knowledge of the PSF is not always ensured, particularly for the JWST, because of the complex shape of its mirror. Therefore, we use the official WebbPSF simulator developed by the Space Telescope Science Institute (STScI) to simulate the wavelength-dependent PSFs numerically.

Moreover, the MRS instrument measures an extensive infrared range (4.9 - 28.3 μm) observed from different spectral channels to allow a full wavelength coverage on multiple detectors with a high spectral resolution (ranging from 1500-3000). Each channel incorporates an Integral Field Unit (IFU) that observes a Field of View (FOV) through several slits in parallel, with a variable number and size of the slits across spectral channels. The light inside each spatio-spectral selection is dispersed with a diffraction grating that introduces a wavelength-dependent spectral blurring with a known PSF form, then projected and sampled onto 2D detectors with heterogeneous spatial and spectral step sizes depending on the channel. Since the spatial sampling is insufficient at all wavelengths, the telescope allows a dither-

ing mode consisting of slightly shifting of the telescope pointing between exposures following a specific pattern, leading to a multi-frame Super Resolution problem.

In chapter 4, we have tackled the reconstruction of a discrete 2D+λ image by jointly processing the overall set of degraded 2D multi-frame measurements observed from different selections (spectral channels and IFU) and pointings of the instrument. The reconstruction process is based on the inverse problem approaches and relies on two major stages. The first stage in the conception of a forward model depends on the discrete object model. The forward model is a series of mathematical operators modeling the response of the IFS instrument. It allows the extraction of an observation matrix $\boldsymbol{H}$ that establishes a relationship between the measurements $\boldsymbol{y}$ and the unknown input $\boldsymbol{x}$, and its transpose $\boldsymbol{H}^t$, both used in the reconstruction algorithm. In the second stage, we propose a reconstruction algorithm based on the regularized least square methods where the solution is the minimizer of a mixed criterion composed of a data fidelity term and some prior knowledge about the unknown input. However, the reconstruction problem is ill-posed because the matrix $\boldsymbol{H}^t\boldsymbol{H}$ is ill-conditioned mainly from blurring. To correct the ill-posedness, we use convex spatial and spectral regularization terms for edge-preserving. Finally, since a closed-form expression of the minimizer is not explicit, we rely on the fast half-quadratic approaches based on Geman and Reynolds formulation to estimate the solution.

We have tested the reconstruction algorithm on two synthetic HS input images with various spatial and spectral distributions. To showcase the importance of edge-preserving regularization, particularly around spatial edges, we compare our algorithm with state-of-art algorithms such as the classic l_2 regularization and the shift-and-add (S&A) algorithm. Since the latter does not consider the blurring, we also compare the proposed algorithm with the S&A followed by spatial TV deconvolution for each spectral band. Even though the proposed algorithm is computationally more complex among the reconstruction algorithms, it allows a significant increase in the spatial and spectral resolutions and provides the best qualitative results, with the smallest error between the original and reconstructed 2D+λ images for both synthetic images. We have also studied the dependence of our results on the signal-to-noise ratio (SNR) of the simulated measurements. Finally, we have extended our comparison by applying source separation techniques such as principal component analysis and non-negative matrix factorization to the original and reconstructed images with the proposed and S&A algorithms. The goal is to evidence the importance of deconvolution and the Super-Resolution on the extracted spectral components. We observe that the spectral components extracted from the reconstructed input image with the proposed algorithm match the original spectral components, which is not the case of the non-deconvoluted spectral components provided by the S&A algorithm.

The proposed algorithm described in chapter 4, however, presents some limitations that are mainly related to the spatio-spectral object model. First, the forward model involves complex components and is computationally burdensome. Second,

the reconstructed HS images, measuring a broad infrared range, are composed of several thousand spectral bands. Therefore, the number of unknowns to estimate is relatively significant, leading to an increase in the computational complexity of the reconstruction algorithm. In addition, our algorithm requires the determination of four hyperparameters (spatial and spectral regularization parameters and edge-preserving thresholds), which is a long process regarding the computational cost. Finally, the spectral distributions, particularly for astronomical observations, usually include spectral rays, spectral features, and a continuum requiring different spectral regularization parameters and thresholds for the different types of spectral information.

Chapter 5 considers a new discrete linear model for the HS input image $\boldsymbol{x}$, allowing to overcome the limitations of the algorithm proposed in Chapter 4. In particular, we assume that $\boldsymbol{x}$ lives in a low dimensional subspace and can be represented by a small number of spectral components $\mathbf{s}$, assumed known, each weighted by an unknown mixing coefficient $\boldsymbol{a}$. This representation preserves the spatial and spectral distributions of $\boldsymbol{x}$.

The proposed reconstruction algorithm is based on the regularized least square approaches with a convex spatial regularization for edge-preserving. The problem is solved with a highly effective optimization algorithm called the Majorize-Minimize step strategy and subspace optimization. We show on simulations that the proposed algorithm shows a significant increase in spatial resolution, especially around the edges. Moreover, the reconstruction algorithm allows the preservation of the spectral distribution, particularly the spectral rays, thanks to the known spectral components. Finally, we evaluate the spatial and spectral performances of the reconstructed image $\hat{\boldsymbol{x}}$ with the proposed l_2 and the S&A algorithms. We observe that $\hat{\boldsymbol{x}}$ with our algorithm shows the least spectral distortion (SAM), the least spatial degradation of structural information (SSIM), and the highest PSNR.

6.2 Perspectives

The contributions presented in this thesis allow several improvements and open perspectives for future work.

1) The forward models provided in Chapters 4 and 5, modeling the responses of the MRS instrument (detailed in Chapter 3), is used to simulate the 2D multiframe measurements. However, other simulators have been developed mainly for the MRS instrument. In particular, a publicly available Python package called "MIRISim" [Klaassen 2020], developed by the MIRI instrument team provides on-orbit performance of the MRS instrument and allows accurate representation of the measurements. Therefore, it is necessary to evaluate the performance of our reconstruction algorithms (that depends on our forward models) on measurements simulated with "MIRISim". In addition, it will also be necessary to evaluate the performance of our reconstruction algorithms on real data that should be transmitted

by the JWST from six months after launch.

2) Our reconstruction algorithm includes a multi-frame Super-Resolution step from multiple pointing of the MRS to enhance the spatial resolution of the reconstructed 3D image. Another solution for spatial resolution enhancement is to perform a fusion process between two sets of measurements of the same scene with complementary information [Guilloteau 2020]. We are thinking of the measurements provided by the MRS instrument [Wells 2015] with high spectral resolution (hyperspectral data with $\lambda/\Delta_\lambda \approx 1500 - 3500$) but limited spatial resolution due to spatial undersampling and small field of view (up to 6.9×7.9 arcseconds^2), and measurements provided by the imager of the MIRI instrument [Bouchet 2015] with high spatial resolution and extended field of view (74×113 arcseconds^2) but limited spectral resolution (multispectral data with $\lambda/\Delta\,\lambda \approx 5$). Both instruments cover the same spectral range from 4.89 to 27.8 μm. The fusion process can be formulated as an inverse problem where the reconstructed 2D+λ image $\hat{\boldsymbol{x}}$ is the minimizer of an objective function $\mathcal{J}$ associated with two data fitting terms for the hyperspectral (HS) and for the multispectral (MS) measurements, respectively, writing

$$\hat{\boldsymbol{x}} = \arg\min_{\boldsymbol{x}} \|\boldsymbol{y}_{\text{HS}} - \boldsymbol{H}_{\text{HS}}\boldsymbol{x}\|^2 + \|\boldsymbol{y}_{\text{MS}} - \boldsymbol{H}_{\text{MS}}\boldsymbol{x}\|^2 + \mu\mathcal{R}(\boldsymbol{x}) \tag{6.1}$$

where $\boldsymbol{y}_{HS}$ and $\boldsymbol{y}_{MS}$ denotes the hyperspectral and multispectral measurements, respectively, $\boldsymbol{H}_{HS}$ and $\boldsymbol{H}_{MS}$ the corresponding forward models, and finally $\mathcal{R}(\boldsymbol{x})$ the regularization term.
It would also be interesting to test the fusion process between two HS measurements observing the same scene and acquired from different instruments, such as the MRS instrument of JWST/MIRI and the infrared spectrometer (IRS) of the Spitzer telescope [1]. While the JWST includes a segmented hexagonal mirror of 6.5 m in diameter, the Spitzer telescope includes a monolithic circular mirror of 0.83 m in diameter. Consequently, the different HS measurements are spatially blurred with very different PSFs. In addition, the IRS and MRS instruments cover different spectral ranges with varying fields of view, spatial and spectral resolutions. Finally, the IRS and MRS instruments use different acquisition techniques to produce HS measurements. The MRS is an IFS instrument that observes the FOV through several slits in parallel, whereas the IRS acquires the measurements via successive spatial scanning by changing the telescope pointing.

3) The estimation of the unknown input $\boldsymbol{x}$ can be also done in the Bayesian framework instead of the deterministic framework [Idier 2001b]. The reconstructed $\hat{\boldsymbol{x}}$ from the measurements $\boldsymbol{y}$ can be inferred through its posterior distribution $P(\boldsymbol{x}|\boldsymbol{y})$. Given the measurements $\boldsymbol{y}$, $P(\boldsymbol{x}|\boldsymbol{y})$ can be derived from the likelihood function $P(\boldsymbol{y}|\boldsymbol{x})$ and a prior distribution $P(\boldsymbol{x})$ using the Bayes theorem that writes

$$P(\boldsymbol{x}|\boldsymbol{y}) = \frac{P(\boldsymbol{y}|\boldsymbol{x})P(\boldsymbol{x})}{P(\boldsymbol{y})} \tag{6.2}$$

[1] https://irsa.ipac.caltech.edu/data/SPITZER/docs/irs/

with $P(\boldsymbol{y})$ the marginal law for the measurements.
From Eq. (6.2), several estimators can be used to estimate $\boldsymbol{x}$ that requires the definition of the likelihood function and the prior distribution. The most common estimators are the maximum a posteriori probability (MAP) that leads to numerical optimization problems and the minimum mean square error (MMSE) that leads to a numerical integration problem.

The solution of the inverse problem depends on the estimation of hyperparameters that find a trade-off between the given measurements and the information provided by the *a priori* term. In the deterministic framework, we fixed the values of the hyperparameters manually by keeping the set that minimizes at best the error between the reconstructed and the original input image. However, the latter is not provided in many real life applications. Thus, we can rely on the unsupervised bayesian approaches where the hyperparameters can be considered nuisance parameters, estimated jointly with $\boldsymbol{x}$, which is a challenging problem [Dobigeon 2009].

4) The reconstruction of $\boldsymbol{x}$ considered in this thesis aims at solving a large system of linear equations that writes

$$\boldsymbol{A}\boldsymbol{x} = \boldsymbol{b} \tag{6.3}$$

where $\boldsymbol{b}$ is a known vector and $\boldsymbol{A} \in \mathbb{R}^{N \times N}$ is a square and positive definite matrix that writes

$$\boldsymbol{A} = \boldsymbol{H}^t\boldsymbol{H} + \mu\boldsymbol{V}^t\boldsymbol{B}\boldsymbol{V} \tag{6.4}$$

with $\boldsymbol{H}$ denoting the IFS forward model, $\boldsymbol{V}$ a linear operator and $\boldsymbol{B}$ an identity matrix or a diagonal matrix. Since the problem is high dimensional, direct inversion of the matrix $\boldsymbol{A}$ is computationally complex and untractable.

In Chapter 5 we reconstructed a 3D spatio-spectral input using iterative algorithms, such as the efficient optimization algorithm based on the Majorize-Minimize step and subspace approximation. In addition, we assumed a low-rank approximation for the 3D input to reduce the number of the estimated unknowns. However, the reconstruction problem remains computationally complex because of the complexity of the IFS forward model. Moreover, the reconstruction problem cannot be considered in the Fourier domain because of the heterogeneous spatial and spectral samplings and the spatio-spectral selections (like IFU and spectral channels). Other numerical options might be considered to accelerate the reconstruction process, in particular, preconditioning [Shewchuk 1994].

Preconditioning is a numerical solving method that reduces the condition number of the reconstruction problem and accelerates the rate of convergence of the iterative optimization algorithm. It consists of introducing a preconditioner $\boldsymbol{M} \in \mathbb{R}^{N \times N}$ of the matrix $\boldsymbol{A}$ such that $\boldsymbol{M}^{-1}\boldsymbol{A}$ has a smaller condition number than $\boldsymbol{A}$. Hence the problem at Eq. 6.3 rewrites

$$\boldsymbol{M}^{-1}\boldsymbol{A}\boldsymbol{x} = \boldsymbol{M}^{-1}\boldsymbol{b} \tag{6.5}$$

Ideally, $\boldsymbol{M}^{-1} = \boldsymbol{A}$. However, this case is not possible since inverting the matrix $\boldsymbol{A}$ is untractable. The preconditioner main objective is to approach $\boldsymbol{A}$ with $\boldsymbol{M}$ such that

the matrix $\boldsymbol{M}$ can be easily inverted with a low computational cost. For instance, we can consider that the matrix $\boldsymbol{M}$ writes

$$\boldsymbol{M} = \boldsymbol{H}'^{t}\boldsymbol{H}' + \mu\, \boldsymbol{D}^{t}\boldsymbol{I}\boldsymbol{D} \tag{6.6}$$

where $\boldsymbol{I}$ is an identity matrix and the matrix $\boldsymbol{H}'$ accounts only for the wavelength dependant spatial blurring and neglecting the other modifications and degradation of the original IFS forward model $\boldsymbol{H}$. The matrix $\boldsymbol{M}$ is, in that case, a block Toeplitz matrix and can be efficiently inverted in the Fourier domain [Hadj-Youcef 2020].

5) In Chapter 5, we assumed a low-rank approximation where the 3D input image $\boldsymbol{x}$ is formulated as a linear combination of spectral components $\mathbf{s}$, weighted by mixing coefficients $\boldsymbol{a}$. We also assumed that $\mathbf{s}$ are already known, and the inversion problem consisted of enhancing the spatial resolution of the reconstructed $\hat{\boldsymbol{x}}$ by estimating $\boldsymbol{a}$. However, the spectral components $\mathbf{s}$, in most cases, are not known *a priori* and must be estimated from the measurements $\boldsymbol{y}$.

Different algorithms for extracting the spectral components can be found in the literature [Henrot 2014b, Bioucas-Dias 2012]. In addition, estimating $\mathbf{s}$ can be achieved separately from the estimation of $\boldsymbol{a}$ or jointly.

The blind unmixing problem (estimation of both $\boldsymbol{a}$ and $\mathbf{s}$) is challenging because the spatial and spectral distributions of the measurements are severely degraded, particularly from the wavelength-dependent blur. Consequently, the estimation $\boldsymbol{s}$ before the reconstruction of $\boldsymbol{a}$ can be inaccurate since the spectral distribution is highly mixed because of the blurring.

Therefore, a joint deconvolution and unmixing can be used to solve the problem [Henrot 2014b].

In addition, in our work, we were only interested in using the LMM for subspace approximation and not in the physical meaning of the spectral components $\mathbf{s}$. However, the latter can be important in several applications, particularly to identify the chemical components of the observed scene. In that case, the mixing coefficients should satisfy the non-negativity constraint and the sum-to-one constraint. Thus, the estimation of $\boldsymbol{a}$ corresponds to solving constrained least squares approach that writes

$$\begin{aligned} \hat{\boldsymbol{a}} = \arg\min_{\boldsymbol{a}} \|\boldsymbol{y} - \boldsymbol{H}\sum_{m=1}^{M} \boldsymbol{a}_m \mathbf{s}_m\|^2 + \mathcal{R}(\boldsymbol{a}) \\ \text{subject to } \boldsymbol{a} > 0 \text{ and } \sum_{m=1}^{M} \boldsymbol{a}_m = 1 \end{aligned} \tag{6.7}$$

6) We can also test and validate the efficiency of our reconstruction algorithm on a synthetic 3D image expressed in a low-dimensional subspace, with at least one mixing coefficient that has a punctual point source as spatial distribution. This reconstruction can be very challenging since the spatial distribution of the measurements $\boldsymbol{y}$ can be lost because of the severe spatial blurring and detector integration.

Bibliography

[Akgun 2005] T. Akgun, Y. Altunbasak et R. M. Mersereau. *Super-resolution reconstruction of hyperspectral images.* IEEE Transactions on Image Processing, vol. 14, no. 11, pages 1860–1875, 2005. 49, 50

[Allain 2006] M. Allain, J. Idier et Y. Goussard. *On global and local convergence of half-quadratic algorithms.* IEEE Transactions on Image Processing, vol. 15, no. 5, pages 1130–1142, 2006. 34, 38, 39, 77, 80

[Almeida 2010] Mariana Almeida et Luis Almeida. *Blind and Semi-Blind Deblurring of Natural Images.* IEEE Transactions on Image Processing, vol. 19, pages 36–52, 01 2010. 28

[Arablouei 2016] Reza Arablouei, Ethan Goan, Stephen Gensemer et Branislav Kusy. *Fast and robust pushbroom hyperspectral imaging via DMD-based scanning.* CoRR, vol. abs/1608.00361, 2016. 43

[Berné 2007] O. Berné, C. Joblin, Y. Deville, J. D. Smith, M. Rapacioli, J. P. Bernard, J. Thomas, W. Reach et A. Abergel. *Analysis of the emission of very small dust particles from Spitzer spectro-imagery data using blind signal separation methods.* Astronomy and Astrophysics - A&A, vol. 469, pages 575–586, Juillet 2007. 14 pages, 11 figures, to appear in A&A. 48, 82

[Bioucas-Dias 2012] José M. Bioucas-Dias, Antonio Plaza, Nicolas Dobigeon, Mario Parente, Qian Du, Paul Gader et Jocelyn Chanussot. *Hyperspectral Unmixing Overview: Geometrical, Statistical, and Sparse Regression-Based Approaches.* IEEE Journal of Selected Topics in Applied Earth Observations and Remote Sensing, vol. 5, no. 2, pages 354–379, 2012. 47, 48, 98, 128

[Bongard 2011] S. Bongard, F. Soulez, É. Thiébaut et É. Pecontal. *3D deconvolution of hyper-spectral astronomical data.* Monthly Notices of the Royal Astronomical Society, vol. 418, no. 1, pages 258–270, 11 2011. 45, 46

[Bouchet 2015] Patrice Bouchet, Macarena García-Marín, P.-O. Lagage, Jérome Amiaux, J.-L. Auguéres, Eva Bauwens, J. A. D. L. Blommaert, C. H. Chen, Ö. H. Detre, Dan Dicken et et al. *The Mid-Infrared Instrument for theJames Webb Space Telescope, III: MIRIM, The MIRI Imager.* Publications of the

Astronomical Society of the Pacific, vol. 127, no. 953, page 612–622, Jul 2015. 24, 54, 126

[Bushouse 2015] Howard Bushouse, Michael Droettboom et Perry Greenfield. *The James Webb Space Telescope Data Calibration Pipeline.* In Proceedings of the 14th Python in Science Conference], Huff, K. and Bergstra, J., eds, volume 44. Citeseer, 2015. 65

[Buttingsrud 2006] Bård Buttingsrud et Bjørn Alsberg. *Superresolution of hyperspectral images.* Chemometrics and Intelligent Laboratory Systems, vol. 84, pages 62–68, 12 2006. 49

[Chambolle 2011] Antonin Chambolle et Thomas Pock. *A First-Order Primal-Dual Algorithm for Convex Problems with Applications to Imaging.* Journal of Mathematical Imaging and Vision, vol. 40, 05 2011. 31, 70, 86

[Charbonnier 1997] P. Charbonnier, L. Blanc-Feraud, G. Aubert et M. Barlaud. *Deterministic edge-preserving regularization in computed imaging.* IEEE Transactions on Image Processing, vol. 6, no. 2, pages 298–311, 1997. 31, 32, 34, 79, 81

[Chein-I Chang 2000] Chein-I Chang. *An information-theoretic approach to spectral variability, similarity, and discrimination for hyperspectral image analysis.* IEEE Transactions on Information Theory, vol. 46, no. 5, pages 1927–1932, 2000. 105

[Chouzenoux 2011] Emilie Chouzenoux, Jérôme Idier et Saïd Moussaoui. *A Majorize–Minimize Strategy for Subspace Optimization Applied to Image Restoration.* IEEE Transactions on Image Processing, vol. 20, no. 6, pages 1517–1528, 2011. 26, 36, 38, 39, 40, 41, 104, 118, 121

[Chouzenoux 2014] Emilie Chouzenoux, Maxime Legendre, Saïd Moussaoui et Jérôme Idier. *Fast Constrained Least Squares Spectral Unmixing Using Primal-Dual Interior-Point Optimization.* IEEE Journal of Selected Topics in Applied Earth Observations and Remote Sensing, vol. 7, no. 1, pages 59–69, 2014. 47

[Demoment 1989] G. Demoment. *Image reconstruction and restoration: overview of common estimation structures and problems.* IEEE Transactions on Acoustics, Speech, and Signal Processing, vol. 37, no. 12, pages 2024–2036, Dec 1989. 28, 71, 78

[Dobigeon 2009] Nicolas Dobigeon, SaÏd Moussaoui, Martial Coulon, Jean-Yves Tourneret et Alfred O. Hero. *Joint Bayesian Endmember Extraction and Linear Unmixing for Hyperspectral Imagery.* IEEE Transactions on Signal Processing, vol. 57, no. 11, pages 4355–4368, 2009. 48, 127

[Elliott 2005] Erin Elliott, James Burge et Derek Sabatke. *Analytic diffraction analysis of a 32-m telescope with hexagonal segments for high-contrast imaging.* Applied optics, vol. 44, pages 1360–5, 04 2005. 56

[Farsiu 2003] Sina Farsiu, Dirk Robinson, Michael Elad et Peyman Milanfar. *Robust shift and add approach to superresolution.* In Andrew G. Tescher, editeur, Applications of Digital Image Processing XXVI, volume 5203, pages 121 – 130. International Society for Optics and Photonics, SPIE, 2003. 26, 49, 70, 77, 78

[Fletcher 1964] R. Fletcher et C. M. Reeves. *Function minimization by conjugate gradients.* The Computer Journal, vol. 7, no. 2, pages 149–154, 01 1964. 37

[Fruchter 2002] A. S. Fruchter et R. N. Hook. *Drizzle: A Method for the Linear Reconstruction of Undersampled Images.* Publications of the Astronomical Society of the Pacific, vol. 114, no. 792, pages 144–152, feb 2002. 49, 70

[Galatsanos 1989] N.P. Galatsanos et R.T. Chin. *Digital restoration of multichannel images.* IEEE Transactions on Acoustics, Speech, and Signal Processing, vol. 37, no. 3, pages 415–421, 1989. 45

[Galatsanos 1991] Nikolaos Galatsanos, Aggelos Katsaggelos, Roland T Chin et Allen Hillery. *Least squares restoration of multichannel images.* Signal Processing, IEEE Transactions on, vol. 39, pages 2222 – 2236, 11 1991. 45

[Gardner 2009] Jonathan Gardner, John Mather, Mark Clampin, Rene Doyon, Matthew Greenhouse, H. Hammel, John Hutchings, Peter Jakobsen, Simon Lilly, K. Long, Jonathan Lunine, Mark Mccaughrean, Matt Mountain, John Nella, George Rieke, Marcia Rieke, Hans-Walter Rix, Eric Smith, George Sonneborn et Gillian Wright. *The James Webb Space Telescope.* Space Science Reviews, vol. 123, pages 485–606, 02 2009. 54

[Geladi 2007] Paul L. M. Geladi, Hans F. Grahn et James E. Burger. Multivariate images, hyperspectral imaging: Background and equipment, chapitre 1, pages 1–15. John Wiley & Sons, Ltd, 2007. 42, 43

[Geman 1992] D. Geman et G. Reynolds. *Constrained restoration and the recovery of discontinuities.* IEEE Transactions on Pattern Analysis and Machine Intelligence, vol. 14, no. 3, pages 367–383, 1992. 25, 33, 36, 79, 80, 104, 118

[Geman 1995] D. Geman et Chengda Yang. *Nonlinear image recovery with half-quadratic regularization.* IEEE Transactions on Image Processing, vol. 4, no. 7, pages 932–946, 1995. 33, 36, 45, 79, 80

[Goldstein 2009] Tom Goldstein et Stanley Osher. *The Split Bregman Method for L1-Regularized Problems.* SIAM J. Imaging Sciences, vol. 2, pages 323–343, 01 2009. 31

[Goodman 1996] Joseph W Goodman. Introduction to Fourier Optics McGraw-Hill Series in Electrical and Computer Engineering, volume 8. 1996. 24, 56, 66, 70, 71

[Guilloteau 2020] Claire Guilloteau, Thomas Oberlin, Olivier Berné et Nicolas Dobigeon. *Hyperspectral and Multispectral Image Fusion Under Spectrally Varying Spatial Blurs – Application to High Dimensional Infrared Astronomical Imaging*. IEEE Transactions on Computational Imaging, vol. 6, pages 1362–1374, Septembre 2020. 49, 50, 51, 126

[Hadamard 1902] J. Hadamard. *Sur les Problemes Aux Derivees Partielles et Leur Signification Physique*. Princeton university bulletin, pages 49–52, 1902. 28

[Hadj-Youcef 2020] M. Amine Amine Hadj-Youcef, François Orieux, Alain Abergel et Aurélia Fraysse. *Fast Joint Multiband Reconstruction from Wideband Images Based on Low Rank Approximation*. IEEE Transactions on Computational Imaging, pages 1–1, 2020. 24, 25, 47, 128

[Halicek 2019] Martin Halicek, Himar Fabelo, Samuel Ortega, Gustavo Marrero Callico et Baowei Fei. *In-Vivo and Ex-Vivo Tissue Analysis through Hyperspectral Imaging Techniques: Revealing the Invisible Features of Cancer*. Cancers, vol. 11, page 756, 05 2019. 11, 43

[Henrot 2011] Simon Henrot, Charles Soussen et David Brie. *Fast deconvolution of large fluorescence hyperspectral images*. In 2011 3rd Workshop on Hyperspectral Image and Signal Processing: Evolution in Remote Sensing (WHISPERS), pages 1–4, 2011. 45

[Henrot 2013] Simon Henrot, Said Moussaoui, Charles Soussen et David Brie. *Edge-preserving nonnegative hyperspectral image restoration*. In 2013 IEEE International Conference on Acoustics, Speech and Signal Processing, pages 1622–1625, 2013. 45

[Henrot 2014a] Simon Henrot, Charles Soussen et David Brie. *Sequential deconvolution — Unmixing of blurred hyperspectral data*. In 2014 IEEE International Conference on Image Processing (ICIP), pages 5152–5156, 2014. 48

[Henrot 2014b] Simon Henrot, Charles Soussen, Manuel Dossot et David Brie. *Does deblurring improve geometrical hyperspectral unmixing?* IEEE Transactions on Image Processing, vol. 23, no. 3, pages 1169–1180, 2014. 128

[Hestenes 1952] Magnus Rudolph Hestenes, Eduard Stiefel*et al.* Methods of conjugate gradients for solving linear systems, volume 49. NBS Washington, DC, 1952. 40

[Hook 2000] R. Hook et Andrew Fruchter. *Dithering, Sampling and Image Reconstruction*. vol. 216, page 521, 01 2000. 26, 65, 70, 77, 78

[Houck 2004] J. R. Houck, T. L. Roellig, J. van Cleve, W. J. Forrest, T. Herter, C. R. Lawrence, K. Matthews, H. J. Reitsema, B. T. Soifer, D. M. Watson, D. Weedman, M. Huisjen, J. Troeltzsch, D. J. Barry, J. Bernard-Salas, C. E. Blacken, B. R. Brandl, V. Charmandaris, D. Devost, G. E. Gull, P. Hall, C. P. Henderson, S. J. U. Higdon, B. E. Pirger, J. Schoenwald, G. C. Sloan, K. I. Uchida, P. N. Appleton, L. Armus, M. J. Burgdorf, S. B. Fajardo-Acosta, C. J. Grillmair, J. G. Ingalls, P. W. Morris et H. I. Teplitz. *The Infrared Spectrograph (IRS) on the Spitzer Space Telescope.* The Astrophysical Journal Supplement Series, vol. 154, no. 1, pages 18–24, sep 2004. 42, 56

[Hunt 1971] B. Hunt. *A matrix theory proof of the discrete convolution theorem.* IEEE Transactions on Audio and Electroacoustics, vol. 19, no. 4, pages 285–288, 1971. 34, 72

[Hunt 1984] B. Hunt et O. Kubler. *Karhunen-Loeve multispectral image restoration, part I: Theory.* IEEE Transactions on Acoustics, Speech, and Signal Processing, vol. 32, no. 3, pages 592–600, 1984. 45

[Hyvarinen 1999] A. Hyvarinen. *Fast and robust fixed-point algorithms for independent component analysis.* IEEE Transactions on Neural Networks, vol. 10, no. 3, pages 626–634, 1999. 47, 48, 104

[Idier 2001a] J. Idier. *Convex half-quadratic criteria and interacting auxiliary variables for image restoration.* IEEE Transactions on Image Processing, vol. 10, no. 7, pages 1001–1009, July 2001. 31, 33, 34, 71, 79, 81

[Idier 2001b] Jérôme Idier. Approche bayésienne pour les problèmes inverses. Lavoisier, Paris, 2001. 24, 28, 29, 35, 79, 126

[Jolliffe 2016] I. T. Jolliffe et Jorge Cadima. *Principal component analysis: a review and recent developments.* Philosophical Transactions of the Royal Society A: Mathematical, Physical and Engineering Sciences, vol. 374, 2016. 47, 104

[Keshava 2002] N. Keshava et J.F. Mustard. *Spectral unmixing.* IEEE Signal Processing Magazine, vol. 19, no. 1, pages 44–57, 2002. 47, 48, 95

[Khan 2018] M. J. Khan, H. S. Khan, A. Yousaf, K. Khurshid et A. Abbas. *Modern Trends in Hyperspectral Image Analysis: A Review.* IEEE Access, vol. 6, pages 14118–14129, 2018. 42

[Klaassen 2020] P D Klaassen, V C Geers, S M Beard, A D O'Brien, C Cossou, R Gastaud, A Coulais, J Schreiber, P J Kavanagh, M Topinka et et al. *mirisim: a simulator for the Mid-Infrared Instrument on JWST.* Monthly Notices of the Royal Astronomical Society, vol. 500, no. 3, page 2813–2821, Nov 2020. 125

[Labat 2008] Christian Labat et Jérôme Idier. *Convergence of conjugate gradient methods with a closed-form stepsize formula.* Journal of Optimization Theory and Applications, vol. 136, no. 1, pages 43–60, 2008. 36, 40

[Labiano 2016] Á. Labiano, R. Azzollini, J. Bailey, S. Beard, D. Dicken, M. Garćia-Mańin, V. Geers, A. Glasse, A. Glauser, K. Gordon, K. Justtanont, P. Klaassen, F. Lahuis, D. Law, J. Morrison, M. Müller, G. Rieke, B. Vandenbussche et G. Wright. *The MIRI Medium Resolution Spectrometer calibration pipeline.* In Astronomical Telescopes + Instrumentation, 2016. 63, 65

[Lallo 2012] Matthew D. Lallo. *Experience with the Hubble Space Telescope: 20 years of an archetype.* Optical Engineering, vol. 51, no. 1, page 011011, Feb 2012. 54

[Lee 1999] Daniel D. Lee et H. Sebastian Seung. *Learning the parts of objects by nonnegative matrix factorization.* Nature, vol. 401, pages 788–791, 1999. 47, 48, 50, 98, 104

[Liu 1991] Y Liu et C Storey. *Efficient generalized conjugate gradient algorithms, part 1: theory.* Journal of optimization theory and applications, vol. 69, no. 1, pages 129–137, 1991. 40

[Makidon 2007] RB Makidon, S Casertano, C Cox et R van der Marel. *The JWST point spread function: Calculation methods and expected properties.* NASA Technic Al Report, vol. 23, no. 24, page 155, 2007. 56

[Mather 2004] John Mather. *The James Webb Space Telescope.* 02 2004. 11, 54, 55

[Nocedal 2006] Jorge Nocedal et Stephen Wright. Numerical optimization. Springer Science Business Media, 2006. 34, 35, 36

[Orieux 2011] François Orieux, Jean-François Giovannelli, T. Rodet, Alain Abergel, Hacheme Ayasso et Mathieu Husson. *Super-resolution in map-making based on a physical instrument model and regularized inversion. Application to SPIRE/Herschel.* Astronomy and Astrophysics, vol. 539, 03 2011. 24

[Orieux 2013] François Orieux, J-F Giovannelli, Thomas Rodet et Alain Abergel. *Estimating hyperparameters and instrument parameters in regularized inversion Illustration for Herschel/SPIRE map making.* Astronomy & Astrophysics, vol. 549, page A83, 2013. 24

[P Nascimento 2007] Jose M. P Nascimento et Jose M. Bioucas-Dias. *Hyperspectral signal subspace estimation.* In 2007 IEEE International Geoscience and Remote Sensing Symposium, pages 3225–3228, 2007. 47

[Perrin 2012] Marshall D. Perrin, Rémi Soummer, Erin M. Elliott, Matthew D. Lallo et Anand Sivaramakrishnan. *Simulating point spread functions for the*

James Webb Space Telescope with WebbPSF. In Mark C. Clampin, Giovanni G. Fazio, Howard A. MacEwen et Jacobus M. Oschmann Jr., editeurs, Space Telescopes and Instrumentation 2012: Optical, Infrared, and Millimeter Wave, volume 8442, pages 1193 – 1203. International Society for Optics and Photonics, SPIE, 2012. 56

[Perrin 2014] Marshall D. Perrin, Anand Sivaramakrishnan, Charles-Philippe Lajoie, Erin Elliott, Laurent Pueyo, Swara Ravindranath et Loïc. Albert. *Updated point spread function simulations for JWST with WebbPSF.* In Jr. Oschmann Jacobus M., Mark Clampin, Giovanni G. Fazio et Howard A. MacEwen, editeurs, Space Telescopes and Instrumentation 2014: Optical, Infrared, and Millimeter Wave, volume 9143 of *Society of Photo-Optical Instrumentation Engineers (SPIE) Conference Series*, page 91433X, Août 2014. 56, 66, 72

[Polak 1969] E. Polak et G. Ribiere. *Note sur la convergence de méthodes de directions conjuguées.* ESAIM: Mathematical Modelling and Numerical Analysis - Modélisation Mathématique et Analyse Numérique, vol. 3, no. R1, pages 35–43, 1969. 40

[Pérez 2004] José-Philippe Pérez. Optique - fondements et applications. Bantam, 2004. Dunod. 24, 63, 70, 73

[Rodet 2008] Thomas Rodet, FranÇois Orieux, Jean-FranÇois Giovannelli et Alain Abergel. *Data Inversion for Over-Resolved Spectral Imaging in Astronomy.* IEEE Journal of Selected Topics in Signal Processing, vol. 2, no. 5, pages 802–811, 2008. 46

[Rodet 2009] T Rodet, François Orieux, Jean-François Giovannelli et Alain Abergel. *Data inversion for hyperspectral objects in astronomy.* pages 1 – 4, 09 2009. 24

[Rudin 1992] Leonid I. Rudin, Stanley Osher et Emad Fatemi. *Nonlinear total variation based noise removal algorithms.* Physica D Nonlinear Phenomena, vol. 60, no. 1-4, pages 259–268, Novembre 1992. 31, 79

[Shewchuk 1994] Jonathan R Shewchuk. *An Introduction to the Conjugate Gradient Method Without the Agonizing Pain.* Rapport technique, USA, 1994. 34, 35, 36, 37, 127

[Simões 2014] Miguel Simões, Jose Bioucas-Dias, Luis Almeida et Jocelyn Chanussot. *A Convex Formulation for Hyperspectral Image Superresolution via Subspace-Based Regularization.* IEEE Transactions on Geoscience and Remote Sensing, vol. 53, 11 2014. 50

[Song 2019] Yingying Song, El-Hadi Djermoune, David Brie et Céedric Richard. *Joint unmixing-deconvolution algorithms for hyperspectral images.* In 2019

27th European Signal Processing Conference (EUSIPCO), pages 1–5, 2019. 47

[Soulez 2013] Ferréol Soulez, Éric Thiébaut et Loïc Denis. *Restoration of hyperspectral astronomical data with spectrally varying blur*. EAS Publications Series, vol. 59, pages 403–416, Janvier 2013. 46

[Stark 1989] Henry Stark et Peyma Oskoui. *High-resolution image recovery from image-plane arrays, using convex projections*. J. Opt. Soc. Am. A, vol. 6, no. 11, pages 1715–1726, Nov 1989. 50

[Sung Cheol Park 2003] Sung Cheol Park, Min Kyu Park et Moon Gi Kang. *Super-resolution image reconstruction: a technical overview*. IEEE Signal Processing Magazine, vol. 20, no. 3, pages 21–36, May 2003. 24, 49, 67, 70

[Tikhonov 1995] A. N. Tikhonov, A. Goncharsky, V. V. Stepanov et Anatoly G. Yagola. Numerical Methods for the Solution of Ill-Posed Problems. Mathematics and Its Applications. Springer Netherlands, 1995. 26, 29, 31, 71, 79

[Vives 2008a] S. Vives, E. Prieto, Y. Salaun et P. Godefroy. *New technological developments in integral field spectroscopy*. In Eli Atad-Ettedgui et Dietrich Lemke, editeurs, Advanced Optical and Mechanical Technologies in Telescopes and Instrumentation, volume 7018, pages 959 – 968. International Society for Optics and Photonics, SPIE, 2008. 24

[Vives 2008b] S. Vives, E. Prieto, Y. Salaun et P. Godefroy. *New technological developments in integral field spectroscopy*. In Eli Atad-Ettedgui et Dietrich Lemke, editeurs, Advanced Optical and Mechanical Technologies in Telescopes and Instrumentation, volume 7018, pages 959 – 968. International Society for Optics and Photonics, SPIE, 2008. 43, 70

[Vivone 2014] Gemine Vivone, Luciano Alparone, Jocelyn Chanussot, Mauro Dalla Mura, Andrea Garzelli, Giorgio Licciardi, Rocco Restaino et Lucien Wald. *A Critical Comparison Among Pansharpening Algorithms*. volume 53, 07 2014. 50

[Wei 2015] Qi Wei, José Bioucas-Dias, Nicolas Dobigeon et Jean-Yves Tourneret. *Hyperspectral and Multispectral Image Fusion Based on a Sparse Representation*. IEEE Transactions on Geoscience and Remote Sensing, vol. 53, no. 7, pages 3658–3668, 2015. 50

[Wei 2016] Q. Wei, J. Bioucas-Dias, N. Dobigeon, J. Tourneret, M. Chen et S. Godsill. *Multiband Image Fusion Based on Spectral Unmixing*. IEEE Transactions on Geoscience and Remote Sensing, vol. 54, no. 12, pages 7236–7249, 2016. 49

[Wells 2015] Martyn Wells, J W. Pel, A Glasse, Gillian Wright, Gabby Kroes, Ruyman Azzollini, Steven Beard, Bernhard Brandl, Angus Gallie, V C. Geers, A M. Glauser, Peter Hastings, Th Henning, Rieks Jager, Kay Justtanont, Bob Kruizinga, Fred Lahuis, David Lee, Ismael Martinez Delgado et David Wright. *The Mid-Infrared Instrument for the James Webb Space Telescope, VI: The Medium Resolution Spectrometer*. Publications of the Astronomical Society of the Pacific, vol. 127, pages 646–664, 07 2015. 24, 42, 54, 55, 57, 63, 66, 71, 82, 85, 126

[Woodgate 1998] B. E. Woodgate, R. A. Kimble, C. W. Bowers, S. Kraemer, M. E. Kaiser, A. C. Danks, J. F. Grady, J. J. Loiacono, M. Brumfield, L. Feinberg, T. R. Gull, S. R. Heap, S. P. Maran, D. Lindler, D. Hood, W. Meyer, C. VanHouten, V. Argabright, S. Franka, R. Bybee, D. Dorn, M. Bottema, R. Woodruff, D. Michika, J. Sullivan, J. Hetlinger, C. Ludtke, R. Stocker, A. Delamere, D. Rose, I. Becker, H. Garner, J. G. Timothy, M. Blouke, C. L. Joseph, G. Hartig, R. F. Green, E. B. Jenkins, J. L. Linsky, J. B. Hutchings, H. W. Moos, A. Boggess, F. Roesler et D. Weistrop. *The Space Telescope Imaging Spectrograph Design*. Publications of the Astronomical Society of the Pacific, vol. 110, no. 752, pages 1183–1204, oct 1998. 42

[Yokoya 2012] Naoto Yokoya, Takehisa Yairi et Akira Iwasaki. *Coupled Nonnegative Matrix Factorization Unmixing for Hyperspectral and Multispectral Data Fusion*. IEEE T. Geoscience and Remote Sensing, vol. 50, pages 528–537, 02 2012. 50

[Yokoya 2017] Naoto Yokoya, Claas Grohnfeldt et Jocelyn Chanussot. *Hyperspectral and Multispectral Data Fusion: A comparative review of the recent literature*. IEEE Geoscience and Remote Sensing Magazine, vol. 5, no. 2, pages 29–56, 2017. 50

[Yu-Li You 1999] Yu-Li You et M. Kaveh. *Blind image restoration by anisotropic regularization*. IEEE Transactions on Image Processing, vol. 8, no. 3, pages 396–407, 1999. 28

[Zhang 2012] Hongyan Zhang, Liangpei Zhang et Huanfeng Shen. *A super-resolution reconstruction algorithm for hyperspectral images*. Signal Processing, vol. 92, no. 9, pages 2082 – 2096, 2012. 49, 98

[Zhao 2011] Yongqiang Zhao, Jinxiang Yang, Qingyong Zhang, Lin Song, Yongmei Cheng et Quan Pan. *Hyperspectral imagery super-resolution by sparse representation and spectral regularization*. EURASIP Journal on Advances in Signal Processing, vol. 2011, no. 1, pages 1–10, 2011. 79

[Zhao 2013] Xi-Le Zhao, Fan Wang, Ting-Zhu Huang, Michael K. Ng et Robert J. Plemmons. *Deblurring and Sparse Unmixing for Hyperspectral Images*. IEEE Transactions on Geoscience and Remote Sensing, vol. 51, no. 7, pages 4045–4058, 2013. 47, 104

[Zhou Wang 2004] Zhou Wang, A. C. Bovik, H. R. Sheikh et E. P. Simoncelli. *Image quality assessment: from error visibility to structural similarity.* IEEE Transactions on Image Processing, vol. 13, no. 4, pages 600–612, 2004. 105

université PARIS-SACLAY

ÉCOLE DOCTORALE
Sciences et technologies de l'information et de la communication (STIC)

Titre: Reconstruction hyperspectrale haute résolution par inversion de mesures spectroscopiques à integrale de champ. Application au spectromètre infrarouge MIRI-MRS du télescope spatial James webb.

Mots clés: Problème inverse, Super-Résolution, Image Hyperspectrale, Déconvolution, Spectroscopie.

Résumé: Cette thèse traite des approches de type problème inverse pour reconstruire une image 3D spatio-spectrale (2D+λ) à partir d'un ensemble de mesures infrarouges 2D fournies par l'instrument "Integral Field Spectrometer" (IFS) (Mid-Resolution Spectrometer: MRS) de l'instrument "Mid-Infrared" à bord du "James Webb Space Telescope" (JWST). Plusieurs difficultés se posent lors de la reconstruction car l'instrument IFS contient des composantes complexes qui dégradent et modifient les mesures: (1) les réponses des composantes ne sont pas parfaites et introduisent un flou spatial et spectral aux mesures qui dépendent de la longueur d'onde, (2) l'instrument considère plusieurs observations avec plusieurs champs de vue (comme les canaux spectraux et les fentes parallèles), (3) les sorties de l'instrument sont projetées sur plusieurs détecteurs 2D et échantillonnées avec des pas d'échantillonnage hétérogènes.

La reconstruction d'image 2D+λ est un problème mal posé principalement en raison du flou spatio-spectral et de l'échantillonnage spatial insuffisant. Pour compenser la perte d'informations spatiales, le MRS permet des observations multiples de la même scène d'entrée en décalant le pointage du télescope, conduisant à un problème de Super-Résolution (SR).

Nous proposons un algorithme de reconstruction qui traite conjointement les informations spatiales et spectrales des mesures 2D suivant deux étapes. Tout d'abord, nous concevons un modèle direct qui décrit la réponse des composantes de l'instrument IFS comme une série d'opérateurs mathématiques et qui établit une relation entre les mesures et l'image 2D+λ d'entrée qu'on cherche à reconstruire. Ensuite, le modèle direct est utilisé pour reconstruire l'image 2D+λ en s'appuyant sur l'approche des moindres carrés régularisée avec une régularisation convexe pour la préservation des contours. Nous nous appuyons sur les approches semi quadratiques rapides basées sur la formulation de Geman et Reynolds pour résoudre le problème. L'algorithme de reconstruction proposé permet une fusion des mesures issues de différentes observations spatio-spectrales avec différents flous et différents échantillonnages, une SR à partir des différents pointages de l'instrument, et une déconvolution pour minimiser le flou.

Un autre modèle direct pour le même instrument est également développé dans notre travail, en supposant que l'image 2D+λ d'entrée vit dans un sous-espace de faible dimension et peut être modélisée comme une combinaison linéaire de composantes spectrales, supposées connues, pondérées par des coefficients de mélange inconnus. Nous nous appuyons ensuite sur l'algorithme d'optimisation Majorize-Minimize Memory Gradient (3MG) pour estimer les coefficients de mélange inconnus. L'approximation par sous-espace réduit le nombre d'inconnues. Par conséquent, le rapport signal sur bruit augmente. De plus, le modèle de mélange de source avec des composantes spectrales connues permet de conserver l'information spectrale complexe de l'image 2D+λ reconstruite.

La reconstruction proposée est testée sur plusieurs images 2D+λ synthétiques ayant des différentes distributions spatiales et spectrales. Notre reconstruction montre une déconvolution nette et une amélioration significative des résolutions spatiales et spectrales des images 2D+λ reconstruites par rapport aux algorithmes de l'état de l'art, notamment autour des bords.

Title: High-resolution hyperspectral reconstruction by inversion of integral field spectroscopy measurements. Application to the MIRI-MRS infrared spectrometer of the James Webb Space Telescope

Keywords: Inverse problem, Super-Resolution, Hyperspectral images, Deconvolution, Spectroscopy.

Abstract: This thesis deals with inverse problem approaches to reconstruct a 3D spatio-spectral (2D+λ) image from a set of 2D infrared measurements provided by the Integral Field Spectrometer (IFS) instrument (Mid-Resolution Spectrometer: MRS) of the Mid-Infrared Instrument on board the James Webb Space Telescope. The reconstruction is challenging because the IFS involves complex components that degrade the measurements: (1) the responses of the components are not perfect and introduce a wavelength-dependant spatial and spectral blurring, (2) the instrument considers several observations of the input with several spatial and spectral fields of views, (3) the output measurements are projected onto multiple 2D detectors and sampled with heterogeneous step sizes.

The 2D+λ image reconstruction is an ill-posed problem mainly due to spatio-spectral blurring and insufficient spatial sampling. To compensate for the loss of spatial information, the MRS allows multiple observations of the same scene by shifting the telescope pointing, leading to a multi-frame Super-Resolution (SR) problem.

We propose a SR reconstruction algorithm that jointly processes the spatial and spectral information of the degraded 2D measurements following two main steps. First, we design a forward model that describes the response of the IFS instrument as a series of mathematical operators and establishes a relationship between the measurements and the unknown 2D+λ input image. Next, the forward model is used to reconstruct the unknown input. The reconstruction is based on the regularized least square approach with a convex regularization for edge-preserving. We rely on the fast half-quadratic approaches based on Geman and Reynolds formulation to solve the problem. The proposed algorithm enables fusion of measurements from different spatio-spectral observations with different blur and different sampling, a multi-frame Super-Resolution from the different pointing of the instrument, and a deconvolution to minimize the blurring.

Another forward model for the same instrument is also developed in our work, by assuming that the 2D+λ input image lives in a low dimensional subspace and can be modeled as linear mixing model (LMM), which is linear combination of spectral components, assumed known, weighted by unknown mixing coefficients. We then rely on the Majorize-Minimize Memory Gradient (3MG) optimization algorithm to estimate the unknown mixing coefficients. The subspace approximation reduces the number of the unknowns. Consequently, the signal-to-noise ratio is increased. In addition, the LMM formulation with known spectral components allows to preserve the complex spectral information of the reconstructed 2D+λ image.

The proposed reconstruction is tested on several synthetic HS images with different spatial and spectral distributions. Our algorithm shows a clear deconvolution and a significant improvement of the spatial and spectral resolution of the reconstructed 2D+λ images compared to the state-of-art algorithms, particularly around the edges.

Université Paris-Saclay
Espace Technologique / Immeuble Discovery
Route de l'Orme aux Merisiers RD 128 / 91190 Saint-Aubin, France